TÉCNICO LISBOA

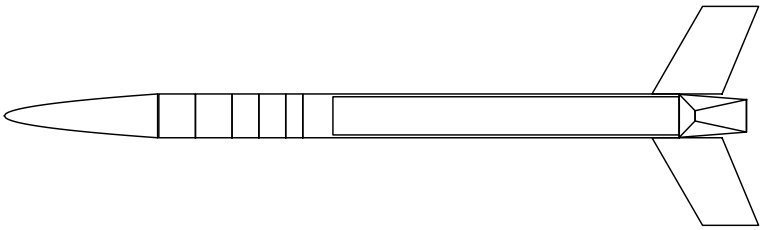

Sounding Rocket Multidisciplinary Preliminary Design and Trajectory Optimisation

Alexandre Mendes Palaio

Thesis to obtain the Master of Science Degree in

Aerospace Engineering

Supervisors: Professor André Calado Marta
Professor Paulo Jorge Soares Gil

Examination Committee

Chairperson: Professor Fernando José Parracho Lau
Supervisor: Professor André Calado Marta
Member of the Committee: Professor Alain de Souza

December 2024

”Nothing in life is to be feared, it is only to be understood.
Now is the time to understand more, so that we may fear less.”
Marie Curie

Declaration

I declare that this document is an original work of my own authorship and that it fulfills all the requirements of the Code of Conduct and Good Practices of the Universidade de Lisboa.

Acknowledgments

First and foremost, I would like to thank my supervisors, Professors André Marta and Paulo Gil, for their patience, guidance, and knowledge throughout these tremendously hard months full of dedication, sleepless nights, and, above all, learning, high dosages of it. Although I have always felt like I was the pilot in command, I could not have passed through the authentic flight check which was my dissertation without your helping hand in those moments when critical thinking was preciously needed.

Secondly, I would like to thank Captain Marta Santos for your unmatched dedication to providing me with the best possible support even before this dissertation became a reality.

I must also express my deepest gratitude to my comrades SABRES, with whom I developed a bond that goes beyond every few words I could pointlessly arrange to describe, ever since we were first-year cadets taking our first steps in the Air Force Academy. It is with great pleasure that, after all these years, I recognise that we have developed such a strong sense of collective identity, it is a personal conviction of mine that each one of us could not have reached so far individually. Working daily alongside you, always setting the bar a little higher than I could grasp under the motto *Quem não deu tudo, nunca deu nada*, truly was the key to my personal and professional growth.

Lastly, I would like to dedicate my final regards to my family and friends who were always there for me when I needed them the most, always finding their way to cheer me up and push me forward, and without whom I would have never dared enough.

To those not directly mentioned but who have nonetheless helped me in any way, shape, or form throughout my academic journey, I would like to share my present and future successes, as they are and will be a by-product of even the smallest of your contributions so far.

Resumo

Projetar um foguete é uma tarefa complexa, não só devido às condições difíceis do meio, mas também devido ao forte acoplamento entre disciplinas. Neste âmbito foi desenvolvida uma ferramenta de optimização multidisciplinar (MDO), com o objetivo de executar o design preliminar de um foguete com um único estágio movido a propulsão sólida. A escolha do algoritmo de optimização, da arquitetura MDO e dos modelos disciplinares, nomeadamente, massa e dimensionamento, dinâmica de voo, aerodinâmica, propulsão, estrutural e atmosférico, foi feita de forma a que a ferramenta numérica desenvolvida tenha um custo computacional reduzido, sendo simultaneamente capaz de satisfazer um conjunto de requisitos de missão pré-estabelecidos para problemas de optimização de co-projeto, devido ao acoplamento entre os processos de optimização da trajetória e de dimensionamento do foguete. As capacidades desta ferramenta foram testadas para diferentes conjuntos de variáveis de projeto e múltiplas missões de crescente complexidade, para problemas de optimização destinados a minimizar a massa total do foguete, impondo simultaneamente uma restrição de altitude mínima, dada uma capacidade de carga útil prescrita. Em primeiro lugar, estudos com até 10 variáveis geométricas mostraram que o uso do seu número máximo permitiu obter os melhores resultados, como esperado. Seguidamente, estudos de sensibilidade da carga útil e da altitude mínima confirmaram que o dimensionamento do foguete é significativamente afetado por ambos. Finalmente, por intermédio de comparações com foguetes reais, nomeadamente o REXUS 2 e o REXUS 10, foi possível mostrar uma boa concordância geral dos resultados, alcançando uma redução da massa total de 14,5 % e 14,9%, respetivamente. Dada a grande modularidade da ferramenta, perspetiva-se que uma extensão da aplicação da mesma para foguetes com múltiplos estágios ou movidos a propelente líquido, possa ser feita mediante desenvolvimentos adicionais.

Palavras-chave: MDO, Trajetória, Co-projeto, Foguete Sonda, Modularidade

Abstract

The design of rockets is known to be a complex task, not only due to the harsh operating conditions but also the strong coupling among disciplines. A multidisciplinary optimisation (MDO) framework was developed, aimed at providing preliminary designs of a single-stage solid propellant rocket. The choice of the optimiser algorithm, MDO architecture and discipline models, namely, mass and sizing, flight dynamics, aerodynamics, propulsion, structural and atmospheric, were such that the developed numerical tool has a very low computational cost while being able to meet a set of pre-established mission requirements. The resulting design framework solved a co-design optimisation problem, due to the coupling between the trajectory and rocket sizing optimization processes. The capabilities of the design framework were tested for different sets of design variables and multiple missions, with increasing complexity, for an optimisation problem aimed at minimizing the total mass of the rocket while imposing a minimum altitude constraint, with a prescribed payload capacity. First, studies with up to 10 geometric design variables showed that the latter were capable of achieving the best results, as expected. Then, sensitivity studies of the payload and the minimum altitude confirmed that the rocket sizing is greatly impacted by both. Lastly, comparisons with real rockets, namely the REXUS 2 and REXUS 10, showed very good agreement, achieving a total mass reduction of 14.5 % and 14.9%, respectively. Given the great modularity of the framework, a straightforward extension to other types of rockets, such as multi-stage or liquid-propellant, is expected upon additional development.

Keywords: MDO, Trajectory, Co-design, Sounding Rocket, Modularity

Contents

List of Tables

List of Figures

Glossary

AAO	All-At-Once
BFGS	Broyden-Fletcher-Goldfarb-Shanno
BLISS	Bi-Level Integrated System Synthesis
CFD	Computational Fluid Dynamics
CO	Collaborative Optimisation
DDO	Disciplinary Design Optimisation
EADS	European Aeronautic Defense and Space Company
FEM	Finite Element Method
GA	Genetic Algorithms
GLOW	Gross Lift-Off Weight
HBVP	Hamiltonian Boundary-Value Problem
IDF	Individual Discipline Feasible
ISS	International Space Station
KKT	Karush-Kuhn-Tucker
LEO	Low Earth Orbit
LP	Linear Programming
LRE	Liquid Rocket Engines
LV	Launch Vehicle
MCO	Modified Collaborative Optimisation
MDA	Multidisciplinary Analysis
MDF	Multidisciplinary Design Feasible
MDO	Multidisciplinary Design Optimisation

MOGA	Multi-Objective Genetic Algorithm
NASA	National Aeronautics and Space Administration
NLP	Nonlinear Programming
PMP	Pontryagin's Minimum Principle
PSO	Particle Swarm Optimisation
REXUS	Rocket-borne Experiments for University Students program
RNII	Jet Propulsion Research Institute
R&D	Research and Development
SLSQP	Sequential Least Squares Programming
SQP	Sequential Quadratic Programming
SRM	Solid Rocket Motor
TPBVP	Two Point Boundary Value Problem
U.S.	United States of America
USSR	Union of Soviet Socialist Republics
XDSM	Extended Design Structure Matrix

Chapter 1

Introduction

1.1 Motivation and Objectives

Over the last two decades, a new generation of entrepreneurs has made an unprecedented investment in Space, completely changing the paradigm. Private companies, such as *SpaceX*, *Virgin Galatic*, *Rocket Lab*, *United Launch Alliance*, *Blue Origin*, *Deep Space Industries* and *Astra Space* have now an important role in the future of the space industry, no longer controlled by the political agendas of a few superpower nations [1].

Presently, 70 countries have an active space program, 20 of which have an annual civilian budget above $100 million [2]. Furthermore, the global space economy is experiencing a rapid expansion nearly doubling in size from $304 billion [3], in 2012, to $546 billion, in 2022, 78% of which comes from commercial space products, services, infrastructure and support industries and only 22% from government budgets [4].

The private sector has recently played such an important role that government space agencies formed public-private partnerships with the largest conglomerates in the world in a joint effort to make us a space fairing society [5]. As an example of this, in 2021 and for the first time in history, the *National Aeronautics and Space Administration* (NASA) selected a private company to provide a Launch Vehicle (LV) for a major mission [6]. *SpaceX* was commissioned a $2.9 billion contract to develop the *Starship Human Lander* to carry astronauts to the moon as part of the *Artemis* mission [7].

While space exploration, space tourism, and space infrastructure are now the main focus of such private and semi-private initiatives [1], Science has always been the major beneficiary of space human endeavours [5, 8, 9] because it has only been possible to overcome the simplest technological milestones in space with the greatest sense of passion, ingenuity, and inspiration, three key drivers towards scientific progress [10]. Thousands of consumer goods, health and medicine practices and devices, industrial products, energy, environment, public safety and transportation technologies available today have been developed as the result of *NASA spin-off technologies* [11].

In the near future, scientific groups will continuously be awarded with new lines of Research and Development (R&D) on new Launch Vehicle (LV) designs capable of accomplishing their assigned goals

in compliance with the most demanding mission requirements.

Currently, the scientific research on modern Multidisciplinary Design Optimisation (MDO) methods applied to the design process of LVs is a hotspot in the aerospace industry, in an effort to further minimise the material usage, manpower, cost, and time, while maximising the reliability, operability, and safety of such systems [12].

The main goal of this dissertation is, then, to develop and validate an MDO framework coupled with trajectory optimisation capable of conducting the preliminary design of sounding rockets with a minimum payload capacity of 44 kg and 100 km minimum peak altitude, so that the results may be compared to well known and documented rockets, namely, the Rocket borne Experiments for University Students program (REXUS) [13].

In the pursuit of such an endeavour, several secondary objectives were established:

- Identify the main systems and subsystems of sounding rockets to be modelled;
- Identify the main mission requirements, design variables, and their couplings;
- Select a suitable MDO architecture, optimisation algorithm and trajectory optimisation method;

1.2 Launch Vehicle Design

LVs are highly complex, expensive, and typically, expendable rocket-powered vehicles intended to place a determined payload at a specific altitude, carrying a specific speed [14].

Several LV architectures have been developed that can be classified according to different criteria: traditional rockets, lifting bodies and winged bodies in terms of structure; expendable or reusable in terms of usability; orbital or suborbital in terms of trajectory; simple payload carriers or more complex human transport spacecrafts in terms of mission assignment; and rocket-based combined cycle, duct-engine (commonly called “air breathing engines”), liquid, solid or hybrid, in terms of propulsion [15], as schematically presented in Figure 1.1.

Launch vehicles are composed by multiple integrated systems and subsystems, each of them involving detailed knowledge of different disciplines, such as, aerodynamics, propulsion, structures, trajectory, guidance, navigation, and control [16].

Rapidly enough, LV design becomes fundamentally an optimisation problem in which the most important task is to develop a great sense of understanding of not only the physical phenomena involved but also the interactions between disciplines with the main goal set to achieve the design that optimally complies with all mission requirements of performance, affordability, reusability, operability, safety, and reliability [17].

One of the possible approaches to rocket design is the *Concurrent engineering method* [18], illustrated in Figure 1.2a. This method relies on an iterative process in which a central data set controlled by a senior systems engineer is updated with the results from every engineering team, traditionally working sequentially but more recently simultaneously in their specific discipline models. In addition, most design choices are made through periodic multidisciplinary collaborative work sessions [18].

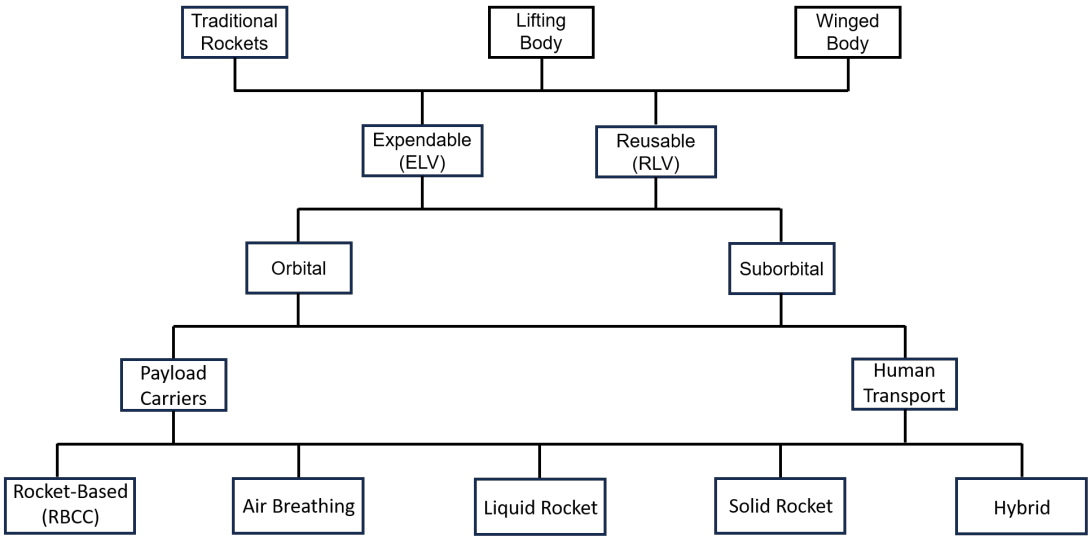

Figure 1.1: Launch vehicle architectures [15].

The advantages of this method are enhanced collaborative work between multidisciplinary engineering teams and reliance on human empirical non-heuristic intuition over major design choices [18]. Some major disadvantages, however, include a total dependence on the concatenation of local disciplinary optimisations, which might jeopardise the achieved optimal system due to the lack of awareness of possible conflicting interactions between disciplines [18], a significant dependence on the quality of the initial values assumed for the design variables which, in the case of poor choices, might lead to local optimum values instead of their global optimum [16], and, lastly, a clear restriction to Fixed Point Iterations (FPI) instead of a more desirable wide search through the design space [19].

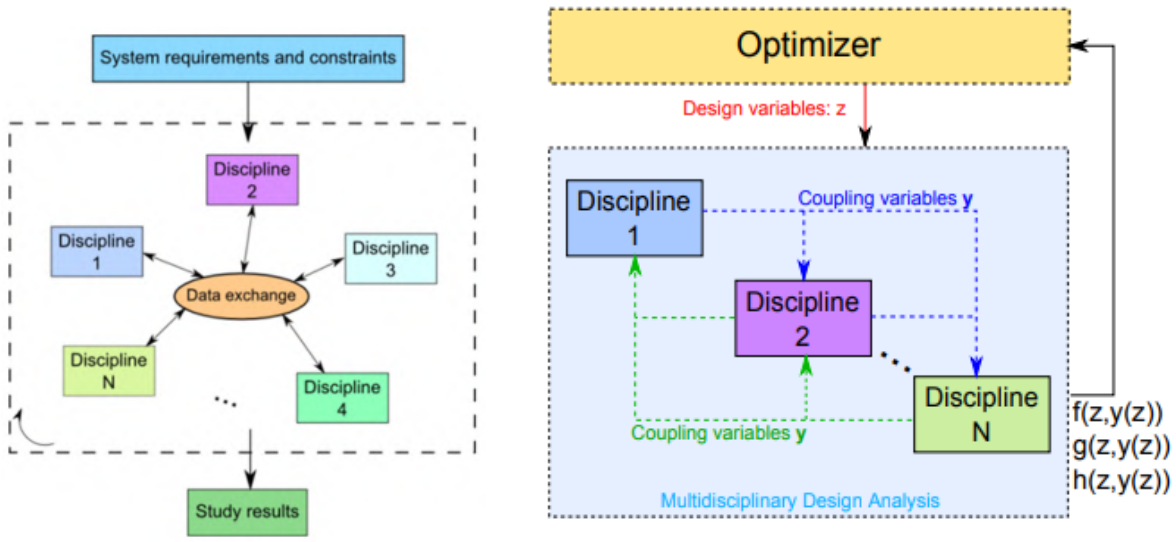

(a) Concurrent engineering [18].

(b) MDO framework [20].

Figure 1.2: Launch vehicle design methodologies.

In the 1990s, as governmental space programs became increasingly more ambitious and private companies gradually started to get involved, a ferocious and renewed commercial competitiveness,

cost-efficiency, and marketability of space affairs and activities led into a new design methodology that could overcome the existing concurrent engineering limitations [18]. The new paradigm, labelled MDO, was based on the idea of taking advantage of the most recent technological advancements to develop computer-based engineering systems capable of conducting the design process of a space launch system, in compliance with its assigned mission requirements, in a completely automated fashion considering all the complex interactions, coupled effects, and trade-offs between different subsystems and disciplines through the entire design space [21].

Objectively, concurrent engineering is an optimisation system that consists of optimising the design variables simultaneously but separately for each discipline. This stands as a problem every time there is a *shared variable* (a variable that affects multiple disciplines) because the optimisation of such variables will very likely reach conflicting values among disciplines [21]. In contrast, MDO frameworks fully depend on multidisciplinary performance metrics with respect to as many design variables as possible, automatically finding the best trade-offs between disciplines for each shared variable, balancing the losses in one discipline with the benefits of that precise change in another, finally achieving the best feasible system possible [21]. Figure 1.2b shows a high-level MDO framework structure using the Multidisciplinary Design Feasible (MDF) architecture [20].

1.3 Sounding Rockets

1.3.1 A Brief History Overview

Since 1903, when *Konstantin E. Tsiolkovsky* first mathematically introduced the concept of using a reaction engined device to reach high altitudes in space [22], rocket research efforts started to be seen as a new form of Science. *R. H. Goddard* followed Tsiolkovsky's steps, breaking a few important milestones: predicted that the performance of the traditional solid rockets could be improved by burning liquid fuels in a small combustion chamber, by arranging the rocket configuration in stages and by using the *De Laval* nozzle configuration to increase the achieved exhaust speeds far beyond the speed of sound [23]. Later, in 1926, *Herman Oberth* defined the mathematical laws that govern rocketry and space flight [24], further corroborating *Goddard's* ideas of using rockets as platforms to carry objects "as far as the moon" [25].

These early days of rocketry were followed by an epoch filled with scientific innovation, technological development, and an increased level of sophistication in rocket design. *Goddard* launched the world's first liquid-fuel rocket (3 m long, liquid oxygen and gasoline fuelled rocket with a 4.5 kg lift-off weight [26]) and introduced the first instruments in his rockets (an aneroid barometer, a thermometer, and a camera) making them truly sounding rockets [27]. The *Soviet Union* (USSR) answered with the world's first jet assisted aircraft take-off (JATO) [28] in 1931, and with their first liquid-fuelled sounding rocket launches in 1933 [29]. In the following years, several rocket R&D groups were established worldwide, which further accelerated the already achieved progress in sounding rocket development: the *Verein fur Raumschiffarht* (Rocket Society) in Germany, the *American Rocket Society*, and the Soviet *Jet Propul-*

sion Research Institute (RNII) [30].

During the *World War II* (WWII) (1939-1945), Germans, Soviets and Americans developed new cutting-edge technologies for military purposes, which culminated with the first mass-produced rocket, the *V-2 (Vergeltungswaffe 2)* [31], a long-range guided missile (14.04 m long, 1.65 m in diameter, 5580 km/h maximum speed, 12980 kg of GLOW, and 750 kg of explosive charge), acknowledged to have been technologically 10 years ahead of its time [32]. The V-2 introduced a series of technological advancements: a pre-chamber system that enhanced the overall engine fuel mixing capabilities, a new fuel injection system for higher thrusts, a shorter and rounder combustion chamber attached to a new nozzle configuration with reduced friction (using a 30 degree opening angle instead of the more conventional 10 - 12 degree angles), a cutting-edge aerodynamic shape, inspired by a bullet round shape, a new guidance system called *Inertial Guidance System* and a new radio transmission system, which could relay live performance information [33].

In the aftermath of WWII, following a series of Allied coalition experimental V-2 rocket launches in German soil, the U.S condensed decades worth of scientific knowledge by recruiting hundreds of highly selected engineers and technicians from the V-2 development program (under project Paperclip) and granting them citizenship to conduct further experimental launches in U.S. soil (at White Sands Proving Ground, New Mexico) [34, 35]. Suddenly, turbo-pump systems, gyro-stabilization systems, aerodynamic and jet-deflector flight controls, automatic sequencing launch systems, flight trajectory tracking systems, recording devices, gimbal-mounted clustered rocket motors and parachute recovery systems were a known reality [36].

The period comprehended between the late 1950s to the early 1970s became known as the “golden age” of sounding rockets [37], as aerospace engineers started to systematically test clever and practical new solutions for highly complicated problems: from aerodynamic analysis of decreased stability at high Mach number [38], development and testing of revolutionary payload recovery systems [39, 40], neutralization of the falling mass hazard by the fragmentation of the spent vehicle assembly through a controlled explosion [41], development of new empirical methods based on experimental data for a rapid determination of the aerodynamic distributed loads during the ascent flight phase [42], development of pratical methods for the evaluation of aerothermal effects on sounding rockets [43], changes in rocket engine characteristics at staging, rocket trajectories and new atmospheric drag profiles to solve the two-stage sounding rocket problem [44], a new fluidic sounding rocket motor ignition system is found feasible which disregards using wiring and any supply of eletrical and stored energy [45], optimum thrust programming for a minimum GLOW to reach a specified altitude [46], aeroelastic analysis of sounding rocket vehicles [47], to the research on the application of new structural materials for sounding rockets, such as fiber reinforced plastics [48].

An average of 500 launches per year worldwide was reported in this period [37], a significant amount of which came from a very successful NASA international cooperative program, which established cooperation between the U.S and 19 countries, with a diverse range of scientific applications: aeronomy, biology, particles and fields, galactic astronomy, ionospheric physics, meteorology, special projects, radio astronomy, solar physics, test and support [37]. Furthermore, a great number of nations launched

their own sounding rocket programs independently starting to create their own research capabilities, namely, Canada, Argentina, India, Japan, Denmark, Norway, France, Germany, Spain, Sweden, United Kingdom, among others [49].

In the 1980s and 1990s, sounding rocket R&D activities entered in a stall phase and were partially overlooked by public funding and private investment [50]. Seen as a well known reality in a field with little margin for technological innovation, they were surpassed by other more ambitious space endeavours, such as the International Space Station (ISS), the Space Shuttle program, and satellite in-orbit placement missions, for commercial and scientific research purposes [50]. As a consequence, suborbital launches, in particular, sounding rocket ones, decreased drastically from several hundred to well under 100 per year [50].

1.3.2 Main Features and Current Applications

Amongst all existing LVs, sounding rockets have the simplest design, being typically composed by four main systems: structural system, which makes up the frame of the rocket (nose cone, rocket external casing, etc); guidance system, which includes all avionic components and physical parts meant to control the rocket during manoeuvres and provide stability during the launch and atmospheric flight (on-board computers, sensors, radars, fins, thrust vectoring systems, etc); recovery system, crucial in the recovery process of the rocket (the most common choice of all being the parachute); and propulsion system, which includes the rocket engine and all related parts (fuel tank, insulation layer, combustion chamber, nozzle, etc) [51–53]. The main parts of a sounding rocket are presented in Figure 1.3.

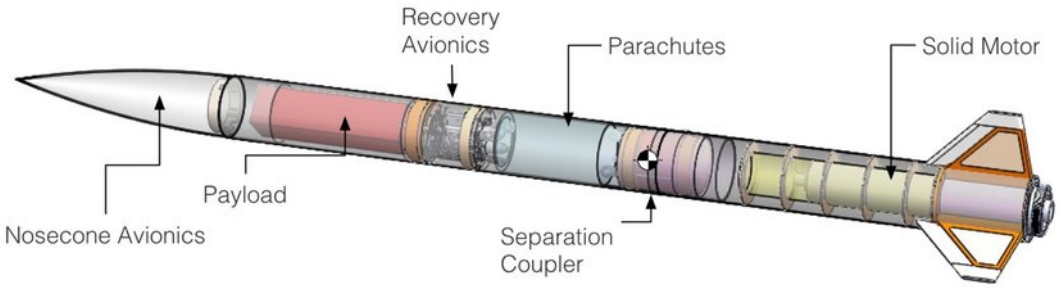

Figure 1.3: Sounding Rocket main parts [53].

Since their first introduction, sounding rockets have always been connected to the aerospace technological development, being the backbone of every major space program due to their innovation, flexibility, quick turn-around at a relatively low cost, and an excellent range of scientific applications across multiple fields such as space science and micro-gravity research [37, 54].

In terms of space science, these are the only type of LV capable of performing scientific flight missions regarding atmospheric and ionospheric phenomena because the highest altitude attainable by a balloon-borne instrument is 40 km and the lowest altitude reachable by an orbiting satellite is about 160 km, conducting *in-situ* experiments in that particular region [55, 56]. Additionally, sounding rockets are an excellent platform for scientific theory validation and instrument operational performance testing before their implementation on orbiting satellites [55]. They are commonly used to take measurements of

transient phenomena at very short notice, such as photometry, radiation, and magnetic-field properties in Low Earth Orbit (LEO) from solar activity [55].

In terms of microgravity, sounding rockets are typically used to conduct scientific suborbital flights of up to 12 minutes under microgravity conditions (less than 10^{-5} g [56]) for: material science, studying the effects of gravity during solidification of metals; fluid physics, studying the combustion behaviours in low-gravity conditions; astrobiology, studying the benefits of microgravity for medical purposes helping to assess the possibility of life beyond earth [55].

In the foreseeable future and despite all technological progress, sounding-rocket experimentation will remain a useful tool to test new scientific theories and instruments due to its unmatched reliability, affordability, practicability, and simplicity [54].

1.4 State of the Art

From the beginning of the 21st century to the present, an emerging market for Suborbital Reusable and Expendable Launch Vehicles has resurfaced, being expected to lead to a complete renaissance in sounding rocket technological demand [49]. Today, several sounding rocket research programs still remain operationally active and assume a relevant role in the aerospace scientific community due to their innovation, flexibility, quick turn-around, and low-cost, fundamentally performing science observation missions and experimental scientific instrument testing for technological proof of concept missions [55].

Despite all past technological advancements, several fundamental issues in the LV design process, particularly for sounding rockets, still remain unaddressed: insufficient payload accommodation, which leads to a high cost per kg of payload, poor cost/reliability relation, inefficient weight management (weight reduction is typically linked to higher complex dynamics systems and technological development costs), performance requirements management, high design sensitivities to environmental uncertainties and manufacturing processes, lack of reusable features, and poor compartmentalization of the design which if improved has been associated with higher efficiency and robustness of the launch system [17].

In an attempt to mitigate these issues, the application of MDO methods based on advanced computer algorithms has been used as an effective solution to optimise the design of a new generation of sounding rockets.

In 2004, an engineering team working for the European Aeronautic Defence and Space Company (EADS) applied such methodology in the design of a post-Ariane 5 new expendable European LV family in an attempt to maximise the injected payload mass by finding the best staging configuration and the propulsion parameters for a given class of payload into orbit [16]. Later, a Genetic Algorithm (GA) optimiser was implemented in an MDO integrated framework with five discipline models (propulsion, system aerodynamics, mass properties, flight dynamics, and a mass-based cost model) to optimise the design of a liquid-fuelled two or three-stage space launcher towards minimum cost and weight [57]. More recently, an MDF optimisation approach coupled with a GA optimiser and refined with a Gradient-Based algorithm was applied to design a microsatellite space launcher, taking into account structures, aerodynamics, trajectory optimisation, and cost models. It was concluded that this approach allowed

to significantly reduce the required time to evaluate the technical and economic feasibility of the design with cost minimisation [58].

Following alternative strategies, in 2006, three multilevel multidisciplinary optimisation techniques, Bi-Level Integrated System Synthesis (BLISS), Collaborative optimisation (CO), and Modified Collaborative optimisation (MCO), were evaluated, compared and contrasted against the industry's already accepted MDO technique, All-at-Once (AAO) and Fixed-Point Iteration (FPI) approach. This study was one of the first to test MDO techniques in realistic scenarios and demonstrated that the BLISS approach was the most promising one and also that there was an overall improvement across the three MDO studied methods over traditional AAO and FPI design process methods [19].

In 2011, a fitness inheritance technique coupled with a Particle Swarm Optimisation (PSO) algorithm within an integrated MDO framework was implemented to minimise the lift-off weight of a solid propellant launch vehicle through the optimisation of several disciplines: propulsion, structures, aerodynamics, and three-degree of freedom trajectory simulation. Results showed that the PSO approach had a very promising performance overall, significantly decreasing the number of function evaluations without considerable negative effects on the quality of the solutions [59]. This method was also used in the design of a single-stage solid propellant sounding rocket to reach a peak altitude of 100 km and carrying a payload of 20 kg with the results showing that the PSO method converged to an optimum solution with acceptable precision [60].

In 2015, an MDO framework of a hybrid rocket using a multi-objective genetic algorithm (MOGA) to investigate the effects of multi-combustion was developed. It was concluded that multi-combustion is not effective for the cases of maximum altitude and minimum total mass [61].

In 2017, an MDO approach was conducted to find the optimal design configuration of a single-stage sounding rocket with solid propulsion for lift-off mass minimisation, ensuring lift capabilities to send small payloads above the Von Karman line, paying special attention to the propulsion system sizing and thrust level selection. It was found that the nozzle expansion ratio should be optimised for the baseline configuration during the design process, propellant mass fraction has significant impact on sizing, high length-to-diameter ratio (slender body) and high nose fineness are recommended, and relatively long burn duration for each Solid Rocket Motor (SRM) size favours performance maximisation [62].

In 2021, a slightly different approach to maximise the payload accommodation while meeting several path constraints was conducted by running several evolution algorithms in parallel to solve the MDO problem [63], accounting for the optimal thrust law for the maximum combustion chamber internal pressure (a complete grain geometry redesign was needed) and the ascent trajectory optimisation through the implementation of a global, self-adaptive, partially restarted differential evolution optimisation algorithm using an ε-constraint handling technique based on the work of Takahama and Sakai [64] which had the ability to explore the design space searching for the global optimal solution within feasible regions.

Besides MDO applications, other worth mentioning research work in the context of sounding rocket development has also been published in recent years.

In 2016, a pseudo-analytic approach was used to determine the optimal launching conditions for the maximum peak altitude of a sounding rocket, considering a constant mass flow of propellant in a

standard atmosphere. It was concluded that, in a burnout situation, the increase in the rocket mass at a given mass ratio results in the increase of the optimal mass flow rate, and also that, the optimal mass flow rate varies linearly with the rocket mass [65].

In 2018, a methodology was proposed to design a new generation of sounding rockets using a general body configuration with four canards and four tail wings, assuming different payload masses and microgravity duration. Aerodynamic forces were calculated with high fidelity models, and three different guidance algorithms were used for the trajectory integration: constant altitude, near-radial and sun-pointing. It was concluded that the sun-pointing guidance algorithm offers nearly perfect microgravity conditions [66].

In 2021, a simple conceptual design procedure of a two-stage sounding rocket and its nozzles was conducted to reach maximum apogee using commercial software programs to perform Computational Fluid Dynamics (CFD) and rocket computation structural design analysis concluding that a thermal coating is needed to face the maximum temperatures felt at a height of 50 km at Mach four, and also that the highest drag coefficient, C_D, values were achieved at Mach 1 due to the formation of shock waves [67]. In the same year, a general sounding rocket preliminary design process for maximum range and payload mass under several construction restrictions was published. It was concluded that for a single-stage sounding rocket, a significant increase in the maximum speed and range only occurs until the ratio of the initial mass to the propellant mass is approximately 50, the achievable range of SRM is much lower because the specific thrust is 10-15% smaller comparatively to Liquid Rocket Engines (LRE). With SRM, more than 3 stages result in no significant increase in flight performance.

In 2022, a new type of design domain for a single-stage sounding rocket, varying three global design variables for peak altitude optimisation: thrust, burn time and propellant fraction, concluded that while maintaining the thrust constant, a greater propellant load does not guarantee an increased apogee altitude, there is an optimum burn time which allows altitude maximization, there is an optimal initial mass for a specific thrust targeted regardless of burn time and mass ratio, and that using only three global design variables simplifies the implementation of an iterative design system capable of maximizing the peak altitude of a single-stage sounding rocket, with a clear understanding of their influence on flight performance [68].

1.5 Dissertation Outline

The dissertation outline comprises seven chapters as follows:

- **Chapter 1: Introduction -** Serves the purpose of introducing the dissertations' motivation, objectives, context and state of the art;

- **Chapter 2: Rocket Fundamentals -** Some theoretical rocket fundamentals are presented, as well as, the models used in the development of the MDO framework (questions of performance, mass and sizing, aerodynamics, propulsion, structures, atmosphere, and trajectory are focused);

- **Chapter 3: Multidisciplinary Design Optimisation -** A brief theoretical overview of several MDO concepts, architectures, and optimisation algorithms is presented. Additionally, the trajectory optimisation topic is briefly discussed, with a special emphasis on direct collocation methods;
- **Chapter 4: Rocket Design Framework -** A comprehensive analysis of the used *Python* libraries (*OpenMDAO* integrated with *Dymos*) used to implement the MDO framework, as well as the actual implementation of the system;
- **Chapter 5: Rocket Optimal Design -** The developed MDO framework is tested to showcase its true optimisation capabilities in conducting a rapid, low computational cost yet accurate enough optimised sounding rocket preliminary design;
- **Chapter 6: MDO with High Fidelity Structural Analysis -** The developed MDO framework is integrated in a High Fidelity Structural Analysis model, developed by Fernandes [70], in order to assess how further can the structural mass be optimised taking an already optimised rocket as the starting point;
- **Chapter 7: Conclusion -** The main conclusions and achievements of the dissertation are emphasised, followed by relevant future work suggestions.

Chapter 2

Rocket Fundamentals

The design process of an LV is highly complex, requiring a deep understanding of not only the physical phenomena involved, but also, the interactions between different disciplines (aerodynamics, propulsion, structures, mass and sizing, etc.). Figure 2.1 serves the purpose of showing the high level of complexity involved in a typical preliminary design process.

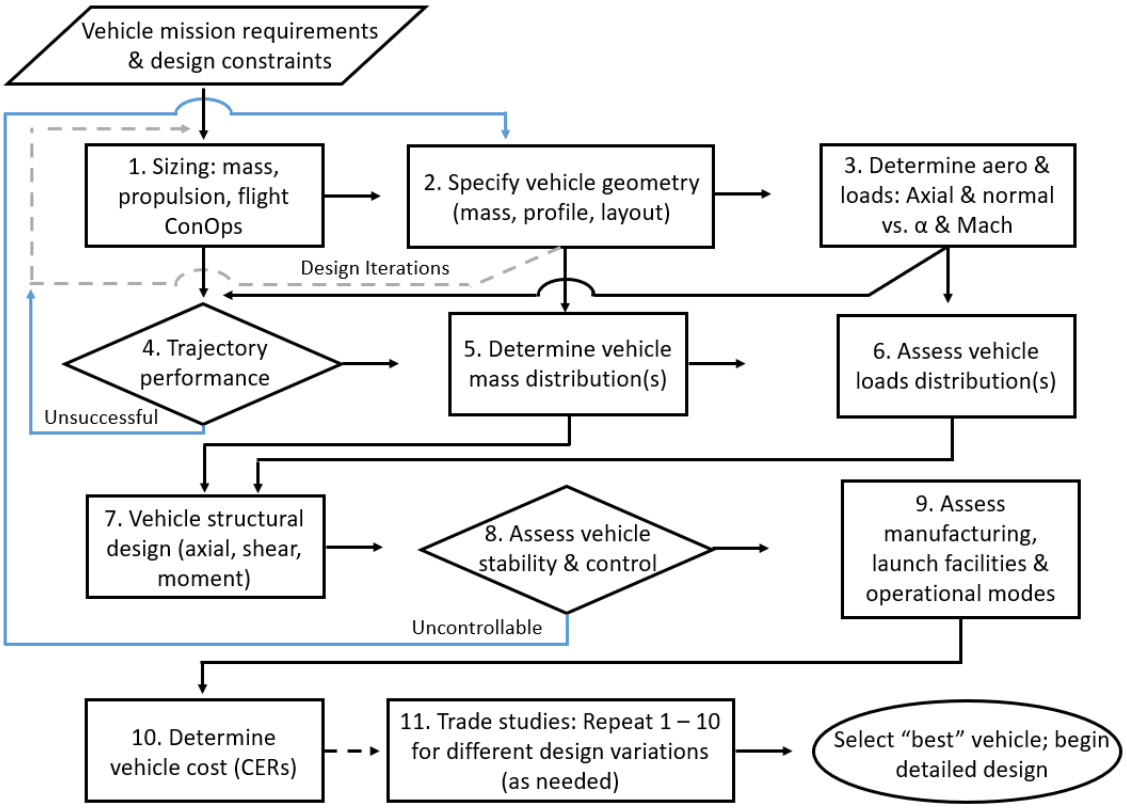

Figure 2.1: Launch vehicle typical preliminary design process [52].

2.1 Performance

In this section, a few basic rocket flight performance parameters will be defined, with a special emphasis on the rocket velocity change, an important parameter commonly used in the early stages of rocket design to assess the energy requirements for the intended mission profile.

To overcome the influence of the Earth's atmosphere, a rocket needs to produce thrust, T, to balance the intense aerodynamic drag and gravitational weight pulling it down during the most energy consuming stage of any rocket flight, the propelled ascent.

The total impulse, I, results from the sum of all measured values of thrust over a period of time [52]:

$$I = \int_0^t T dt = m_p c \ , \tag{2.1}$$

where m_p is the total mass of propellant and c is the rocket specific exhaust velocity.

By dividing the total impulse with the consumed propellant weight per unit time, $\dot{w}_p$, the specific impulse I_{sp} is obtained, and, alternatively, by dividing it by the total propellant volume, V_p, the volumetric specific impulse, I_V it is obtained. These are two important performance parameters because they quantitatively portray the overall power and size of the rocket engine and they are commonly used to compare different rocket propellants and engine architectures [52, 69].

$$I_{sp} = \frac{I}{\dot{w}_p} = \frac{T}{\dot{m}_p g_0} = \frac{c}{g_0} \ , \tag{2.2}$$

$$I_V = \frac{I}{V_p} = \frac{m_p g_0 I_{sp}}{V_p} = \rho_p g_0 I_{sp} \ , \tag{2.3}$$

where $\dot{m}_p$ is the propellant mass flow rate, $g_0 = 9.80665 \ m/s^2$ is the sea level gravitational acceleration, and ρ_p is the propellant mass density [52, 69].

To have a rough appreciation of the efficiency of the overall rocket design, a parameter called Impulse-to-Weight Ratio, $\frac{I}{W}$ is commonly used:

$$\frac{I}{W} = \frac{I_{sp} m_p}{(m_p + m_s + m_{PL}) g_0}, \tag{2.4}$$

Or, alternatively, the Trust-to-Weight Ratio, $\frac{T}{W}$:

$$\frac{T}{W} = \frac{T}{(m_p + m_s + m_{PL}) g_0}. \tag{2.5}$$

where W is the total weight of the rocket, m_s is the structural mass of the rocket and m_{PL} is the payload mass [69].

In energy terms, a rocket needs to gain just enough kinetic energy to change its velocity from a rest position, at launch, to a targeted velocity that allows it to reach a specific altitude or place a payload into a desired orbit, accounting for all the energy losses throughout the mission profile. Thus, the rocket overall change in velocity, Δv, needs to take into account: the physically unavoidable change in velocity to reach orbit, Δv_{orbit}; and compensate the energy losses due to gravitational effects effectively

expressed through gravity velocity losses, $\Delta v_{gravity}$, aerodynamic losses translated into drag velocity losses, Δv_{drag} and steering energy losses here treated as steering induced velocity losses, $\Delta v_{steering}$ [52],

$$\Delta v = \Delta v_{orbit} + \Delta v_{steering} + \Delta v_{drag} + \Delta v_{gravity}. \tag{2.6}$$

The Tsiolkovsky rocket equation is a simple approach to calculate the Δv_{orbit} term that only requires knowing the rocket's specific impulse, I_{sp}, initial and final masses, m_0 and m_f, respectively,

$$\Delta v_{orbit} = I_{sp}\ g_0\ ln\frac{m_0}{m_f}. \tag{2.7}$$

During spaceflight, the engine thrust direction will most likely not be parallel to the velocity direction, which represents the steering losses,

$$\Delta v_{steering} = \int_0^{t_f} \frac{2T}{m}\ sin^2\left(\frac{\delta+\alpha}{2}\right) dt, \tag{2.8}$$

where m is the instantaneous mass of the rocket, δ is the gimbal angle (the angle between the thrust line and the longitudinal body axis of the rocket), and α is the angle of attack. To attenuate these losses, the combined angle composed by the angle of the attack and the gimbal angle should be minimised.

To estimate the drag losses during the rocket ascent phase, one has to integrate the acting gravitational force through the ascent time period, as

$$\Delta v_{drag} = \int_0^{t_f} \frac{D}{m} dt = \frac{C_D S_{ref} \frac{1}{2}\rho v^2}{m} dt, \tag{2.9}$$

where C_D is the drag coefficient, S_{ref} is the reference area, ρ is the atmospheric density, and v is the instantaneous rocket speed. One direct conclusion is that the aerodynamic losses may be minimised forcing $\rho \to 0$ as fast as possible, which suggests ascending as quickly as possible, in other words, prescribing a vertical trajectory.

Furthermore, the gravity losses might be calculated as

$$\Delta v_{gravity} = \int_0^{t_f} g\ sin\gamma\ dt, \tag{2.10}$$

where g is the instantaneous gravitational acceleration and γ is the flight path angle of the rocket [52]. These losses need to be integrated during the atmospheric ascent phase time period because, as the rocket ascends, the gravitational acceleration will vary with altitude, and the rocket might suffer sudden changes in the flight path angle caused by unexpected wind gusts. Additionally, it might be concluded that these losses are only null either when the rocket is no longer under the influence of gravity or when the gravity vector is perpendicular to the velocity vector.

2.2 Mass and Sizing

The mass and sizing model is responsible for the estimation of masses and component sizing. Before the model was developed, it was necessary to identify the main rocket parts to be modelled. Figure 2.2 portrays the main rocket parts: nose cone tip, nose cone, payload module, service module, recovery module, body tube, propellant, casing, fins, boat tail, and nozzle.

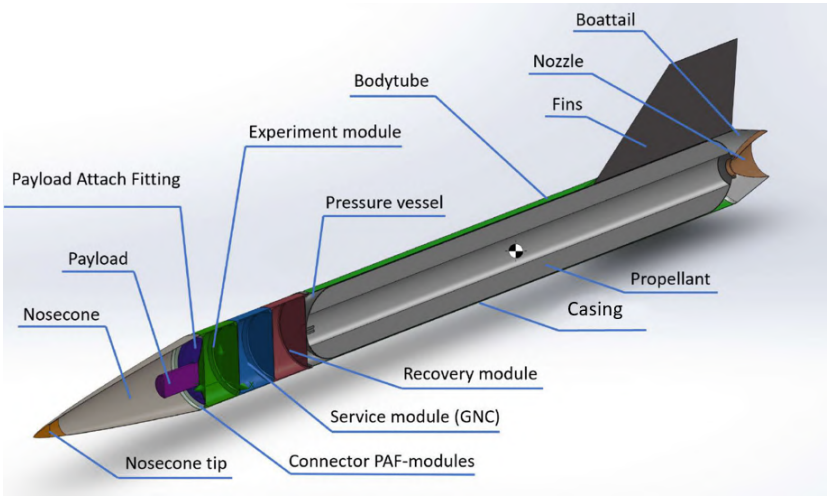

Figure 2.2: Rocket Layout Configuration [70].

Having identified the main rocket parts, a set of equations was assembled to model their mass and sizing.

Nose Cone and Nose Cone Tip

First, the rocket nose cone and tip equations were derived. Using their length-to-diameter ratios, it is possible to obtain the rocket length and nose cone length from the diameter. Additionally, the nose cone diameter is considered to be equal to the nose cone of the rocket. Lastly, the mass of the nose cone was obtained knowing the density of the material, its thickness, and surface area, while the mass of the nose cone tip was obtained knowing its structural material density and volume, [52]:

$$L_{rocket} = (L/D)_{rocket} D_{rocket} \ , \tag{2.11}$$

$$L_{nc} = D_{nc} (L/D)_{nose\,cone} \ , \tag{2.12}$$

$$D_{nc} = D_{rocket} \ , \tag{2.13}$$

$$S_r = \pi R_{rocket}^2 \ , \tag{2.14}$$

$$m_{nc} = \rho_{nc} t_{nc} S_{nc} \ , \tag{2.15}$$

$$m_{tip} = \rho_{tip} V_{tip} \ , \tag{2.16}$$

where L_{rocket}, is the rocket length, $(L/D)_{rocket}$ is the rocket length-to-diameter ratio (typically between 15 and 25 [62]), L_{nc} is the nose cone length, D_{nc} is the nose cone diameter, $(L/D)_{nose\,cone}$ is the nose

cone length-to-diameter ratio (typically assumes values between 3 and 6 [62], D_{rocket} the diameter of the rocket, R_{rocket} is the radius of the rocket, S_r the rocket reference area, m_{nc} is the nose cone mass, ρ_{nc} is the density of the nose cone structural material. t_{nc} is the thickness of the nose cone wall, S_{nc} is the nose cone surface area, m_{tip} is the mass of the tip, ρ_{tip} is the density of the tip, and V_{tip} is the volume of the tip.

Service, Recovery and Payload Modules

From the REXUS rocket standard configuration [13], a few parameters were fixed: the recovery system mass, m_R = 8.3 kg; the control and guidance systems operating within the service module, m_S = 13 kg; the module length, L_m = 30 cm.

Then, a set of equations was developed to calculate the mass of the service, recovery, and payload modules, m_S, m_R and m_{mPL}, knowing the dimensions of the rocket, D_{rocket} and R_{rocket}, the density of the module building materials ρ_m, for a given module thickness t_m. Finally, the total mass of each module was calculated by summing up the module mass, m_m, to the previously mentioned masses,

$$V_m = \pi(R_{rocket}^2 - (R_{rocket} - t_m)^2)L_m + 2\pi t_m R_{rocket}^2 \ , \tag{2.17}$$

$$m_m = V_m \rho_m \ , \tag{2.18}$$

$$m_{xt} = m_m + m_x \ \ , \tag{2.19}$$

where V_m is the volume of a single module, t_m is the thickness of the module diameter, m_m is the structural mass of the module, m_x is the mass of a general module structure (it can either be the service module, the recovery module or the payload module), and m_{xt} is total module mass.

Fins

From the REXUS standard fin dimensions [71], the main geometric measurements of the fins were used to build a set of equations dependent on the diameter of the rocket.

$$c_r = K_{cr} D_{rocket} \ , \tag{2.20}$$

$$c_{tip} = \frac{K_{c\,tip}}{2} \ , \tag{2.21}$$

$$F_{ss} = K_{Fss} D_{rocket} \ , \tag{2.22}$$

$$m_{fins} = n_{fins}(A_{fins})\rho_{fins} t_{fins} \ , \tag{2.23}$$

where c_r is the fin root chord, c_{tip} is the fin tip chord, F_{ss} is the fin semi span, m_{fins}, the total mass of the finset, K_{cr} a constant of the fin root cord, $K_{c\,tip}$ a constant of the fin tip chord, Fss a constant of the fin semi span, and, m_{fins} is the mass of the fins. These equations were confirmed to be in accordance with the REXUS standard fins, a rocket with comparable characteristics, as converged in the benchmark case study in Section 5.3.

Nozzle

The nozzle was designed using the engine dimensioning calculation procedure in [52]. Equations to calculate the nozzle throat area, exit area, length, mass, and the length and mass of the nozzle convergent section, here named as "nozzle adapter", were derived as

$$A_t = \frac{c_{del} T_{vac}}{P_c g_0 I_{sp_V ac}} \ , \tag{2.24}$$

$$A_e = \varepsilon A_t \ , \tag{2.25}$$

$$L_n = 0.8 \left(\frac{2R_e - 2R_t}{2\tan(\alpha)} \right) \ , \tag{2.26}$$

$$L_{na} = \frac{(D_{Rocket} - 2t_{bt}) - 2R_t}{2\tan(\alpha_{convergent})} \ , \tag{2.27}$$

$$m_{na} = \rho_{na} V_{na} \ , \tag{2.28}$$

$$m_n = \rho_n m_n \ , \tag{2.29}$$

where c_{del}, nozzle exhaust velocity, T_{vac}, average thrust in vacuum, P_c, average internal casing pressure, g_0, gravitational acceleration at sea level, $I_{sp\,vac}$, specific impulse in vacuum, A_t, nozzle throat area, A_e, nozzle exit area, L_n, nozzle length, L_{na}, nozzle adapter length, R_e, nozzle exit radius, R_t, nozzle radius, α, nozzle angle, $\alpha_{convergent}$, t_{bt}, body tube thickness, ϵ, nozzle expansion ratio, nozzle convergent section angle, m_{na}, nozzle adapter mass, ρ_{na}, nozzle adapter density, ρ_n, nozzle density, V_{na}, nozzle adapter volume.

Rocket Motor

The rocket motor was sized using a set of equations designed to model the geometric properties of a solid rocket motor (SRM). This choice of propulsion system will be justified later in Section 2.4.

$$L_g = L_c - 2t_c \ , \tag{2.30}$$

$$R_{gi} = R_{go} - t_g \ , \tag{2.31}$$

$$R_{go} = R_{rocket} - t_c \ , \tag{2.32}$$

$$m_p = \pi L_g (R_{go}^2 - R_{gi}^2)\rho_p \ , \tag{2.33}$$

$$m_c = \pi (R_c^2 - (R_c - t_c)^2)(L_c - 2t_c) + 2\pi t_c R_c^2 \ , \tag{2.34}$$

where L_g, is the grain length, L_c is the casing length, t_c is the casing thickness, R_{gi} is the grain inner radius, R_{go} is the grain outer radius, m_p is the propellant mass, ρ_p is the propellant density, and R_c is the casing radius.

Rocket Sizing

A further set of equations was derived to calculate a few important remaining parameters: the body tube length L_{bt}, volume V_{bt} and mass m_{bt}, the rocket total lift-off mass m_0, the rocket structural mass m_s and the rocket empty mass m_f.

$$L_{bt} = L_{rocket} - L_{nc} - 3L_m - L_n - L_{na} \ , \tag{2.35}$$

$$V_{bt} = \pi(R_{rocket}^2 - (R_{rocket} - t_{bt})^2)L_{bt} \ , \tag{2.36}$$

$$m_{bt} = \rho_{bt} V_{bt} \ , \tag{2.37}$$

$$\begin{aligned} m_0 = \ & m_{nc} + m_{tip} + m_{PLt} + m_{Et} + m_{St} + m_{Rt} + m_{fins} + m_{bt} + \\ & + m_n + m_{na} + m_w + m_p + m_c \end{aligned} \ ,$$

$$\begin{aligned} m_s = \ & m_{tip} + m_{nc} + m_{mPL} + m_{mE} + m_w + m_{St} + m_{Rt} \\ & + m_{bt} + m_c + m_{fins} + m_n + m_{na} \ , \end{aligned} \tag{2.38}$$

$$m_f = m_0 - m_p \ , \tag{2.39}$$

where L_{bt}, is the body tube length, V_{bt} is the body tube volume, m_{bt} is the body tube mass, m_0 is the rocket initial mass, m_s is rocket structural mass and m_f is the rocket empty mass.

2.2.1 Mass and Sizing Model

A model was created from the equations presented in the previous section. It was subdivided into six smaller sub-models or components, each of them responsible for the dimensioning process of a rocket main part: nose cone, modules, fins, nozzle, body tube, and SRM sorted by the model execution order. Additionally, a final component was also created to calculate a few general properties, namely, the rocket's initial mass, empty mass, structural mass and structural factor. To consult the complete set of equations used for the mass and sizing calculations for each component, please refer to the Appendix B. Figure 2.2 gives a simplified view of the rocket main parts included in the model, highlighting the inputs, outputs, and main components.

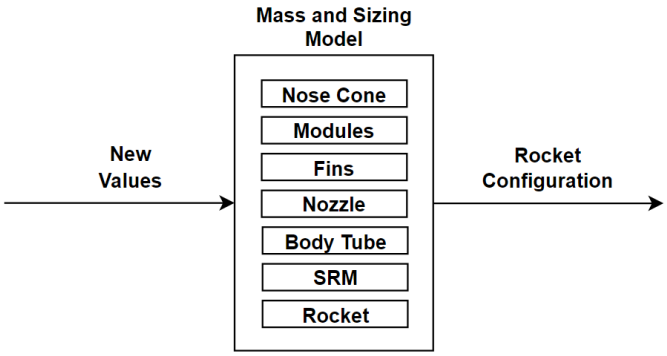

Figure 2.3: Mass and sizing simplified schema highlighting the inputs, outputs and inner components of the model.

2.3 Aerodynamics

During its flight, a sounding rocket has to withstand complex interactions with the atmosphere [72]. In this section, the most prominent aerodynamic properties will be presented, following the selection of two main aerodynamic components, namely, the nose cone and fin configurations, and finally, a aerodynamics model will be proposed.

2.3.1 Aerodynamic Properties

During the atmospheric phase, a rocket is subjected to a number of different aerodynamic properties: lift, L, drag, D, friction, dynamic pressure, q, heating, acoustics, and stability, all of which depend on the rocket geometry and size, free-stream relative velocity, V, atmospheric density, ρ, Reynolds number, R_e, and Mach number, M [72].

Lift is the component of the aerodynamic force in the direction perpendicular to the body relative air velocity that is generated from a pressure difference between its surfaces [72], defined as

$$L = \frac{1}{2} C_L \rho A V^2 \ , \tag{2.40}$$

where C_L is the lift coefficient and A is the frontal cross sectional area. When designing the body shape of the rocket, it is crucial to assess its behaviour under zero lift conditions. Typically, it is chosen an axisymmetric geometry that guarantees that the coefficient of lift is null for a zero angle of attack ($C_L = 0$, $\alpha = 0$) and also that lift will only be induced either during pitch events, where the rocket experiences a non-zero angle of attack, or under small flight perturbations, where the induced lift will counteract small variations in the angle of attack, thus helping to stabilise the rocket (if the static margin is positive) [73].

Drag is the component of the aerodynamic force that opposes the motion of an LV, enforcing significant negative effects during atmospheric flight, such as energy losses and heating issues [72]. Figure 2.4 shows several types of drag, depending on their source: skin friction drag, body pressure drag, parasitic pressure drag, fin-body interference drag, fin tip vortex related drag and base drag.

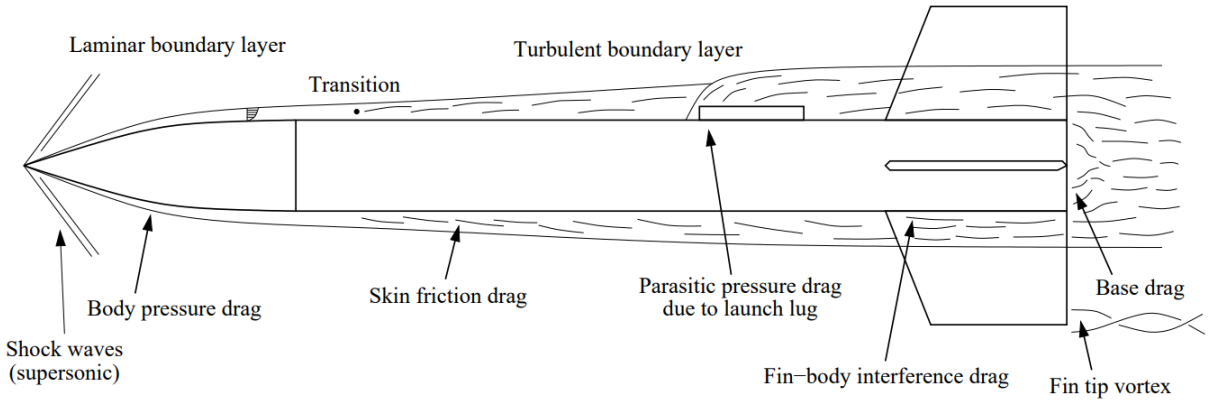

Figure 2.4: Main sources of drag of a rocket [74].

All these drag sources have complex interactions between each other, and although they directly influence the overall drag force acting on the rocket, only the most significant were considered in the model to reduce the number of variables and achieve the maximum computational efficiency. For now, only a general definition of the drag force will be formally defined [75]:

$$D = \frac{1}{2} C_D \rho A V^2 \ , \tag{2.41}$$

where C_D is the drag coefficient.

Another parameter which is related to drag that holds special importance in terms of the assessment of the structural aerodynamic loading sustained by an LV is the dynamic pressure , q, [72]:

$$q = \frac{1}{2} \rho V^2 \ , \tag{2.42}$$

During its ascent phase, the rockets' acceleration and associated speed increase. As a consequence, the rocket has to withstand strong positive dynamic pressure variations, which need to be limited to avoid potential structural failures due to aerodynamic loading overstress [52].

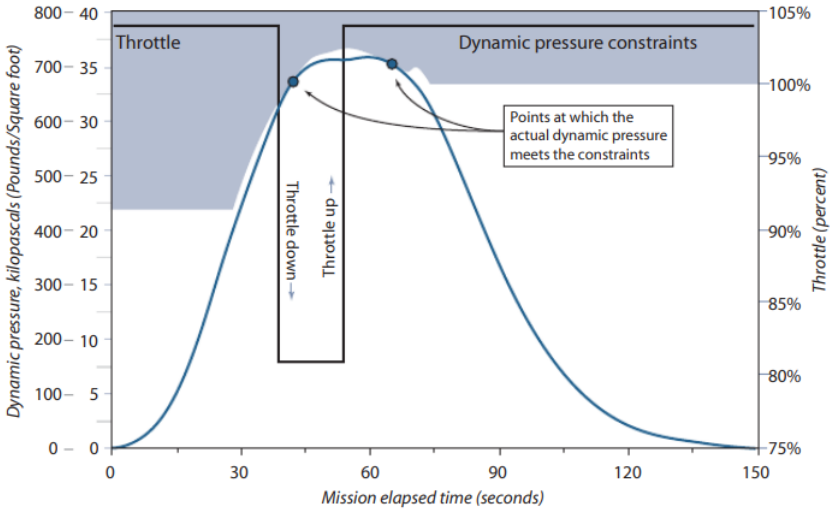

Figure 2.5: Space Shuttle's typical dynamic pressure vs mission elapsed time profile [52].

A good example of the importance of this parameter in the LV design process is portrayed in Figure 2.5, in which a throttle down - throttle up manoeuvre is used in order to comply with dynamic pressure constraints near the max-q point, during a typical space shuttle mission profile [52].

2.3.2 Nose Cone, Tail Fins and Recovery System

In rocket design, the geometric configuration of the nose cone and tail fins has a particularly significant impact on the overall aerodynamic performance of the rocket.

In general terms, a better aerodynamic behaviour will lessen the resulting aerodynamic forces, either longitudinal or lateral, which will then generate reduced structural stresses. This translates into smaller thicknesses of the rocket structure and, ultimately, less weight [52]. Additionally, the presence of smaller

aerodynamic forces has the coupled effect of reducing energy losses throughout the atmospheric flight, leading to less required propellant at lift-off, further minimising the weight of the rocket at launch. Thus, it is of great significance to select the pair of geometries that results in the best compromise in terms of mass, volume, structural strength, manufacturing costs, and aerodynamic performance [52].

Nose Cone

To select the best nose cone configuration, the following criteria will be followed:

- The best transonic behaviour, as the greatest aerodynamic loads are generated under transonic flight regimes, while maintaining a satisfactory behaviour under subsonic and supersonic flight regimes;
- Highest volume-to-mass ratio as it is highly desirable for a nose cone to have the highest volume possible to accommodate the payload while minimising its mass;

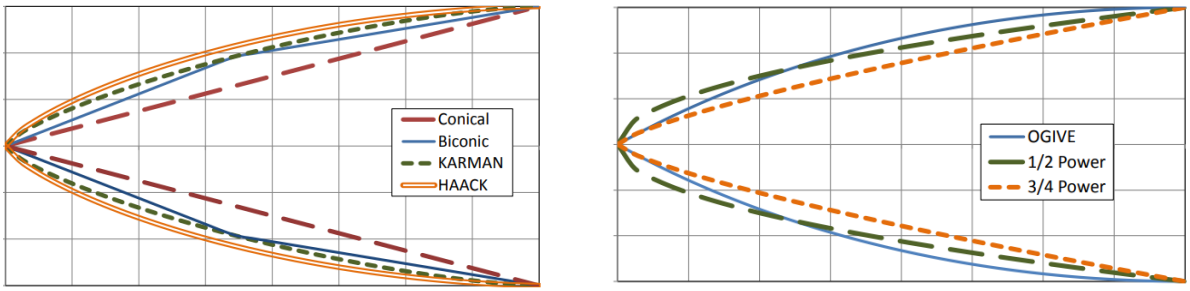

Figure 2.6: Comparison between seven nose typical cone geometric shapes [73].

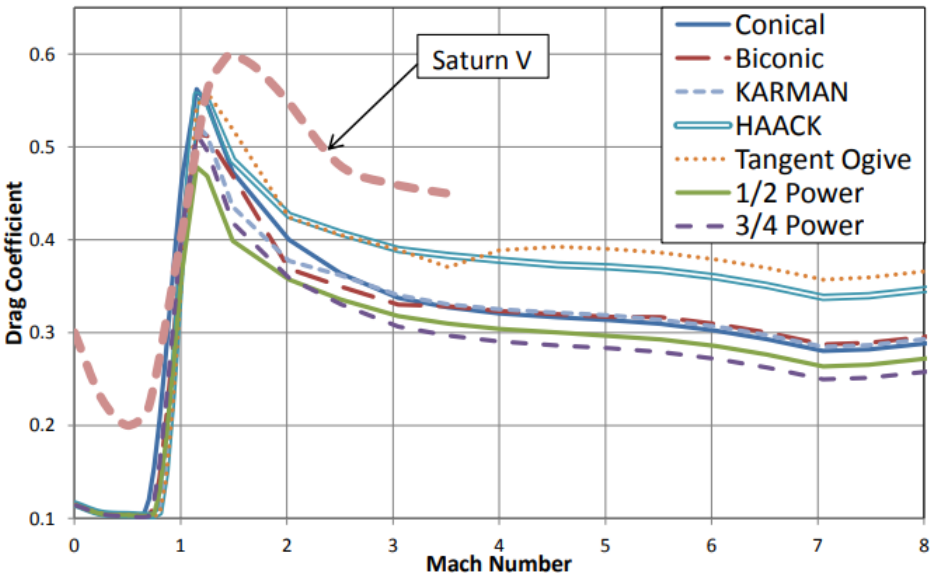

Figure 2.7: Drag coefficient profile for different nose cone configurations [73].

Figure 2.7 presents the drag profiles (drag coefficient curves as a function of Mach number) of the forementioned nose cones presented in Fig. 2.6, compared with Saturn V for perspective. These were obtained by the Missile DATCOM design tool [76] for a nose cone reference model [73]. From this analysis, only two candidates remain: the 1/2 Power and 3/4 Power configurations, because they present

similar performance levels under subsonic conditions and clearly outperform every other configuration of the lot in the transonic, supersonic, and hypersonic flight regimes.

To evaluate the impact that each configuration has in terms of mass and volume, their respective values were compared with the conical configuration, here used as a reference, in Table 2.1

Table 2.1: Nose cone mass and volume analysis. Adapted from [73].

Nose Cone	% Mass Difference	% Volume Difference
Conical	0%	0%
1/2 Power	26%	39%
3/4 Power	12%	18%

The 1/2 Power configuration offers the best volume to mass ratio increase. Additionally, considering it outperforms the 3/4 Power configuration in the transonic region, while presenting a similar performance in the other flight regimes, it is the selected nose cone configuration of the process.

Tail Fins

Tail fins are one of the most influential rocket parts in rocket design. Their main purpose is to give stability to the rocket, allowing it to follow an intended trajectory even under great external destabilising forces [77]. This can only be achieved by placing the centre pressure (CP) below the centre of mass (CM) along the roll axis, so that for every sudden change in the angle of attack, a restoring force acting on the CP is originated (positive static margin), creating a restoring moment and consequently allowing the rocket to recover to its original direction, thus mitigating the perturbation [77]. However, the external placement of the tail fins along the aft. end of the body tube has serious aerodynamic implications that need to be accounted for [77].

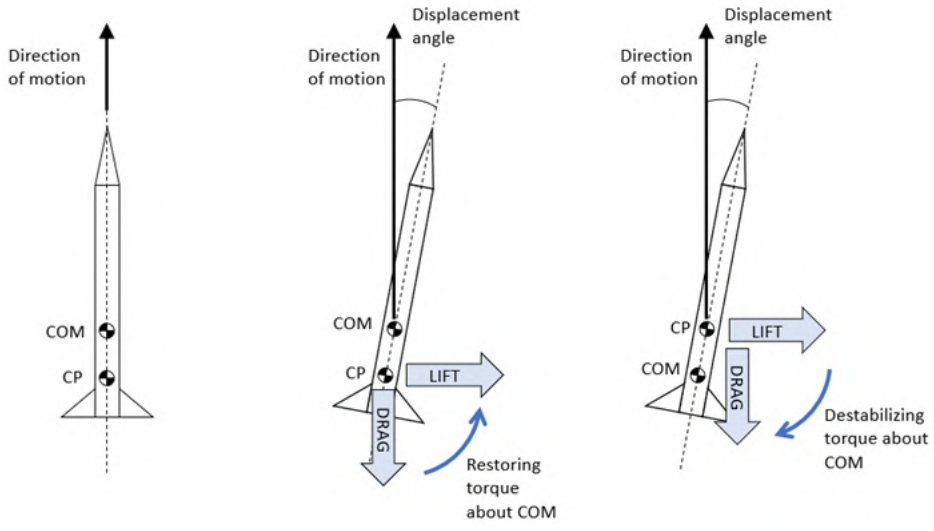

Figure 2.8: Rocket stability and control diagram [78].

Thus, the selection, according to the mission requirements, of the best tail configuration is crucial in finding the optimal rocket design. Several aspects, then, need to be taken into consideration [79]: the fin planform shape, geometry, aspect ratio, and cross-section.

Figure 2.9a presents the following planforms [80]: (a) rectangular, (b) swept, (c) swept tapered, (d)

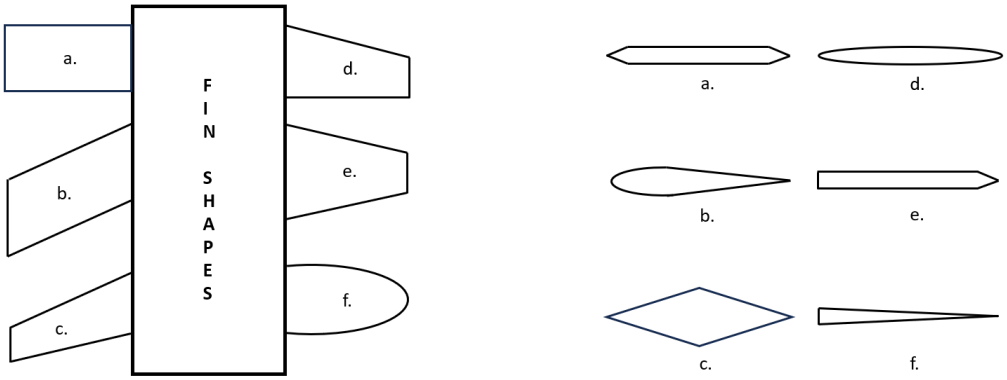

(a) Tail fin planform shapes

(b) Tail fin cross-section shapes

Figure 2.9: Tail fin properties.

clipped delta, (e) trapezoidal, and (f) elliptical; and fig. 2.9b the cross-sections: a) double-diamond, b) NACA, c) single-diamond, d) biconvex, e) hexagonal blunt-base , f) single-wedge.

After thorough analysis of the works of several authors [13, 80–83], the selected tail fin configuration was a swept-tappered planform shape with a symmetrical double-diamond cross-section.

The swept-tappered planform is the planform which pushes the centre of pressure the furthest back along the roll axis, which is crucial for stability.

As for the symmetrical double-diamond cross-section, it ensures that the leading and trailing edges have a sharp end, which is best for supersonic conditions, in aerodynamic terms. Additionally, this design maintains the maximum thickness throughout the full central section of the fin cord, which adds considerable strength and stiffness, thus being less susceptible to vibration and consequently to ”fin flutter” [83].

Recovery System

After reaching its peak altitude, a sounding rocket starts to rapidly descend, gaining excessive speed at increasingly higher rates. Thus, integrating a recovery system is pivotal to ensure a descent with controlled speed, a safe landing, and, finally, a successful recovery for further reuse.

The traditional recovery system is the parachute, which taking advantage of the resulting high drag after inflation, will effectively slow down the rocket, thus controlling the achieved descent rate until a safe terminal speed has been reached.

Although many variations exist, the recovery system being modelled will be a combined drogue-main parachute configuration with side-ejection, which consists in deploying a smaller parachute, named ”Drogue parachute”, at altitudes as high as 15 km [84], to gradually attenuate the rocket at high speed, well within the supersonic region, and then a significantly larger subsonic main parachute, at altitudes between 3 and 7.5 km [85], further increasing the body drag of the rocket until it smoothly reaches terminal speeds of around 5 to 8 m/s [85, 86].

Figure 2.10 illustrates a complete sounding rocket recovery sequence divided in seven stages: from the moment the drogue parachute is deployed in S1 to the final low speed, fully inflated, and stabilised

descent phase, in S7.

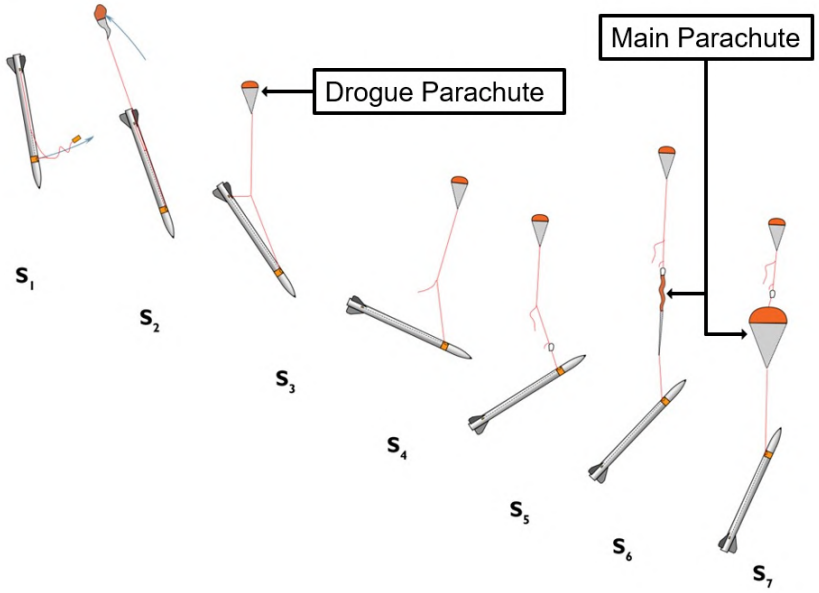

Figure 2.10: Schematics of a complete sounding rocket parachute recovery sequence from drogue parachute deployment, in S1, to the main parachute fully inflated, in S7. Adapted from [85].

2.3.3 Aerodynamic Model

This model was designed to estimate the aerodynamic behaviour of the rocket at each operating state. Its simplified diagram is illustrated in Fig. 2.11.

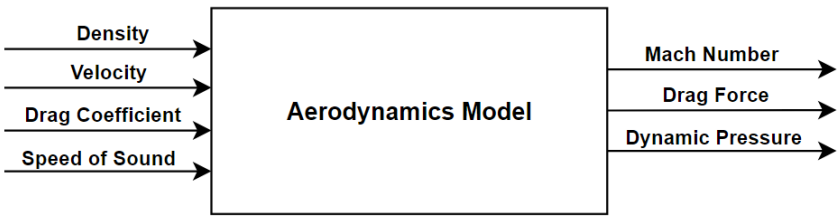

Figure 2.11: Aerodynamics model diagram.

A first approach was made following the works of several authors [87–91] by first calculating the various components of the coefficient of drag from empirical relations based on its geometric dimensions. However, the obtained results were not faithful to the expected physical behaviour since the applied empirical relations had been derived for high-power model rockets, so, they could not be applied to a suborbital rocket with roughly 5 to 10 times their size. For a more detailed explanation on this first model formulation, please refer to Appendix B.6.

A second aerodynamics model was then drawn using a simpler formulation. Only three sources of drag were considered in the calculation of the total zero lift drag coefficient, Cd_0: nose cone drag coefficient, Cd_{nc}, base drag coefficient, Cd_b and fins drag coefficient, Cd_f, as

$$Cd_0 = Cd_{nc} + Cd_b + Cd_f. \tag{2.43}$$

The nose cone drag coefficient values were calculated through a direct interpolation of the data points of the 1/2 power nose cone drag coefficient profile presented in Figure 2.7 retrieved from the Missile DATCOM software [73]. The base and fin drag coefficients were calculated through empirical relations based on several atmospheric parameters, the geometric dimensions of these components and the mach number of the rocket [92]. Figure 2.12 portrays the Cd_0 profile of the model compared with the Saturn V for perspective.

Ultimately, the Cd_0 was used to calculate the drag force applying Equation (2.41) and the dynamic pressure was calculated through Equation (2.42).

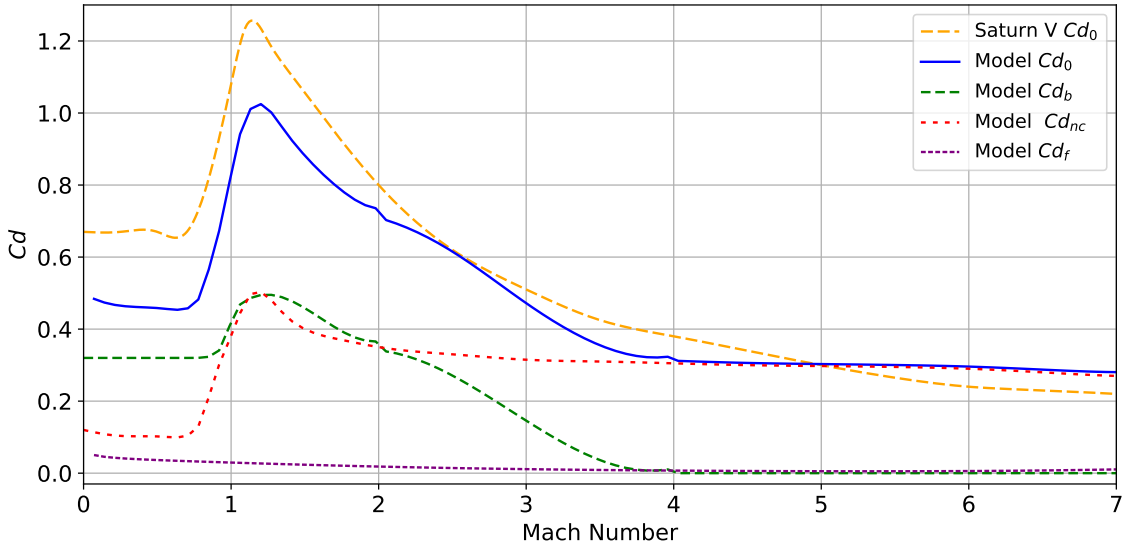

Figure 2.12: Drag profiles of the main components compared with the Saturn V drag profile to give perspective.

Compressible Flow Correction

The previous expressions for C_d are only valid for incompressible flow, thus, their application needs to be extended to cover the compressible flow regime [91].

At subsonic speed ($M_a < 0.8$), the compressible flow correction for the aerodynamic coefficient is defined as

$$C_d = \frac{C_i}{\sqrt{1 - M_a^2}}, \tag{2.44}$$

where M_a is the free stream Mach number. At the transonic region ($0.8 \leq M_a \leq 1.1$), the corrected aerodynamic coefficient is given by

$$C_d = \frac{C_i}{\sqrt{1 - (0.8)^2}}. \tag{2.45}$$

Lastly, at supersonic speed ($M_a > 1.1$), the corrected aerodynamic coefficient is

$$C_d = \frac{C_i}{\sqrt{M_a^2 - 1}}. \tag{2.46}$$

Recovery System Contribution

In order to simulate the presence of the recovery system upon its activation, an additional contribution was introduced to the produced drag.

Table 2.2 presents the main characteristics of the recovery system:

Table 2.2: Recovery system main characteristics. Adapted from [85].

Parameter	Unit	Parachute	
		Drogue	Main
Area	**[m^2]**	0.9	7.28
C_D	**-**	0.3	0.55
Mass	**[kg]**	1.3	0.6
Deployment Altitude	**[km]**	7.5 - 15	3 - 7.5
Expected Inflation Force	**[kN]**	53	25

After the drogue parachute descent altitude is reached, an additional component of drag is calculated as

$$D_{drogue} = \frac{1}{2}\rho v^2 C_{D\,drogue} S_{drogue}\ , \tag{2.47}$$

where D_{drogue} is the drag component due to the drogue parachute, $C_{D\,drogue}$ is the drag coefficient of the drogue parachute, and S_{drogue} is the drogue parachute area.

Similarly, after the main parachute descent altitude is reached, an additional component of induced drag is calculated as

$$D_{main\,parachute} = \frac{1}{2}\rho v^2 C_{D\,main\,parachute} S_{main\,parachute}\ , \tag{2.48}$$

where $D_{main\,parachute}$ is the drag component due to the main parachute, $C_{D\,main\,parachute}$ is the drag coefficient of the main parachute, and $S_{main\,parachute}$ is the main parachute area.

2.4 Propulsion

At first sight, the main purpose of the propulsion system might be seen as solely to generate the required propulsive force to put an LV in motion so that it can prescribe a desired mission profile. Yet, given certain mission requirements, a careful choice of the most adequate propulsion system might maximise the performance and safety, as well as, minimise operational risks and overall costs of the entire mission. Thus, the right selection of a propulsion system is of pivotal importance [51].

Propulsion System Selection

Within the jet engine class, duct engines, commonly known as air-breathing engines, are the best solution for the majority of modern commercial aviation applications. Their working principle assents on using the surrounding medium as the oxidizing agent for the combustion of in-vehicle stored fuels to generate thrust. However, they have strong maximum service ceiling limitations (as an example, 14000 - 17000 m for turbojets and 20000, 30000 and 45000 m at 3, 5 and 12 Mach respectively for ramjets) due to the lack of oxygen concentration with altitude in atmospheric air, thus making them unsuitable for space applications [51]. Alternatively, rocket engines have both the oxidizer and propellant stored inside the vehicle being completely independent of the physical properties of the surrounding medium to sustain normal operating conditions thus making them a suitable option space flight.

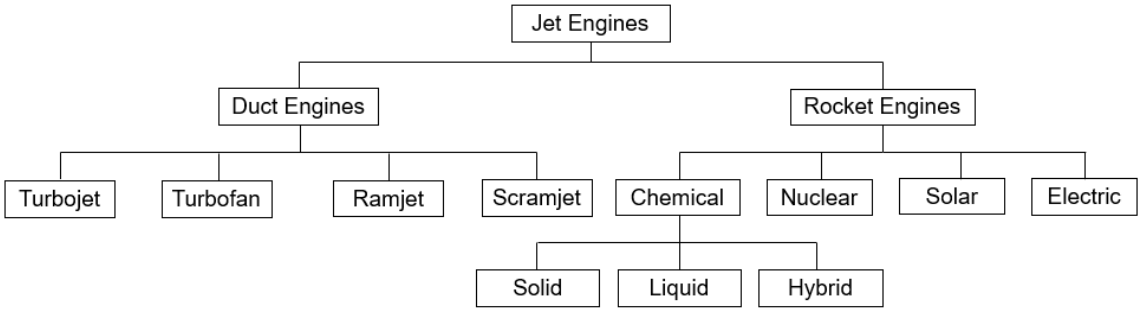

Figure 2.13: Different types of jet engines.

Figure 2.13 portrays the several existing different types of engines within the Jet Engine family.

As other forms of energy supply are still not a proven concept for suborbital flight, namely, nuclear, solar and electric, the only viable option left rests within the Chemical Rocket Engines (CREs) subset [51]. Inside these engines, chemical energy is transformed into heat energy by a high temperature combustion reaction of the solid propellant. High pressurized gases are forced out of the combustion chamber into the nozzle, which acting as an accelerator, allows them to expand, trading static pressure with dynamic pressure, as they steeply accelerate until supersonic speeds have been reached at the nozzle exit [93]. It is precisely the opposing force originated from the described change in linear momentum of the ejected matter at the nozzle that allows the rocket to move forward, thus being commonly known as a propulsive force acting on the center mass of the rocket [51].

Figure 2.14 illustrates the three existing types of this engines based on the propellant physical state: Solid Rocket Motor (SRM); Liquid Rocket Engine (LRE); or Hybrid Rocket Engine (HRE), when propellants in different states are simultaneously used.

LREs are commonly used in heavy rockets because they provide throttling control and engine shut off and re-ignition capabilities, which are essential for space maneuvering. However, these features come at the cost of requiring the installation of complex turbo pumps, valves, high-pressure tanks, and other mechanical parts operating at high rates and temperatures, significantly increasing the complexity of the design and the overall operation and maintenance costs.

In contrast, SRMs are a much simpler choice, fairly easy to operate, highly affordable to manufacture

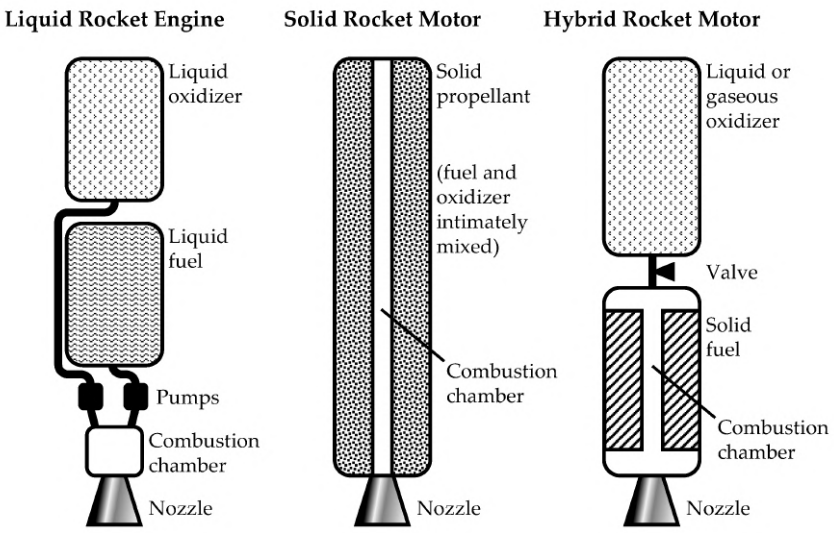

Figure 2.14: Schematic view of CREs [94].

and maintain, with greater fuel volumetric efficiency, although they do not provide throttling control or engine cut-off and re-ignition capabilities.

A modern solution that has already been tested for a wide range of space applications and which simultaneously exploits the advantages of SRMs and LREs is the HRE [95]. By combining within the same propulsion system, a solid propellant with liquid or gaseous oxidizer, it is possible to control the thrust curve for specific periods of time throughout the flight [96]. Although these systems provide high storage safety, prevent inadverted ignitions and allow for high propellant versatility selection, they offer poorer fuel volumetric and combustion efficiency in comparison to SRMs.

Table 2.3: Qualitative comparison of the main characteristics of CREs [95, 96].

Parameter	SRM	LRE	HRE
Throttling Control	☒	☑	☑
Engine Cut-Off and Re-Ignition	☒	☑	☑
Manufacturing and Operating Complexity	Low	High	Medium
Cost	Low	High	Medium
Performance	Low to Medium	High	Medium

From Table 2.3, which summarizes the main characteristics of CREs, it may be concluded that for mission profiles which do not require throttling control or engine cut-off and re-ignition capabilities, which is the case of the majority of single-stage sounding rockets performing suborbital flights, the most advantageous option is the SRM.

Grain Geometry Selection

The grain is a processed solid propellant mass, which normally represents 80 to 94% of its mass [51]. Additionally, it is the grain perforation geometry that directly influences the thrust profile of the engine because it allows the engineers to effectively control the propellant instantaneous burned area along the propelled flight and, consequently, the obtained chamber pressure and produced thrust. This serves to show the importance of choosing a suitable grain perforation when designing a SRM.

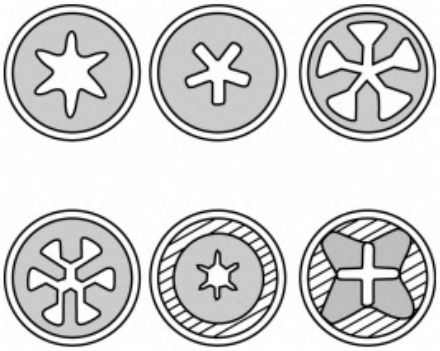

Figure 2.15: Several cross-sections of perforated internal-burning propellant grains [93].

Due to the extensive diversity of existing grain configurations, portrayed in Figure 2.15, other aspects, aside from the geometry, need to be considered in order to make a final decision: best grain compactness possible, minimum erosive burning, minimum unburnt propellant slivers, minimum shift in the centre of gravity [51].

In the suborbital flight context, high burning areas are needed to produce high chamber pressure and thrust levels in the first seconds of the flight in order to place the rocket outside the atmospheric region as soon as possible in order to minimise gravity losses, followed by a period of lower burning areas, lower chamber pressures, and thrust levels in order to minimise excessive speed and their resulting drag losses. Thus, dual-phase or a regressive thrust-time profile are the optimal solutions over neutral or progressive thrust-time profiles [51].

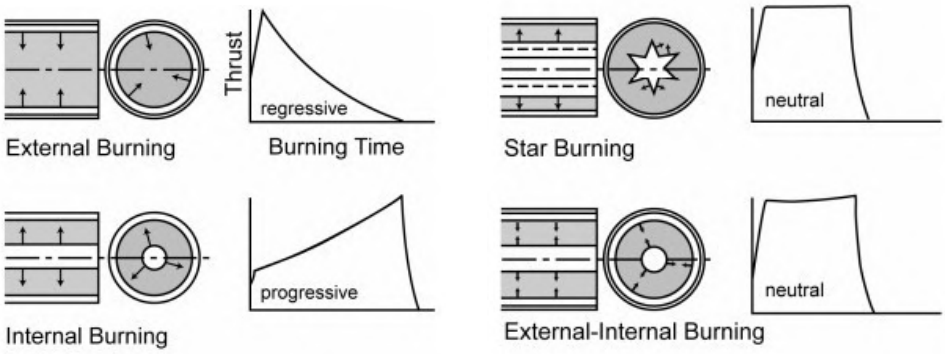

Figure 2.16: Propellant grains and their thrust profile [93].

As the propulsion model is being designed for an MDO application, it is important to avoid highly complex grain configurations because they will most likely present unnecessary burnback and internal ballistic evaluation challenges, which, in the end, will be of minimal consequence to the final optimisation results. Instead, a simpler, mathematically efficient to model configuration was preferred.

Figure 2.16 portrays four of these simpler configurations along with their burnback direction and thrust-time profiles. It was decided to model a propulsion system which mimics the behaviour of an SRM integrated with a cylindrical grain with lateral combustion by sequentially conducting an instantaneous burnback analysis followed by an internal ballistic analysis, i. e., by first evaluating the propellant regression to assess the instantaneous burning areas, given an initial grain radius and a known burn-

ing direction, and afterwards, by using one-dimensional isentropic flow equations [97] to evaluate the resulting chamber pressure and thrust, among other parameters.

2.4.1 Propulsion Model

This model was developed to accurately predict the behaviour of the main physical properties of a SRM under real operating conditions. Its simplified flowchart is depicted in Fig. 2.17, where the main inputs and outputs are listed.

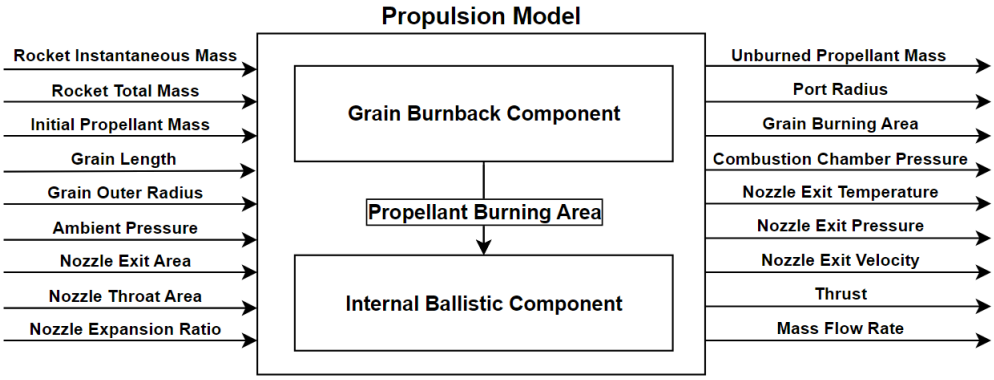

Figure 2.17: Propulsion model diagram highlighting inputs, outputs and inner components.

Grain Burnback Component

First, based on the works of several authors [98–102], a set of analytical equations was assembled to model the grain burnback, i.e, the propellant regression rate and respective propellant burning areas over time,

$$m_{pi} = m_{p0} - (m_0 - m_i) \, , \tag{2.49}$$

$$R_p = \sqrt{\frac{-m_{pi}}{\rho_p \pi L_{grain} + R_i^2}} \, , \tag{2.50}$$

$$A_b = 2\pi R_p L_{grain} \, , \tag{2.51}$$

where m_{pi} is the instantaneous propellant mass, m_{p0} is the initial propellant mass, m_0 is the rocket lift-off mass, m_i is instantaneous rocket mass, R_p is the port radius, ρ_p is the propellant density, L_{grain}, is the grain length, R_i is the grain inner radius, and A_b is the instantaneous burning area.

Internal Ballistic Component

Then, using the propellant burning area as the main input, a second set of equations was assembled to model the internal ballistic behaviour of the motor, namely the combustion chamber pressure and the thrust, using one-dimensional isentropic flow equations [97], as

$$T_e = T_t(1 + \frac{\gamma - 1}{2} M_e^2)^{-1} \ , \tag{2.52}$$

$$P_t = \left[\frac{a \rho_p A_b}{C_D A_t} \right]^{\frac{1}{1-n}} \ , \tag{2.53}$$

$$P_e = P_t(1 + \frac{\gamma - 1}{2} M_e^2)^{\frac{-\gamma}{\gamma - 1}} \ , \tag{2.54}$$

$$V_e = M_e \sqrt{\gamma R T_e} \ , \tag{2.55}$$

$$\dot{m} = -C_D A_t P_t \ , \tag{2.56}$$

$$Thrust = \dot{m} V_e + (P_e - P) A_e \ , \tag{2.57}$$

where a is the burn rate coefficient, C_D is the nozzle discharge coefficient, A_t is the nozzle throat area, n is the propellant ballistic exponent, T_e is the nozzle exit temperature, T_t is the nozzle throat temperature, γ is the gas specific heat ratio, M_e is the nozzle exit mach number, P_e is the nozzle exit pressure, P_t is the internal casing total pressure, V_e is the nozzle exit velocity, R is the universal gas constant, and P is the atmospheric pressure.

2.5 Structures

One of the major challenges throughout the rocket design optimisation process is to guarantee that every candidate rocket configuration, will withstand beyond all the expected internal and external loading for the intended mission profile.

The structural challenge resides in the fact that increasing structural stiffness and strength, although highly desirable, is highly dependent on increasing the material thickness, thus, the overall structural mass and the manufacturing cost. One way to address this issue, is to test the application of different structural aerospace materials with enhanced physical properties only in major critical rocket components. However, these solution poses two main difficulties: typically, the better the material's structural properties, higher its manufacturing costs; and blindly conducting real structural testing under a controlled environment might still significantly increase the overall production cost of the rocket;

Thus, integrating a structural analysis model at the preliminary stage of the design process plays a crucial role in finding the perfect balance between material selection and its required thickness in order to engineer the most lightweight and cost-effective rocket design configuration possible which still complies with all structural constraints.

A simple model was built to test the occurrence of two critical phenomena during flight: buckling of the body tube and fin flutter.

2.5.1 Buckling

In cylindrical thin shell structures subject to high compressive forces, such as the rocket body tube, buckling is a common phenomenon. It occurs when a structure undergoes axial compressive forces be-

yond their critical point, deforming into a configuration with compromised structural integrity and weakened physical properties, such as strength and stiffness, consequently no longer meeting the initial design's structural requirements. Therefore, it is crucial to integrate a buckling analysis to the design process to guarantee that the buckling critical stress will not be exceeded, for any in-flight loading condition.

The linearised buckling equation for the critical stress of a thin elastic cylindrical shell is given by [103]

$$\sigma_{crit} = \frac{\gamma E}{\sqrt{3(1-v^2)}} \left(\frac{th}{R}\right) , \tag{2.58}$$

where E is the cylindrical shell Young modulus, R its radius, th its thickness, v the material Poisson's ratio and γ a multiplication factor given by

$$\gamma = 1 - 0.901\left(1 - e^{-\phi}\right) \quad \text{with} \quad \phi = \frac{1}{16}\sqrt{\frac{R}{th}} . \tag{2.59}$$

Consequently, the critical axial load for buckling, L_{crit}, may be calculated by simply multiplying it by the cross-sectional area of the sell as

$$L_{crit} = \sigma_{crit}\pi((R^2) - (R - th)^2) . \tag{2.60}$$

Additionally, it is standard practice to apply a factor of safety in every major structural analysis, which ensures that a safety margin will prevent structural failure within operation conditions. For this buckling analysis, a safety factor of 1.4 will be applied, in accordance with the structural design requirements and factors of safety for spaceflight hardware defined by NASA [104].

2.5.2 Fin Flutter

Another well-documented phenomenon that might lead to structural failure that cannot be overlooked is fin flutter [105]. This results from combined elastic bending and torsion events originated by the interaction with the atmospheric air stream, which might excite the tail fin structure when exceeded a certain air stream velocity value, called flutter velocity V_f, matching its natural frequency, leading to amplified oscillations that might end up surpassing the deformation levels tolerated by the stiffness of the material and, finally, undermining its structural integrity [106].

Following the Flutter Boundary Equation [107], it is possible to calculate the flutter velocity as

$$V_f = a\sqrt{\frac{G_E}{\frac{YAR^3}{(t/c_r)^3(AR+2)}\left(\frac{\lambda+1}{2}\right)\left(\frac{P}{P_0}\right)}} , \tag{2.61}$$

where a is the speed of sound at an altitude where the rocket reaches maximum velocity, G_E is the effective shear modulus of the tail fins (for isotropic materials $E = 2G(1+v)$), AR is the aspect ratio of the tail fins, P_0 is the atmospheric pressure at sea level, P is the atmospheric pressure at the reference altitude of the speed of sound, t is the tail fin thickness, c_r is the tail fin root cord, and λ is the tail fin

tapper ratio. Y is a constant value given by [106]

$$Y = \frac{24\epsilon\gamma P_0}{\pi} \ , \tag{2.62}$$

where ϵ is the distance of the fin centre of mass behind the fin quarter-chord and γ is the specific heat air ratio (typically it is considered to be equal to 1.4 [51]).

2.5.3 Structural Model

After a brief theoretical analysis of two key structural events, namely, buckling and fin flutter, a model was created to assess the structural integrity of the rocket along the flight profile. First, given a pair of drag and thrust forces, the model calculates the resulting compressive loading at the body tube cross-sectional area. Then, it compares it with the critical buckling stress in order to evaluate if, at any moment in time, the rocket was subject to such a loading condition for buckling to occur, given the previously established safety factor of 1.4.

Additionally, the fin flutter velocity is also monitored throughout the entire flight profile in order to evaluate if the structural integrity of the fins remains unharmed, as this is the pivotal rocket component for stability.

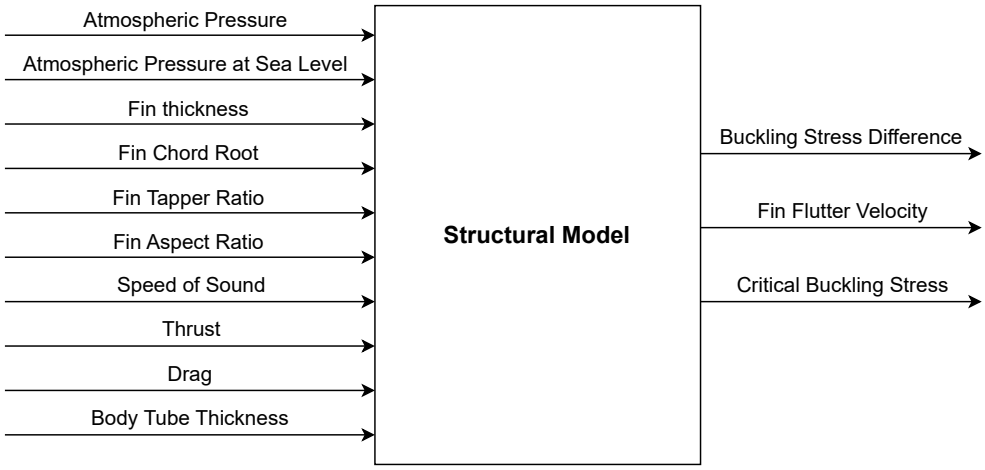

Figure 2.18: Structural model diagram highlighting inputs and outputs.

2.6 Atmosphere

During its ascent, an LV undergoes aerothermal loads that directly depend on the thermodynamic properties of the atmosphere, which are the by-product of the chemical composition of the various atmospheric layers of gases, solar activity and planetary gravity, rotation and magnetic field [108]. At relatively low altitudes (below 15 km), the atmosphere can be considered to be in thermal equilibrium. However, this does not remain true for higher atmospheric layers, where all thermodynamic properties are strongly affected by altitude [108].

Although technologically possible depending on the level of resources at our disposal, it is completely unrealistic, at an academic level, to have access to real live data of the atmospheric properties for each trajectory simulation. Thus, it is necessary to create an atmospheric model which will feed standard values of the most common atmospheric parameters to multiple other models, such as aerodynamic, propulsion, and flight dynamics [108].

2.6.1 Atmospheric Model

Following the 1976 U.S. Standard Atmosphere Convention [109] for the altitude range of $0 \leq h \leq 86$ km and the 1962 U.S Standard Atmosphere Convention [110] for higher altitudes, a first approach was conducted in order to build this model by adapting the methodology in [108].

Assuming thermodynamic equilibrium and constant or linear temperature variation in the fist layers of the atmosphere, the temperature distribution with altitude was defined as

$$T = T_i + a(h - h_i) \ , \tag{2.63}$$

$$\text{with } a = \frac{dT}{dh} = -\frac{(n-1)}{n}\frac{g}{R} \ , \tag{2.64}$$

where the subscript i refers to the reference quantities at the beginning of each layer, n is the polytropic exponent (in adiabatic conditions $n = \gamma$, the specific heat ratio), g the gravitational acceleration, R is the specific gas constant and a is the thermal lapse rate, a crucial parameter which determines the stability of hydrostatic equilibrium within the layer ($a < 0$ means decreasing temperatures with altitude and thermal stability while $a > 0$ means increasing temperatures with altitude and thermal instability).

From the temperature distribution, it was possible to define the atmospheric pressure, P_a and atmospheric density, ρ, considering that the gravitational acceleration varies with altitude:

$$g = g_0 \left(\frac{r_0}{r_0 + h}\right)^2 \ , \tag{2.65}$$

$$p = p_i \left[1 + \frac{a(h - h_i)}{RT_i}\right]^{-\left\{\frac{g_0}{aR}\left[1+\beta\left(\frac{T_i}{a}-h_i\right)\right]\right\}} e^{\frac{\beta g_0}{aR}(h-h_i)} \ , \tag{2.66}$$

$$\rho = \frac{p}{RT} \ , \tag{2.67}$$

where r_0 is the earth radius and $\beta = \frac{2}{r_0}$.

Additionally, a non-dimensional parameter commonly used to distinguish the flow regime in which a moving LV actually is, the *Knudsen number*, K_n, was introduced as the ratio between the mean free path of the flow undisturbed molecules, λ, and the characteristic length of the vehicle, l_c,

$$K_n = \frac{\lambda}{l_c} \tag{2.68}$$

Under this parameter, there are several reference values for each flow regime:

$$\begin{cases} \text{Continuum flow,} \quad \text{if} \quad K_n \leq 0.01, \\ \text{Transitional flow,} \quad \text{if} \quad 0.01 < K_n < 10, \\ \text{Free-molecular flow,} \quad \text{if} \quad 10 \leq K_n \end{cases} \tag{2.69}$$

Then, following an alternative methodology adapted from the *OpenAeroStruct Python* library was followed [111]. In this new version of the model, arrays with the values of each atmospheric parameter retrieved from the standard atmosphere convention tables [109, 110] were created as plotted in Fig. 2.20.

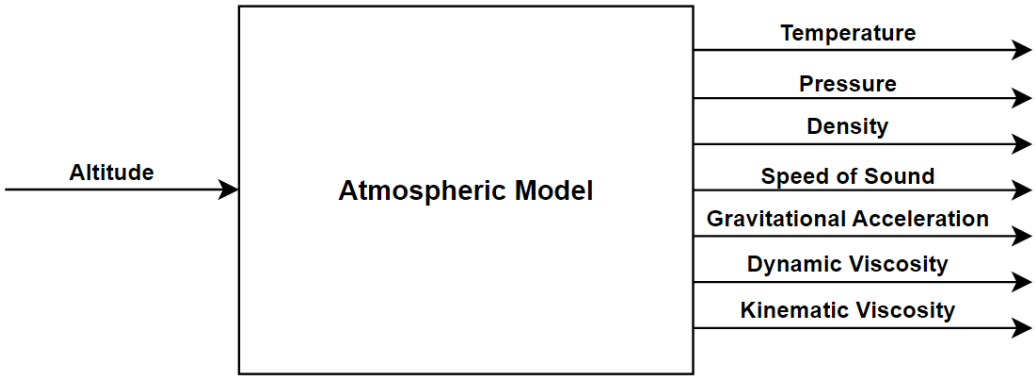

Figure 2.19: Atmospheric model diagram highlighting inputs and outputs.

By interpolating the altitude value (model input) using the *Akima1DInterpolator* class imported from the *Scipy Python* library [112, 113], it was possible to find the respective values of all atmospheric parameters for each particular altitude, namely, temperature T, pressure P_a, density ρ, speed of sound c, gravitational acceleration g, dynamic viscosity μ, and kinematic viscosity k.

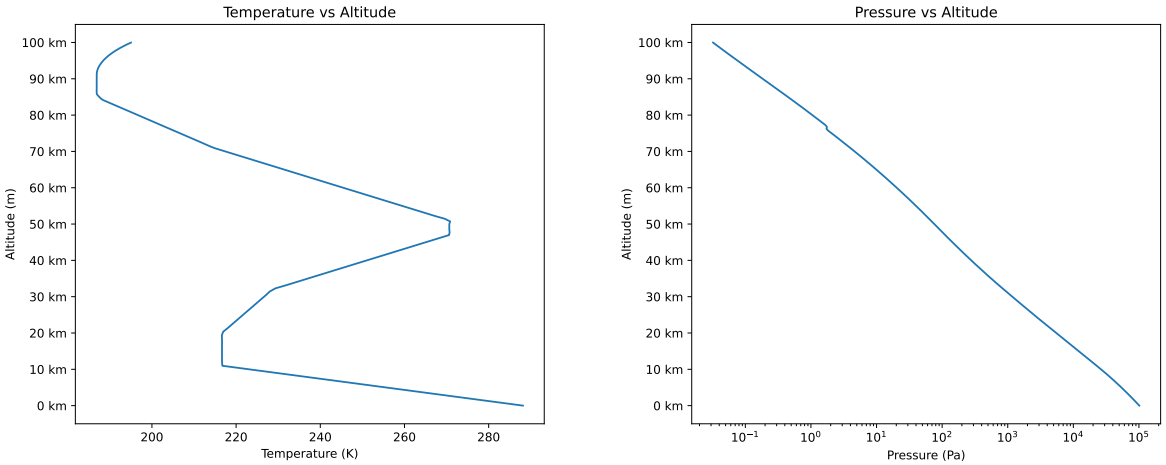

(a) Temperature distribution with altitude.

(b) Pressure distribution with altitude.

Figure 2.20: Atmospheric properties.

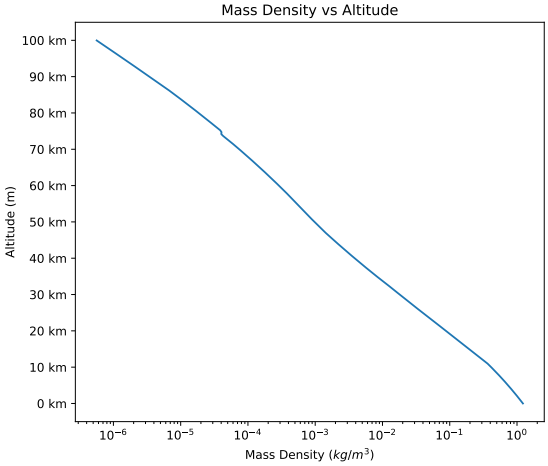

(c) Density distribution with altitude.

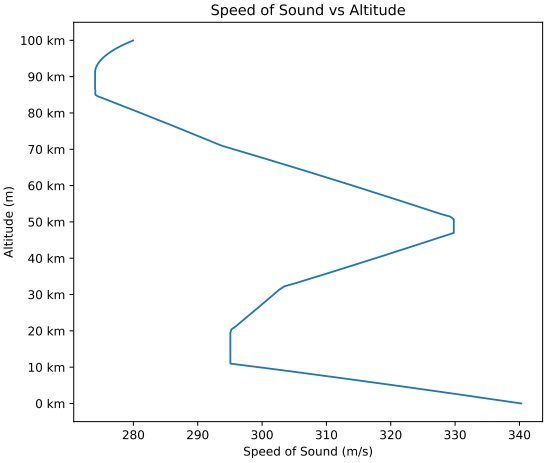

(d) Speed of sound distribution with altitude.

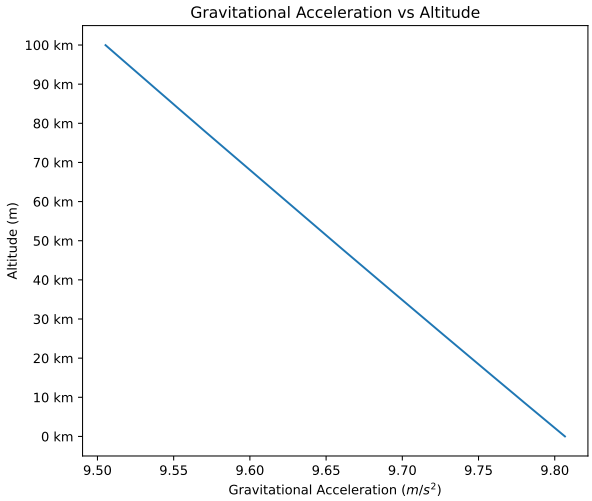

(e) Gravitational acceleration distribution with altitude.

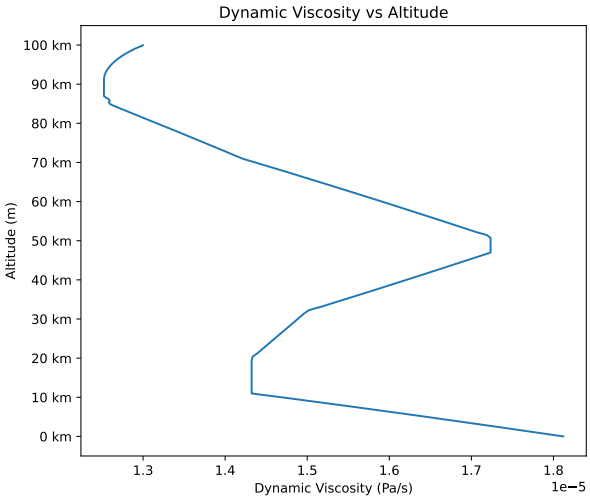

(f) Dynamic viscosity distribution with altitude.

Figure 2.20: Atmospheric properties.

2.7 Flight Dynamics

To successfully determine the prescribed trajectory of an LV it is crucial to rigorously understand its dynamic behaviour. Thus, it is necessary to define a set of flight dynamics equations, commonly known as equations of motion, capable of translating the complex interactions between the rocket, the atmosphere and any other external factors with active influence on the rocket into formal mathematics [114].

In order to reduce the number of state variables for simplicity and computational cost efficiency, a 2 DoF plane model was preferred rather than more complex 3 DoF, 4 Dof, 5 DoF or even 6 Dof models. Accordingly, the following assumptions were made:

- The rotational motion of the LV was not considered in the calculation of the trajectory flight path. Hence, it was rather considered that the acting forces were applied in the centre of mass of the

rocket throughout the flight, as illustrated in Fig. 2.24;

- The thrust vector, $\vec{T}$, is always aligned to the velocity vector, $\vec{v}$, the aerodynamic drag vector, $\vec{D}$ has the opposite direction to $\vec{v}$ and the lift vector, $\vec{L}$, is perpendicular to $\vec{v}$;
- The Weight vector, $\vec{W}$ is always pointing to the center of the Earth;
- The rocket is assumed to be a rigid body with variable mass;
- Expected effects from the rotation of the Earth, such as the Coriolis effect and centripetal acceleration are disregarded due to their impact being considered negligible for the suborbital flights under study. The curvature of the Earth was disregarded due to the small downrange expected values (30 to 60 km) in comparison to the radius of the Earth (6378 km measured at the equator, 6371 km at the poles);

Thus, the flight dynamics of the rocket can be reduced to the following set of equations, which determine the time rate of change of four variables: velocity, v, flight path angle, γ, altitude, h, and downrange, x [114]:

$$\dot{V} = \frac{T}{m}\cos\alpha - \frac{D}{m} - g\sin\gamma \,, \tag{2.70}$$

$$\dot{\gamma} = -\left(\frac{g}{V} - \frac{V}{R_e + h}\right)\cos\gamma + \frac{T}{m}\sin\alpha \,, \tag{2.71}$$

$$\dot{x} = V\cos\gamma \,, \tag{2.72}$$

$$\dot{h} = V\sin\gamma \,, \tag{2.73}$$

Figure 2.21 portrays the typical flight dynamics states variables and acting forces during space flight.

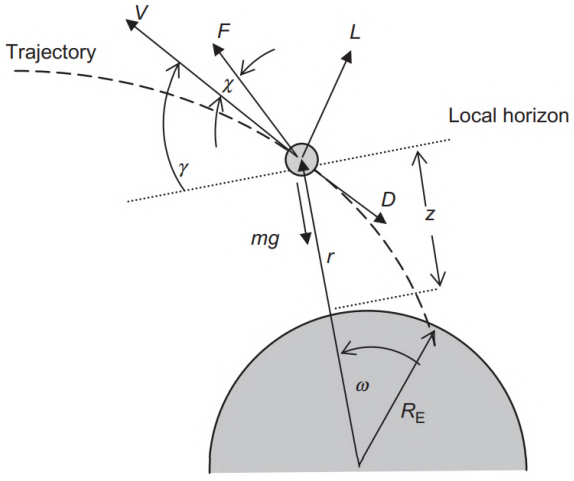

Figure 2.21: Flight Dynamics state variables and acting forces [114].

2.7.1 Flight Dynamics Model

Following the 2 DoF flight dynamics system previously presented, a flight dynamics model was created to be integrated in the trajectory model, at a higher level.

This flight dynamics model is responsible for handling four state variables (downrange, x, altitude, h, velocity, v, pitch angle, γ, and also their time derivatives, respectively: $\dot{x}$, $\dot{h}$, $\dot{v}$ and $\dot{\gamma}$. This bears particular importance because these are the state variables which keep track of the progress of the trajectory integration process at each point in time. Figure 2.22 portrays the flight dynamics model, its inputs and outputs.

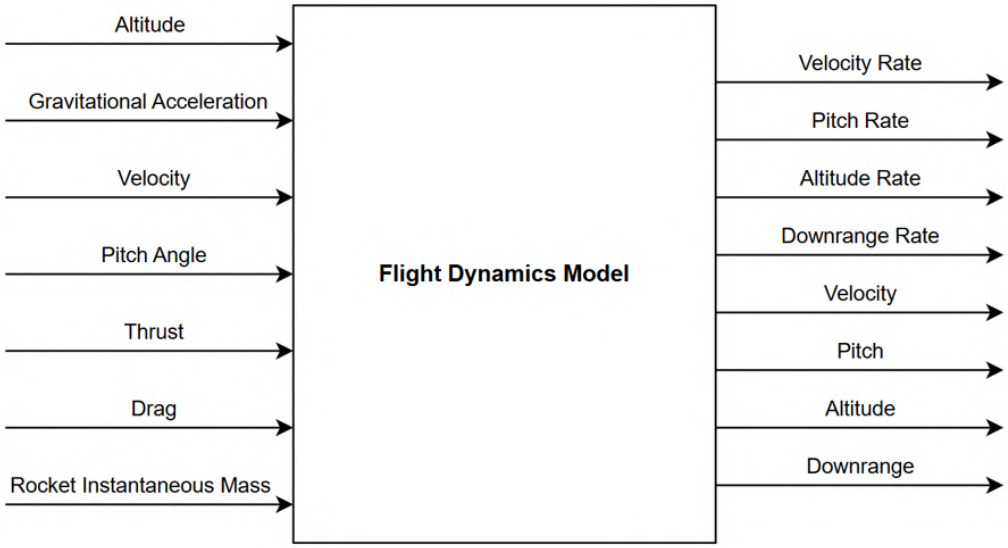

Figure 2.22: Flight dynamics diagram highlighting inputs and outputs.

2.8 Trajectory

In order to place a desired payload at a specific altitude, an LV needs to follow a carefully planned flight profile, taking into account the safety and operational constraints, adverse atmospheric conditions and any unforeseen technical malfunctions, aimed at minimising the overall mission costs.

In the case of sounding rockets, the trajectory can be divided into four main different flight phases: lift off, pitch over manoeuvre, gravity turn and descent.

Lift off vertical flight : Although it is relatively common among sounding rockets to lift-off with a launching angle between 75 ° to 85 ° from a launch rail, immediately starting a gravity turn, it is a standard procedure for the first flight phase to be a vertical powered ascent. During this phase, the rocket gains as much speed and altitude in the shortest amount of time as possible, while maintaining a zero angle of attack to reduce gravity and drag energy losses [52]. After a few seconds of flight time, the rocket is already several hundred meters high with enough speed and altitude to have cleared service towers or any other infrastructure, then proceeding to the pitch over manoeuvre.

Pitch over manoeuvre :

The initial vertical flight, although necessary to quickly gain altitude and speed, proves to be far from optimal after a few seconds of flight time as the gravity energy losses start to have a significant toll, so the solution is to smoothly transition to a gravity turn in which the rocket gradually turns around it's transverse axis in a gravity aided manoeuvre, minimising energy losses and, ultimately, optimising fuel consumption [52]. The aim of this short flight phase is solely for the rocket to produce a small pitch angle, which dictates the beginning of the gravity turn.

By using movable fins, gimbled thrust, vernier thrusters, thrust vanes or other means of active attitude flight controls, as illustrated in Fig. 2.23, it is possible to induce a moment applied to the rocket centre of mass resulting in an angular velocity around the rocket's transverse axis, making it gently pitch towards the desired flight path angle.

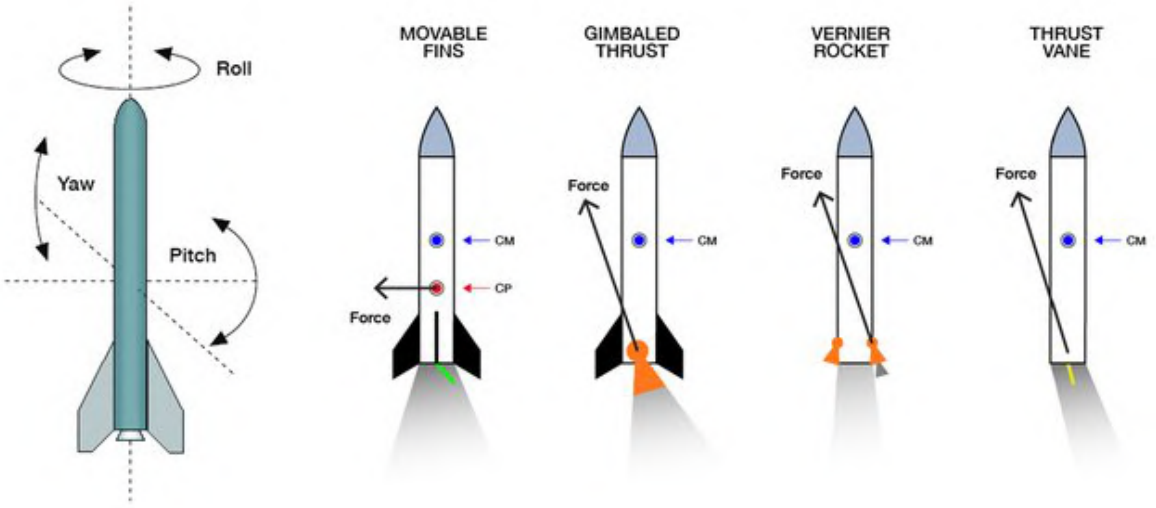

Figure 2.23: Rocket active attitude control systems [115].

During this manoeuvre, the rocket undergoes small angles of attack, which potentially might cause high structurally demanding transverse loads; therefore, it should be performed under low dynamic pressure conditions to avoid destructive loads that might jeopardise the integrity of the structure.

Gravity Turn :

Triggered by the pitch manoeuvre, the gravity turn fundamentally consists in a smooth gradual turn in the rocket pitch angle solely aided by gravity, slowly bringing the flight path angle of the rocket towards the horizontal axis at the apogee [52]. Moreover, if, during this manoeuvrer, the thrust vector is maintained aligned to the velocity vector of the rocket, a null angle of attack can also be maintained, which is important to minimise the transverse loads acting on the structure, specially through the maximum dynamic pressure point, also known as "max-q".

After the main engine cut-off, only the drag and gravity forces remain acting on the rocket, so it enters a coasting phase while under the gravity turn until it frees itself from atmospheric influence

(if existent, the payload fairing separation takes place at this point), continuing the gravity turn until the apogee. Figure 2.24, portrays the crucial effect of the gravity in this turning manoeuvre.

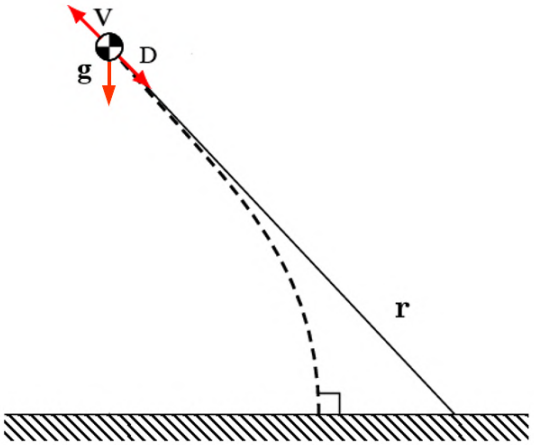

Figure 2.24: Gravity turn schematics. Adapted from [116].

Descent Flight

After reaching the apogee, the rocket starts a descent phase in which it rapidly gains speed as it loses altitude. At atmospheric re-entrance, the rocket starts heating up and slowing down subject to increasing drag forces under atmospheric flight conditions. When the rocket speed has slowed enough, a drogue parachute is deployed to drastically slow the rocket from supersonic to subsonic conditions, at which point the main parachute is deployed to further decrease the rocket velocity until a desired terminal speed is achieved [52]. Finally, the rocket enters a controlled descent until it reaches the ground, at which point retrieving action is activated.

A detailed sounding rocket flight sequence is portrayed in Fig. 2.25.

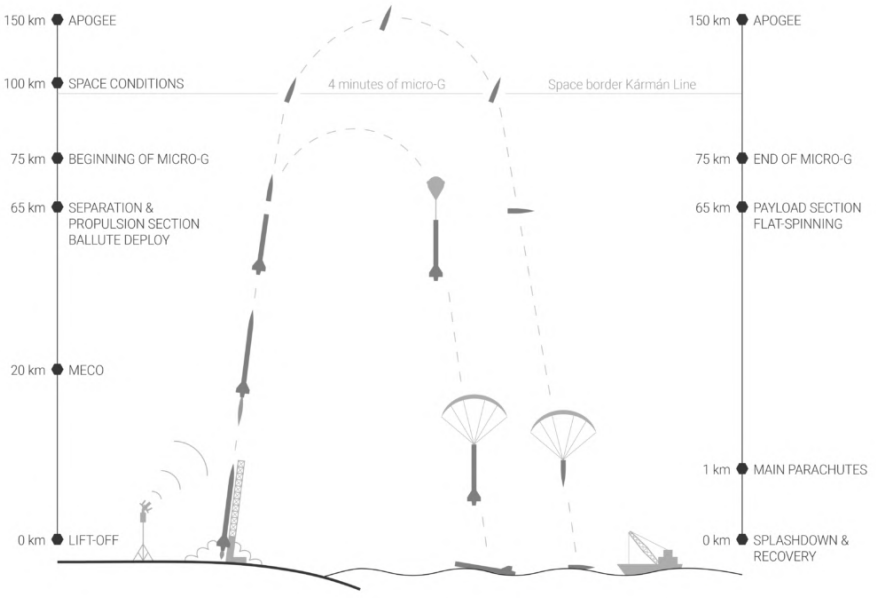

Figure 2.25: Sounding Rocket Trajectory Profile [117].

2.8.1 Trajectory Model

In order to implement this model, a high-level group was created, with 5 coupled models within, namely, Flight Dynamics, Atmospheric, Propulsion, Aerodynamics and Structural. Fig. 2.26 gives an overview of these models and their couplings.

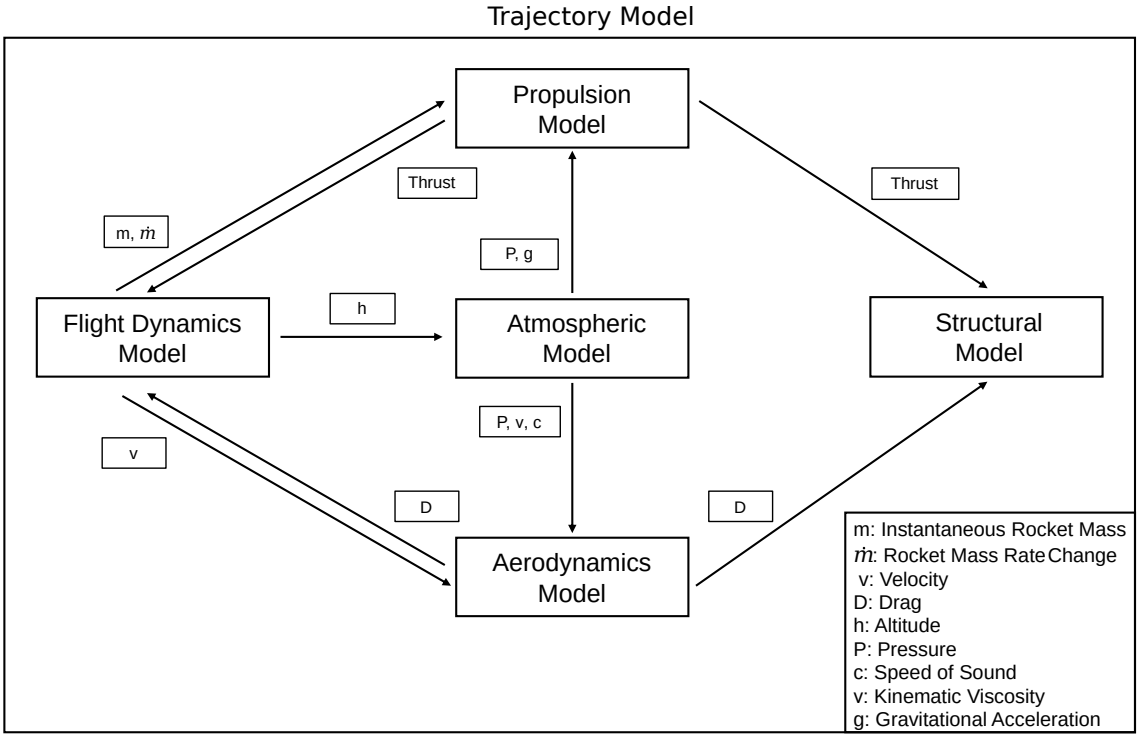

Figure 2.26: Overview of the trajectory model.

This model was then integrated in a top-level group with the mass and sizing model in order to create a framework capable of conducting an MDO process coupled with trajectory optimisation.

Chapter 3

Multidisciplinary Design Optimisation

Recent advancements in technology have improved accessibility to higher computational power at gradually lower costs. Consequently, modern computer-based engineering systems capable of conducting complex MDO processes superseded the traditional concurrent engineering philosophy-based systems, where Disciplinary Design Optimisation (DDO) was conducted.

In this chapter, a brief overview of the basic concepts of a typical MDO problem formulation is given, then a short analysis of the most commonly used MDO architectures is presented, followed by a short analysis of optimisation algorithms. Afterwards, the main trajectory optimisation methods are explained with special emphasis on direct collocation, in particular, pseudo-spectral methods.

3.1 MDO Main Concepts

The biggest advantage in using a multidisciplinary analysis is the capacity to understand the complex interactions and trade-offs between disciplines towards the global optimum result of the objective function [118]. A classic example, is the aerostructural optimisation process in aircraft wing design. In order to enhance the aerodynamic performance of a wing, the engineer adjusts a few geometric parameters which, in most cases, reduce its structural strength. Thus, the positive effects in aerodynamics achieved from the adjustment of the values of several geometric properties, called design variables in the context of MDO, need to be balanced with their negative and undesirable effects on the wing's structural properties [21, 111].

As the number of disciplines and variables integrated in the MDO process increases, such coupling among disciplines also exponentially increases, which begs for the necessity to carefully select only the most significant parameters to the objective function as design variables, treating the others as constants.

3.1.1 Design Variables

The design variables are treated as an input vector $\mathbf{x} = [x_1, x_2, x_3, ..., x_n]$ of the system, whose value evolves during the optimisation process in order to find the best design.

Typically, they can be divided into two groups: local variables, when they are specific to one discipline, or global variables, when they are shared by multiple disciplines [119].

One important characteristic of these variables is that they need to be independent, i.e., they can not be a linear combination of other design variables, otherwise, it would lead to poor performance and unpredictable system behaviour [21].

Another important aspect regards their bounds definition (lower and upper), in terms of the physical significance of the problem. For instance, design variables which represent a physical property, such as mass and length of the rocket, need to be constrained to guarantee that the optimal solution remains within a physically feasible standpoint [21].

However, it is of the utmost importance not to over-restrict the design space by setting too conservative bounds, consequently conditioning the optimiser to look for a solution outside the optimal region, or not to under-restrict the design space by setting too loose bounds, giving the optimiser a broader design space to work with at higher computational costs [120].

3.1.2 Objective Function

The objective function is the mathematical expression that translates how the design variables impact a target parameter subject to optimisation, e.g., the rocket lift-off total mass or the propellant lift-off mass.

By convention, the optimisation process typically intends to minimise the objective function, although it can equally be applied in a maximisation context with the following alternative formulation [21]

$$max[f(x)] = -min[f(x)] \ . \tag{3.1}$$

For a single-objective optimisation problem, the selection of the appropriate objective function bears a critical importance because there may be several significant metrics to minimise with complex trade-offs to balance. Alternatively, a multiple-objective formulation may be a more suitable solution for these cases. Essentially, the objective function is the linear combination of n objectives [21]:

$$\bar{f} = \sum_{i}^{n} w_i f_i(x) \tag{3.2}$$

where w_i is the weighting factor and $f_i(x)$ represents the same individual objective.

3.1.3 Constraints

Similarly to variable boundaries, constraints need to be defined in a typical MDO problem formulation to ensure physical feasibility of the design space [21]. There are two types: equality and inequality constraints, as posed as

$$g(x) = 0 \ , \tag{3.3}$$

$$h(x) < 0 \,, \tag{3.4}$$

where $g(x)$ and $h(x)$ are the constraint functions.

The difference between bounds and constraints resides in the fact that the optimisation process is being restricted or constrained, in their broadest sense. Bounds only constrict the design space, i.e., only constrict the range of values from which they can be managed. A constraint, however, allows the designer to tailor the feasibility region of the optimiser with detail. Therefore, an optimal solution will only be returned when the optimiser has successfully minimised/maximised the objective function with all constraints satisfied.

3.1.4 State and Coupling Variables

In order to enhance our understanding about the crucial balancing process of variable trade-off analysis, it is necessary to define all types of variables involved, according to the role they play in the optimisation process [21].

Besides the already defined design variables, in Section 3.1.1, there are fundamentally two other major groups: state and coupling variables. State variables, $\bar{y}$, serve the purpose of evaluating the performance of the system and are simply the outputs of the disciplines, representing the system's response to a certain set of design variable values, thus describing the state of the system at any given time. Coupling variables, y, are shared variables within the system, which serve the purpose of linking together the behaviour of each discipline. Their role is to ensure interdisciplinary feasibility and convergence. Typically, coupling variables are a subset of state variables.

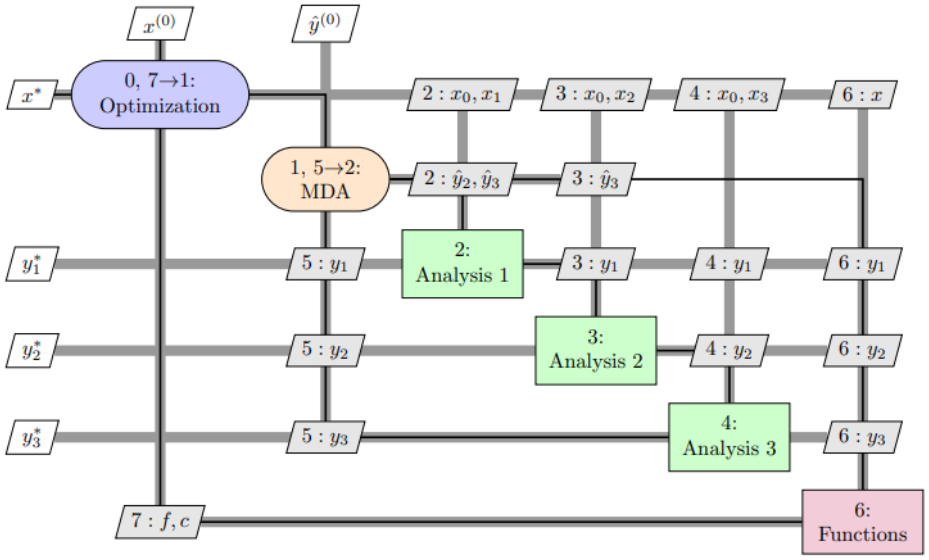

Figure 3.1: XDSM of the MDF architecture with a Gauss-Seidel MDA [118].

Without focusing too much on the details, Fig. 3.1 portrays an Extended Design Structure Matrix (XDSM) of a Multidisciplinary Design Feasible (MDF) architecture with a Gauss-Seidel multidisciplinary

analysis and serves to show a typical MDO architecture with the special emphasis on the role of each variable within the optimisation process [118]. For each individual block, upside and right side connections represent the inputs, whereas downside and left side connections represent the outputs. Looking from up to bottom and from left to right, it can clearly be observed that the optimiser has direct control over all design variables x (its outputs), which are fed to the inner multidisciplinary analysis block (its inputs). This block directly manages the coupling variables, y, which are inputs and outputs of the analysis 1, 2, and 3 blocks, representing the several disciplines of the multidisciplinary model.

3.2 MDO Architectures

The ultimate goal of any MDO problem is to find which design configuration is the optimal solution within a given design space subject to specific constraints under one or multiple optimisation objectives.

Existing literature [18, 19, 121–125] makes it clear that the choice of the right MDO architecture directly influences the computational cost and the quality of the final design. This choice involves being versed in the main advantages and disadvantages of the existing architectures, their specific applicability and scalability in the extent of each problem, and adequate implementation associated with a good choice of optimisation algorithm [118].

The main MDO architectures currently in use by the aerospace industry can be organised under several different criteria. They can be classified into two different groups: single level (or monolithic) and multi level (or distributed), according to the number of optimisers used in each architecture (single or multiple optimisers, respectively). The monolithic MDO architectures solve a single optimisation problem, while the distributed architectures decompose the original problem into a set of smaller optimisation subproblems that provide the exact same solution. Figure 3.2 portrays the most common single level and multilevel architectures.

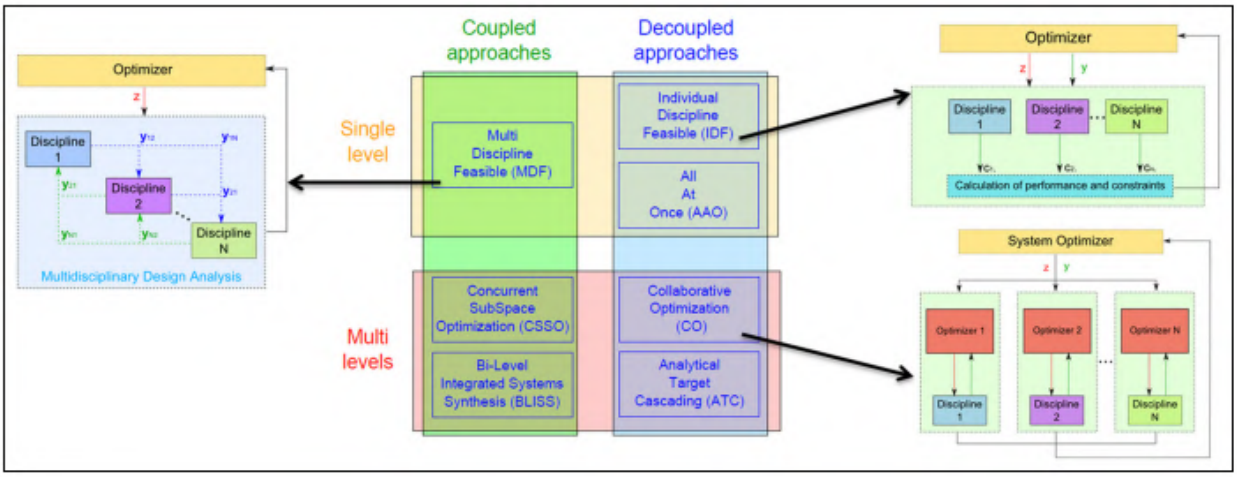

Figure 3.2: MDO architectures [18].

Single-level architectures are characterised by only using an optimiser at the top level of the multidisciplinary system, which is the governing level responsible for ensuring multidisciplinary feasibility [126].

It now follows a brief overview of the three most common single-level architectures: Multidisciplinary Feasible (MDF), Individual Discipline Feasible (IDE) and All-at-Once (AAO).

The MDF architecture, solves the optimisation problem by implementing a system-level optimiser which calls a multidisciplinary analysis (MDA) responsible for solving all governing equations at the subsystem/component level until the coupling variables converge within the specified tolerance limits [127]. In other words, multidisciplinary feasibility is guaranteed at every iteration. While this approach ensures simplicity and multidisciplinary feasibility at each iteration, it may present convergence issues, requiring under-relaxation measures and poor performances from gradient-based optimiser sensitivity analysis. Additionally, very limited advantage is taken from variable couplings leaving little to no room for parallel processing outside the MDA module, which consequently might lead to significantly higher computational costs which might pose an issue for large scale application problems [119, 124].

As an alternative approach, the IDF architecture adds additional independent variables to the problem to ensure that each discipline can be solved separately, while interdisciplinary equilibrium is maintained by a set of optimisation constraints that ensure the overall feasibility of the design once the optimisation convergence is achieved [127]. IDF potentially solves the high computational cost opened by the MDF architecture by conducting each discipline feasibility analysis independently and, in parallel, favouring speed and efficiency, at the cost of introducing additional variables and optimisation constraints, increasing the overall complexity of the original problem which might pose scalability issues for larger applications [124].

Still on the topic of MDO single-level architectures, the AAO architecture is considered the most elementary, as a system-level optimiser responsible for the optimisation of a global objective function handles the design variables z, coupling variables y, and state variables x, as well as, calls different discipline evaluators at the subsystem level which solve their local equations (residuals). These residuals are handled by the optimiser as equality constraints $R = 0$ [119]. Similarly to the IDF architecture, AAO offers parallel data processing capabilities which prove to be extremely beneficial for small scale applications. However, in comparison, a higher number of variables is handled at the optimiser level and the overall feasibility of the design is not guaranteed whenever optimisation convergence has not been achieved, as well, which makes this method not ideal for large-scale applications, such as rocket design optimisation problems [119].

In contrast to the single-level, multilevel architectures divide the original optimisation problem into a single system-level optimisation problem and several sub-system level ones, according to the number of levels. The basic idea is for the system-level optimisation problem to coordinate the smaller sub-level problems, which in turn will be solved locally. The four most common architectures of this sort are: Collaborative Optimisation (CO), Concurrent SubSpace Optimisation (CSSO), Bi-Level Integrated System Synthesis and Analytical Target Cascading (ATC).

In general, these architectures allow for better subsystem level autonomy, dividing the general optimisation problem into a set of smaller ones, which can be solved locally at the discipline level. Additionally, having various optimisation levels allows for the most advantageous optimisation algorithms to be applied at each level, without any external interference. Additionally, they can also perform parallel data

processing, which proves to be extremely beneficial in small scale applications [118].

The main drawbacks are a greater overall complexity of the system, scalability issues for some architectures and overall optimisation process inefficiencies for highly hierarchical architectures handling a high number of coupling variables [118].

After a thorough analysis, it was defined that the most suitable architecture for the developed framework was a single-level MDF architecture, as it is capable of solving the optimisation problem using a system-level optimiser that directly handles all the design variables and constraints, relaying on a MDA block to ensure multidisciplinary feasibility at each iteration, balancing simplicity in the hierarchical build of the design, efficiency of the data flows, and computational time. Most importantly, MDF guarantees feasibility at each optimisation iteration, which is found to be critical in the context of rocket design coupled with trajectory optimisation, as it means that any found solution can be physically engineered while satisfying an optimal trajectory.

In this case, the optimiser would be at the system top-level, managing all design variables fed to the mass and sizing model, allowing for a new candidate configuration to be designed., passed onto the trajectory model, within which a flight dynamics model would ensure the overall feasibility of the system by imposing the state variables at the collocation nodes along the trajectory integration process.

3.3 Optimisation Algorithms

Optimisation algorithms are numerical methods designed to systematically search for the best values for variables that optimise the objective function [128].

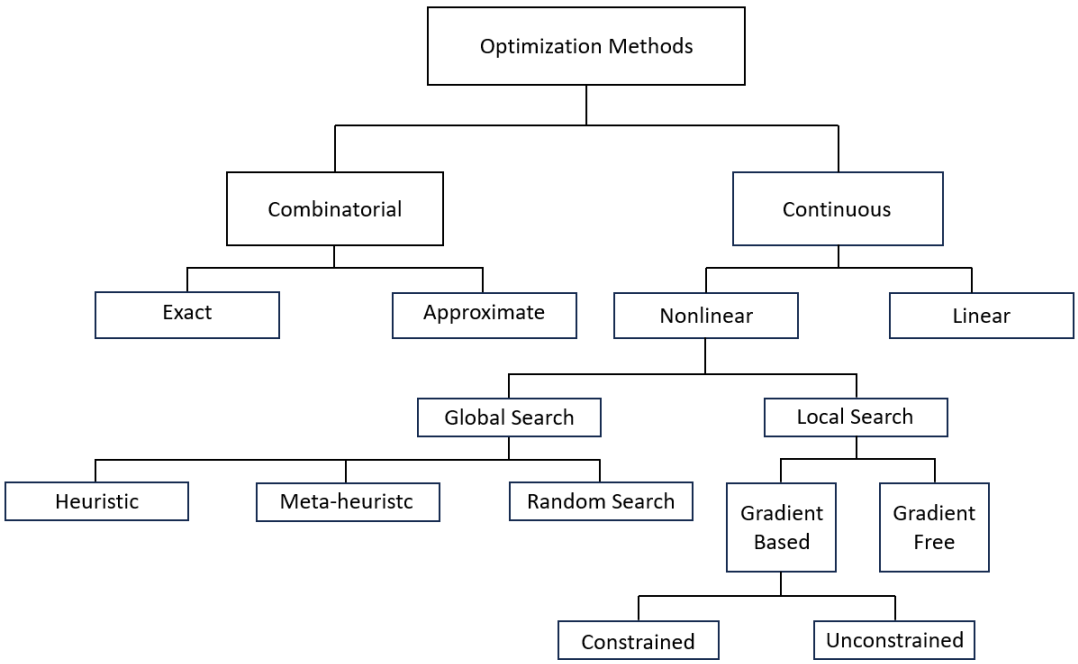

Figure 3.3: Taxonomy of optimisation algorithms. Adapted from [129].

Figure 3.3 portrays a glimpse of the wide range of optimisation algorithms, each one tailored to a specific optimisation problem. It is of unwavering importance to choose the most suitable optimisation

algorithm for each MDO problem, as this choice will directly influence the speed convergence, computational cost, and accuracy of the solution [128].

Optimisation algorithms can be divided into two major groups: combinatorial (or discrete) or continuous, depending on whether the variables are discrete or continuous quantities, respectively. Discrete optimisation algorithms are hardly suitable for rocket design applications due to the continuous nature of the majority of the design variables involved, which typically represent physical properties (continuous in their essence) [128]. Therefore, these will not be covered in the present section.

Continuous optimisation algorithms can be further divided into two groups: linear and nonlinear. Linear Programming (LP) algorithms are particularly designed for the minimisation (or maximisation) of a linear objective function subject to linear constraints. Commonly used methods are the simplex method [130, 131] and the interior-point method [132]. For further reading on this algorithms, please refer to [128]. Nonlinear Programming algorithms (NLP) are suitable for nonlinear yet smooth objective functions with at least continuous first partial derivatives on the solution target regions of the design space [128]. By nature, the objective function, inequality and equality constraints have a nonlinear behaviour in a rocket design environment with variables having a quadratic, cubic, exponential or otherwise nonlinear relationships. Consequently, NLP algorithms need to be used in this work.

Gradient-based algorithms are a particularly interesting solution in the context of MDO rocket design problems, as these are typically continuous nonlinear constrained, and so the optimiser can quickly converge into the local optima, guided by the gradients of the objective and constraint functions. It is important to note that only by defining a good enough feasible region within the design space and also by making a good initial guess for the solution, will these methods be effective, otherwise struggling with convergence or quickly converging into local optima which, do not represent the global optimal solution of the objective function of the problem [21].

Among all optimisation algorithms of this sort, the most popular include: Newton's method, Quasi-Newton Methods, particularly, the Broyden-Fletcher-Goldfarb-Shanno (BFGS), and Sequential Quadratic Programming (SQP) methods, more specifically the Sequential Least Squares Quadratic Programming (SLSQP) methods, for constrained problems.

Alternatively, Gradient-free algorithms are methods which do not require gradient information, so they might pose as an interesting option for problems where the derivatives are unknown, e.g., when the used models within the system are seen as "black-boxes" and the only known quantities are their inputs and outputs.

For problems which might pose convergence issues or for which it might be particularly challenging to set the constraints, global search algorithms can arise as a suitable solution. These algorithms generically search through the entire design space and look for the best solution, only by setting an objective function, without the need of any sort of derivative information or initial guess. Good examples of these are the Genetic algorithms [133, 134], within the Evolutionary algorithms, and the Particle Swarm Intelligence [59, 60], within the Swarm Intelligence algorithms. However, their need for a very large number of function evaluations, makes them less computationally efficient for rocket design.

Sequential Least Squares Quadratic Programming

One of the most efficient methods for constrained nonlinear optimisation problems is the Sequential Quadratic Programming (SQP), regarding function evaluations and computation cost [135]. Some of the most interesting characteristics are:

- Linear constraints and bounds remain satisfied;
- For n active constraints, SQP methods can achieve local convergence with quadratic convergence rate;
- Local convergence speed is superlinear;
- A large number of constraints can be treated by an active set strategy, and the computation of gradients for inactive restrictions can be omitted.

In essence, SLSQP is an optimisation method within the SQP wider family in which the constraints are linearised about the current point and a quadratic approximation of the objective function is defined [135].

Its formulation can be posed in standard form as

$$\min_{y \in \mathbb{R}^n} \quad f^k(y) \tag{3.5}$$

$$\text{subject to} \quad g^k(y) \leq 0, \tag{3.6}$$

where

$$f^k(y) = \frac{1}{2}(y - x_k)^T B_k (y - x_k) + \nabla f(x_k)^T (y - x_k) + f(x_k), \tag{3.7}$$

$$g_j^k(y) = \nabla g_j(x_k)^T (y - x_k) + g_j(x_k), \quad j = 1, \ldots, m. \tag{3.8}$$

Then, the Least Squares mathematical method is used to solve iteratively a set of Quadratic Programming subproblems, starting with a given vector of parameters, x^0, until a $(k+1)^{th}$ iterate, x^{k+1}, is reached in which the objective function converges within a specific tolerance condition, in compliance with all equality and inequality constraints [135].

In each iteration k, the optimiser needs to evaluate the function and constraint gradients, Δf and Δg, respectively, to determine a search direction d^k. Then, a line search is performed along that direction to find the setp length α^k that minimises the $f(x)$, and a new iteration then follows at [135]:

$$x^{k+1} := x^k + \alpha^k d^k \ , \tag{3.9}$$

where d^k is the search direction within the k^{th} step and α^k is the step length.

3.4 Trajectory Optimisation

In a rocket design process, given a specific set of mission requirements, it is necessary to find the optimal flight profile for every rocket.

Trajectory optimisation problems are a part of the larger optimal control theory branch of mathematics, which specifically seeks to find the optimal control law of a dynamic system that satisfies some set of constraints while minimising some cost function. In the present case, the controls could be the thrust or nozzle gimbal angle, e.g., with the dynamic system being the rocket itself [136]. A general mathematical problem definition can be defined as follows:

$$\text{Optimal Trajectory:} \quad \{x^*(t), u^*(t)\} \tag{3.10}$$

$$\text{System Dynamics:} \quad \dot{x} = f(t, x, u) \tag{3.11}$$

$$\text{Constraints:} \quad c_{\text{min}} < c(t, x, u) < c_{\text{max}} \tag{3.12}$$

$$\text{Boundary Conditions:} \quad b_{\text{min}} < b(t_0, x_0, t_f, x_f) < b_{\text{max}} \tag{3.13}$$

$$\text{Cost Functional:} \quad J = \phi(t_0, x_0, t_f, x_f) + \int_{t_0}^{t_f} g(t, x, u)\, dt \tag{3.14}$$

where x represents the state variables, u the control variables, $f(t, x, u)$ the system dynamics functions, c_{min}, c_{max} and $c(t, x, u)$ the lower, upper bounds, and boundary functions, respectively, b_{min}, b_{max}, $b(t_0, x_0, t_f, x_f)$ the lower, upper bounds and boundary function, respectively, and, finally, J represents the cost function.

Figure 3.4 portrays the main trajectory optimisation methods currently used.

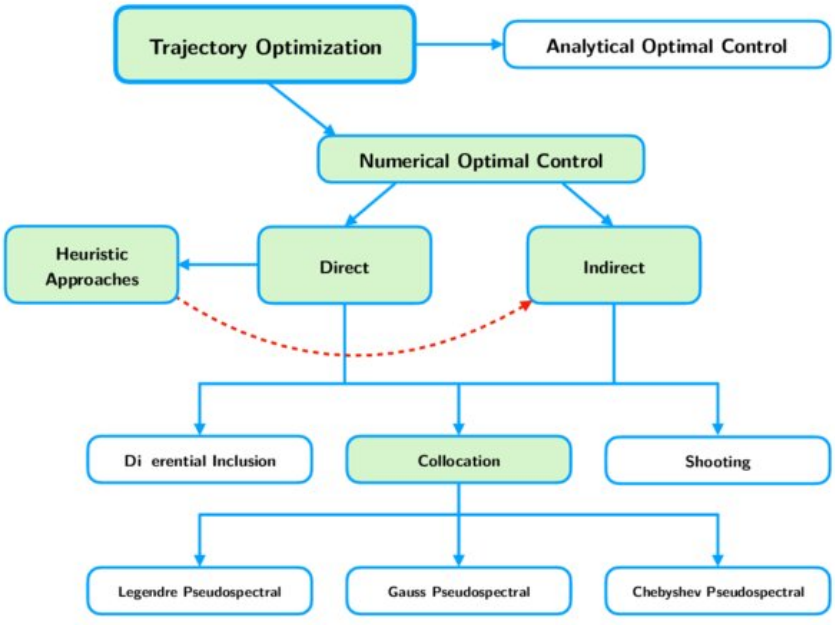

Figure 3.4: Taxonomy of the trajectory optimisation methods [137].

A trajectory optimisation problem can be first subdivided into two distinct subsets: analytical and numerical. Analytical optimal control methods are extremely efficient for closed-loop problems with simple system dynamics (linear, for example) where the analytical solution can easily be found, therefore not suitable for the current trajectory problem. Alternatively, the numerical optimal control methods are a more suitable option due to their efficiency in finding the best solution for highly non-convex problems with multiple local minima.

The latter subset can be further subdivided into three categories: heuristic, direct and indirect methods. The main advantage of the heuristic methods is that they are completely independent of any given initial information, being fully capable of conducting a global search through the design space in order to find a suitable starting point to initialise the optimisation problem. Thus, these methods are typically used coupled with other methods, namely, the indirect methods [137]. The direct and indirect numerical optimal control methods are present in a wide range of spacecraft trajectory optimisation applications. There are mainly three different types of methods: differential inclusion, collocation, and shooting, from which only the collocation subset is of interest, given that the differential inclusion method is better suited for modelling the behaviour of dynamic systems with significant uncertainties, which is not the case as the set of equations of motion is well-defined, and, similarly, the shooting method faces path constraint handling issues [137].

Direct vs Indirect Collocation

Generally speaking, collocation methods belong to a broader transcription family of methods, in which differential equations governing the rocket system dynamics are enforced in a grid of points discretised from an initial continuous time interval, called collocation nodes, ensuring that the discretised approximations at these points are faithful to the continuous dynamics [136]. This proves to be a critical property as it allows to change an otherwise complex time-continuous dynamic system optimisation problem into a much simpler Nonlinear Programming Problem (NLP). Therefore the trajectory can easily be solved with significantly reduced computational costs by interpolating and numerically solving all the state and control variables, constraints, derivatives and objective functions for the interior points of the trajectory without losing track of the physical significance of the problem [138, 139].

Collocation methods can be formulated in two different approaches: direct or indirect. Direct methods first discretise and then optimise while indirect methods optimise and then discretise [140], as illustrated in Fig. 3.5.

Starting with the indirect collocation methods, they first establish the necessary and sufficient conditions for optimality, thus forming a Hamiltonian boundary-value problem (HBVP) which is analytically derived by applying the Pontryagin's Minimum Principle (PMP). Then, the newly created differential equations governing the adjoint variables, the control equation, and the boundary conditions form a new Two Point Boundary Value Problem (TPBVP). Then, TPBVP is discretised using a collocation method, such as Hermite-Simpson, for example, transforming the continuous-time problem into a finite-dimensional nonlinear programming problem (NLP), which is numerically solved through the application of optimisation solvers, such as gradient-based methods or sequential quadratic programming (SQP), until the

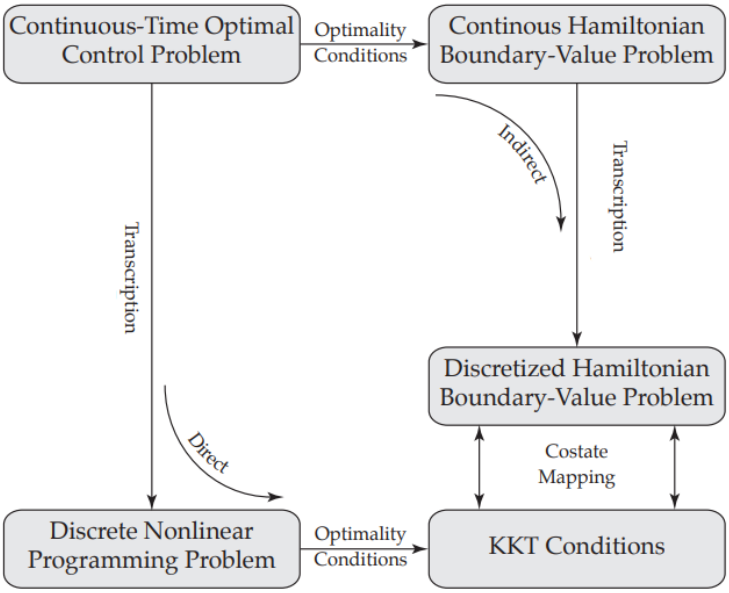

Figure 3.5: Comparison between direct and indirect collocation methods [141].

Karush-Kuhn-Tucker (KKT) optimality conditions are met [142].

In contrast, direct collocation methods are the most used in the context of trajectory optimisation due to their simplicity, robustness, and range of application [142]. These methods are characterised by first discretising a continuous time interval into a grid of collocation points. Then, the state and control variables are also discretised at the collocation points, in which dynamics are enforced. Lastly, a nonlinear program is formulated from the discretised points and solved [142].

In comparison with the latter, indirect methods are commonly more accurate, providing stronger solutions with reliable error estimates due to the necessary and sufficient conditions being derived analytically in the early stages of the problem formulation, at the cost of requiring a better initialisation as they tend to have smaller convergence regions [140].

Therefore, at the preliminary design level, for a single-stage suborbital trajectory optimisation process, the direct collocation methods are the better choice because they have proven to be simpler, computationally faster, and accurate enough, while avoiding potential convergence issues for problems with increased complexity.

Pseudospectral Collocation Methods

Pseudo-spectral methods have gained traction in the trajectory optimisation field in recent years as a powerful, highly efficient alternative for the already well-established direct collocation methods, to solve continuous nonlinear constrained optimal control problems with smooth functions, such as single-phase rocket trajectory optimisation problems. Highly complex applications of this method range from low-thrust orbit transfers, impulsive orbit transfers, ascent guidance, reentry trajectory design, and spacecraft attitude control, among others [143].

The basic idea behind a pseudospectral method is to build a high-order polynomial so that its time

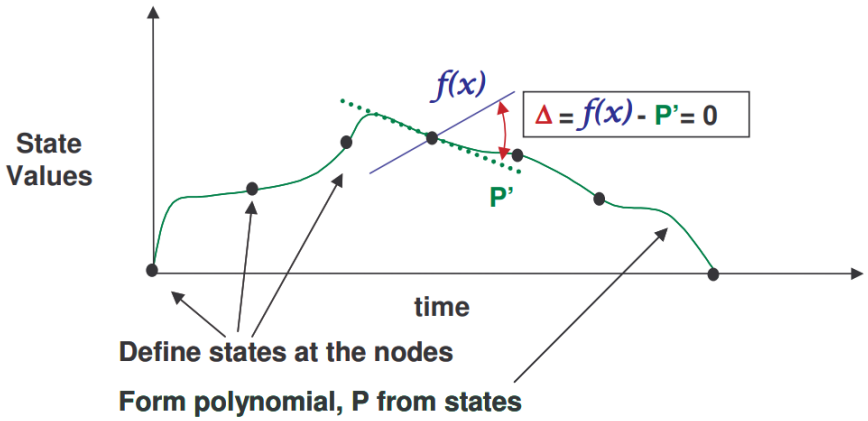

Figure 3.6: Pseudo-spectral procedure.

derivative values match the values of the system dynamics differential equations (state and control variable differential equations) at all collocation points, across the entire time interval of the trajectory. By evaluating both the polynomial time derivatives and the physical time derivatives for a well-distributed representative number of discretisation nodes, it is possible to use numerical methods (Legendre-Gauss, Legendre-Gauss-Radau, Legendre-Gauss-Lobatto or Chebyshev-Gauss-Lobatto) to minimise the existing defects until a preset maximum tolerance limit is satisfied [142].

The major difference between direct collocation methods and pseudo-spectral resides in the fact that the first typically divides the trajectory into multiple segments and independently attempts to find a low-order polynomial that suits well with the system dynamics differential equations at the collocation points, facing the necessity of setting continuity constraints between segments and additional interior nodes within segments, whereas the latter is based on building a one segment high-order polynomial whose time derivatives match the system dynamics differential equations for all the collocation nodes, which suits well only for problems with smooth flight dynamics without significant function discontinuities [142].

Given that pseudospectral collocation methods are particularly powerful and highly efficient for continuous nonlinear constrained optimal control problems when compared to other direct collocation methods, these were the methods selected for the framework to solve the trajectory optimisation problem. Particularly, the high-order Gauss-Lobatto quadrature rules, as higher order polynomials offer improved accuracy to the collocation method due to the finite precision and the number of parameters solved by the NLP problem is potentially lower in comparison to other lower order polynomials.

Chapter 4

Rocket Design Framework

4.1 MDO *Python* Lybraries

In order to implement a multidisciplinary system for the current rocket design optimisation problem, it was necessary to search for an available software framework with the following characteristics:

- Handling a system with multiple coupled disciplines integrated with trajectory optimisation;
- Support a wide range of optimisers so that a suitable option can be chosen according to specific optimisation requirements of the problem;
- Free and open-source framework with proven capabilities in handling a wide range of optimisation problems;
- Modular environment for easier model construction;
- Good metadata and data handling capabilities for less advanced non database specialised users;

After careful consideration, it was defined that the framework currently under development was to be implemented using the *OpenMDAO Python* library [144] for the multidisciplinary optimisation integrated with the *Dymos Python* library [145] for the trajectory optimisation end of the problem, thus producing a coupled approach to the preliminary rocket design.

OpenMDAO

OpenMDAO is an open-source object-oriented software framework crafted for multidisciplinary design, analysis and optimisation applications, programmed mainly in the *Python* language (for scripting convenience) and completely capable of interacting with other compiled languages, such as SWIG, Cython, C and C++, among others.

Figure 4.1 illustrates a standard modularised architecture implemented using OpenMDAO, emphacising the main hierarchical layers within every problem formulation: Component (lowest-level), Group (mid-level), and Problem (top-level) [146].

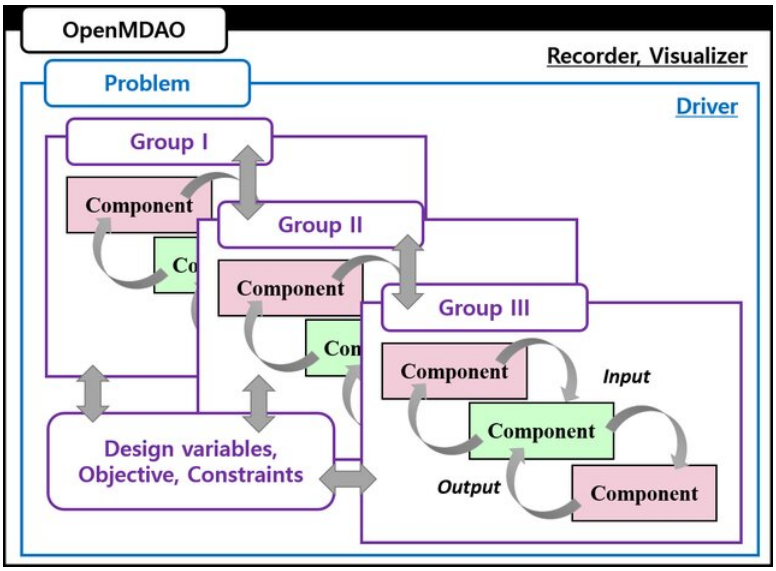

Figure 4.1: OpenMDAO standard modularized architecture [146].

Unlike other similar available options, it significantly eases the computational costs solving large-scale MDO problems by using distributed-memory parallelism and high-performance computing (HPC) resources by integrating the MPI [147] and PETSc *Python* libraries [148].

Since it was first introduced for NASA's next-generation advanced single-aisle civil transport project in 2008 at the NASA Glenn Research Center (based in Cleveland, USA) [149], it has been under continuous development with several compelling use cases across a wide range of applications: from a Cubesat MDO problem for maximised data download capabilities [150], to a low-order aerostructural wing optimisation [151], to a structural topology optimisation [152], etc.

Dymos

Dymos is an open-source software tool built on top of the OpenMDAO framework designed to solve optimal control problems, such as trajectory optimisation. The combination of a framework built from an OpenMDAO optimisation problem integrated with a Dymos trajectory optimisation opens the possibility to solve co-design optimisation problems with high computational efficiency even for complex use cases. The proposed framework will allow the implementation of a static system model within each optimisation cycle (a mass and sizing model, for example), which will receive new design variable values from the optimiser, send its outputs (for example, the length and mass of the rocket) towards a trajectory group capable of conducting all the necessary dynamic calculations through Ordinary Differential Equations (ODE) or Differential-Algebraic Equations (DAE) [145].

The advantage in using this coupled co-design system over a more traditional sequential approach is that the optimiser defined at a top-level can control the values of all the design variables, either affecting the static or the dynamic parts of the model allowing the propagation of the derivatives and potentially finding better designs with lower computational costs [145]. Fig. 4.2 portrays an XDSM diagram of a standard coupled co-design problem emphasising the existent data flows between the optimiser, the static system model, and the Ordinary Differential Equations block (in the presented framework, the

SLSQP block, the mass and sizing model, and the flight dynamics model within the trajectory model, respectively).

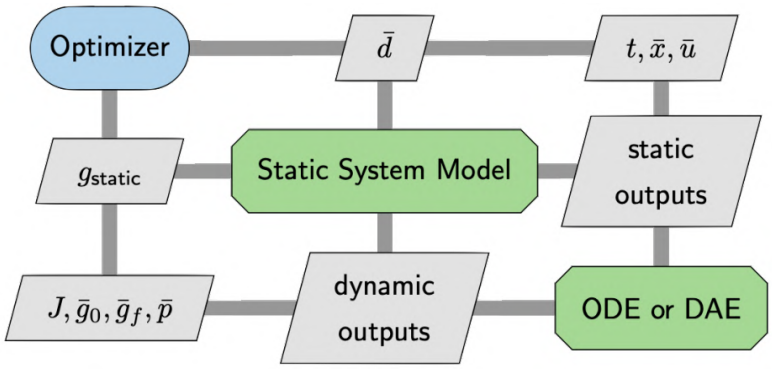

Figure 4.2: XDSM diagram of a standard coupled co-design problem, i.e., a MDO problem coupled with trajectory optimisation (OpenMDAO base framework integrated with Dymos) [145].

In the context of MDO, Dymos performs specially well for gradient-based problems dealing with differentiated time-integration schemes by creating transient models from ODEs, which, in turn, can be coupled with other models from the co-design system [145].

In terms of trajectory optimisation processes, Dymos allows for the implementation of direct transcription methods, particularly pseudospectral (high-order Gauss-Lobatto and Radau), briefly discussed in Section 3.4, in their implicit or explicit formulations [145].

4.2 MDO Framework Implementation

Previously in Chapter 2, the basic mathematical equations were arranged in a set of models, each designed to represent the behaviour of a particular discipline of the rocket analysis. In total, six models were developed: mass and sizing, flight dynamics, atmospheric, propulsion, aerodynamic, and structural. This section serves the purpose of showcasing how the framework was implemented and providing a general overview of the main data flows in the system.

In terms of the hierarchical structure of the framework, regarding the OpenMDAO standard modularised architecture previously portrayed in Figure 4.1, it was created a top-level group containing the optimiser and two major groups: the mass and sizing group, which essentially is the mass and sizing model, and the trajectory group, which essentially is the trajetory model presented in Fig. 2.26. For each set of design variables x, directly handled by the optimiser, the mass and sizing generates a new rocket configuration, from which a few main parameters are fed within the trajectory model and a new objective function evaluation value is sent back to the optimiser.

At the trajectory level, the flight dynamics model handles four state variables (downrange x, altitude h, velocity v, pitch angle γ, and also their time derivatives, respectively, $\dot{x}$, $\dot{h}$, $\dot{v}$ and $\dot{\gamma}$. The remaining $\dot{m}$, which represents the propellant instantaneous burned mass is handled by the propulsion model.

These state variables are particularly important in the trajectory integration process because they mark the state values of the trajectory, i.e., the progress of the trajectory at each point in time, particularly

at the collocation nodes, as briefly explained in Section 3.4. Additionally, they also control the time progress of the other models. For example, the altitude h, is an output of the flight dynamics, and an input of the atmospheric model. As it is integrated over time, each new value is received by the atmospheric model and consequently, the corresponding atmospheric properties, which are dependent on the altitude, are dynamically updated and received as inputs by other models, which, consequently, will be influenced by that first change in the altitude. This effect also serves to show the extremely coupled behaviour of the multidisciplinary optimisation system.

At the end of each trajectory simulation, the final altitude and the smallest difference between the critical stress of the body tube and the applied compressive stress are sent back to the optimiser, which does a constraint defect analysis and a gradient evaluation, and a new iteration begins after a linesearch process.

Figure 4.3 illustrates the XDSM diagram of the MDO framework implementation. It is possible to observe the design variables, x, coupled variables, local variables, static variables (constants) d, constraint variables, h and σ, all six developed models, as well as, the optimiser, SLSQP.

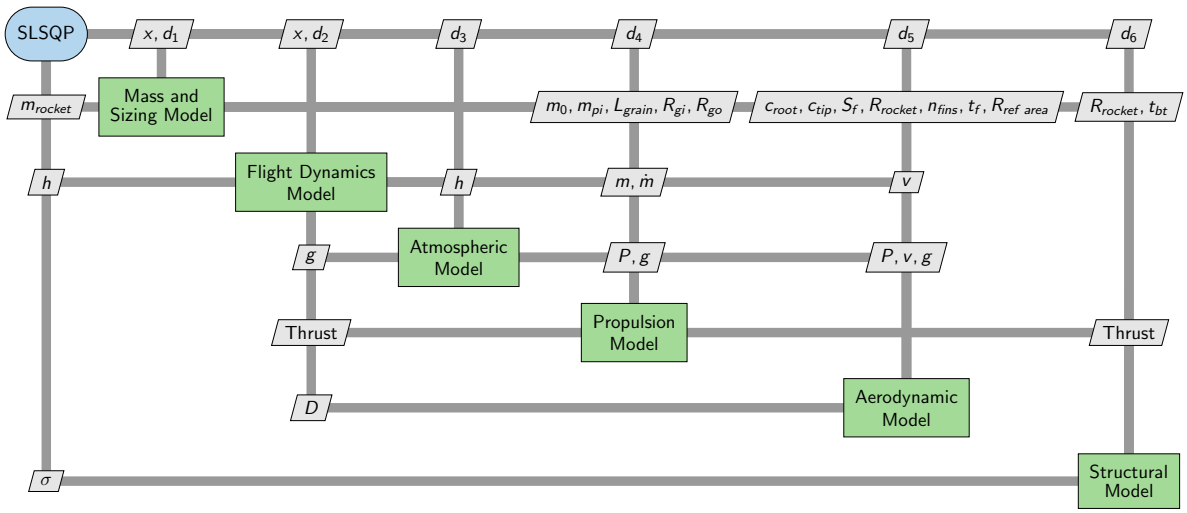

Figure 4.3: XDSM diagram of the framework highlighting the optimizer SLSQP (blue), the models (green) and design, coupled, local, and static variables (grey).

Chapter 5

Rocket Optimal Design

In this Chapter, the obtained results from a series of tests and case studies conducted with the developed framework are presented.

First, in Section 5.1, the problem formulation of the optimisation process under study is presented, then a series of parametric studies of two main optimisation parameters are conducted in Section 5.2, then in Section 5.3, a benchmark case study was conducted and the optimised rocket compared with the REXUS 2 sounding rocket [13]. In section 5.4, a follow-up multivariable case study is conducted, and finally, a series of sensitive analysis of a couple significant parameters, such as, minimum altitude and payload, were also conducted and the optimised results compared with the REXUS 10 sounding rocket, in Section 5.5.

As a reference for all the computational times presented in this Chapter, Table 5.1 lists the main computational characteristics of the used system.

Table 5.1: Computational characteristics.

Parameter	**Details**
Operating system name	Microsoft Windows 10 Home
Version	10.0.19045 Build 19045
System manufacturer	Acer Predator G3-572
System type	x64-based PC
Processor	Intel(R) Core(TM) i7-7700HQ @ 2.80GHz, 4 Cores
Installed physical memory (RAM)	16.0 GB
Storage unit	SSD 128 GB

5.1 Problem Definition

In order to get a first assessment of the capabilities of the developed MDO framework in the context of a real problem, it is important to, first, formally define it.

The chosen optimisation objective f was to minimise the rocket lift-off total mass subject to a constraint of reaching a peak altitude of at least 100 km, using the SLSQP optimisation method, briefly explained in Chapter 3.

Table 5.2 shows the initial conditions, constraints, and problem formulation of the optimisation problem:

Table 5.2: Initial conditions and problem formulation.

Conditions	Parameter	Unit	Value	Problem formulation
	v	[m/s]	0	
Initial	h	[m]	0	minimise: $f(m_{rocket})$
	x	[m]	0	With respect to design variable: D_{rocket}
	θ	[rad]	1.57	Subject to constraints: $h_f \geq 100km$
Final	$\dot{h}$	[m/s]	0	$m_{PL} \geq 44$

5.2 Parametric Study of Optimiser Parameters

As the framework was designed for a quick preliminary rocket design application, it is of the utmost importance to use the best setup configuration to obtain the most computationally cost-efficient behaviour from the optimiser. To that end, a parametric study on the impact of the optimiser tolerance as well as the step size of the finite-difference gradient approximations was conducted.

It was observed that the step size of the finite difference method, here used to approximate the derivatives, directly influenced the number of function and gradient evaluations, the number of iterations and, consequently, the computational time of the optimisation process. Therefore, in order to better assess the accuracy of the framework, several step sizes were tested: 10^{-2} and 10^{-3}. Similarly, the tolerance level of the SLSQP method was varied ranging from higher tolerances, such as 10^{-1}, 10^{-2} and 10^{-3} to smaller ones such as 10^{-4} and 10^{-5}, in order to evaluate the trade-off between the quality of the solution and the required computational time.

Tables 5.3 and 5.4 compile the obtained results of the tolerance analysis for computed step sizes of 10^{-2} and 10^{-3}, respectively.

Table 5.3: Tolerance analysis for a step size of the finite difference method of 10^{-2}.

Initial Diameter	Parameter	Tolerance				
		10^{-1}	**10^{-2}**	**10^{-3}**	**10^{-4}**	**10^{-5}**
0.3382	Rocket Diameter	0.3460	0.3589	0.3590	0.3589	0.3587
	Rocket Total Lift off Mass	472.4	511.1	511.4	511.1	510.6
	Altitude	70505.6	99803.1	101051.2	101180.4	100077.4
	Computational Time	1'10"	1'45"	2'01"	4'26"	6'44"
	Step Size	10^{-2}	10^{-2}	10^{-2}	10^{-2}	10^{-2}
	Function Evaluation	3	4	5	14	21
	Gradient Evaluation	2	3	4	7	10
	Number of Iterations	1	2	3	7	10

Table 5.3 – continued from previous page.

Initial Diameter	Parameter	Tolerance				
		10^{-1}	10^{-2}	10^{-3}	10^{-4}	10^{-5}
0.3560	Rocket Diameter	0.3568	0.3589	0.3589	0.3589	0.3589
	Rocket Total Lift off Mass	504.6	511.2	511.1	511.1	511.1
	Altitude	96485.9	100690.2	999997.8	99997.8	99997.8
	Computational Time	1'02"	1'32"	8'24"	8'24"	12'20"
	Step Size	10^{-2}	10^{-2}	10^{-2}	10^{-2}	10^{-2}
	Function Evaluation	3	4	30	30	41
	Gradient Evaluation	1	2	10	1	11
	Number of Iterations	1	2	10	1	11
0.3738	Rocket Diameter	0.3600	0.3590	0.3590	*	*
	Rocket Total Lift off Mass	514.4	511.5	511.2		
	Altitude	101863.3	100787.5	100521.5		
	Computational Time	1'30"	2'00"	2'26"	40'35"	40'05"
	Step Size	10^{-2}	10^{-2}	10^{-2}	10^{-2}	10^{-2}
	Function Evaluation	2	2	2	167	152
	Gradient Evaluation	2	2	2	Unk	Unk
	Number of Iterations	2	2	2	Unk	Unk

* Indicates that no convergence was observed within a reasonable time frame (under 100 iterations or 30 minutes of computational time).

Table 5.4: Tolerance analysis for a step size of the finite difference method of 10^{-3}.

Initial Diameter	Parameter	Tolerance				
		10^{-1}	10^{-2}	10^{-3}	10^{-4}	10^{-5}
0.3382	Rocket Diameter	0.3461	0.3589	0.3590	0.3589	0.3588
	Rocket Total Lift off Mass	472.4	511.1	511.4	511.2	510.6
	Altitude	70505.6	99803.1	101051.2	100589.9	100077.4
	Computational Time	1'40"	2'15"	7'54"	5'29"	5'29"
	Step Size	10^{-3}	10^{-3}	10^{-3}	10^{-3}	10^{-3}
	Function Evaluation	3	4	5	19	19
	Gradient Evaluation	1	3	3	8	8
	Number of Iterations	1	3	3	8	8
0.3560	Rocket Diameter	0.3597	0.3589	0.3589	0.3589	0.3589
	Rocket Total Lift off Mass	513.5	511.2	511.1	511.0	511.0
	Altitude	99809.8	100690.2	100130.0	100091.0	100091.0

Table 5.4 – continued from previous page.

Initial Diameter	Parameter	Tolerance				
		10^{-1}	**10^{-2}**	**10^{-3}**	**10^{-4}**	**10^{-5}**
0.3560	Computational Time	0'57"	1'28"	2'16"	3'32"	4'30"
	Step Size	10^{-3}	10^{-3}	10^{-3}	10^{-3}	10^{-3}
	Function Evaluation	2	2	7	12	12
	Gradient Evaluation	1	4	3	5	5
	Number of Iterations	1	2	3	5	5
0.3738	Rocket Diameter	0.3653	0.3590	0.3588	0.3587	
	Rocket Total Lift off Mass	531.2	511.4	510.6	510.6	*
	Altitude	113474.6	101725.8	99583.4	99922.02	
	Computational Time	0'55"	2'00"	2'02"	3'12"	36'53"
	Step Size	10^{-3}	10^{-3}	10^{-3}	10^{-3}	10^{-3}
	Function Evaluation	2	5	9	9	102
	Gradient Evaluation	1	4	6	6	Unk
	Number of Iterations	1	4	6	6	Unk

* Indicates that no convergence was observed within a reasonable time frame (under 100 iterations or 30 minutes of computational time).

Generally speaking, it was observed that lower tolerance levels provided more accurate results with higher computational costs, as expected.

In terms of the objective function, for larger tolerances (10^{-1}, 10^{-2}), an average relative deviation of 1.87% was observed with a similar behaviour for both step sizes, whereas, for lower tolerances (10^{-3} and 10^{-4}), this deviation comes down to approximately 0.1%.

In terms of the constraint violations, for a tolerance of 10^{-1}, the constraint violation averages approximately 13%, whereas for tolerances of 10^{-2} and smaller, this value steeply decreases to consistently under 0.5% for the most cases.

Regarding the impact of the step size in the optimisation results, it was observed that the system convergence times were well under 10 minutes for most cases, across different initial guess points and tolerance levels. In comparison with the 10^{-2} step size obtained results, it was observed that with the 10^{-3} step size, significantly less function and gradient evaluations were required in order to achieve slightly better results.

From the data presented in the previous Tables, it can be concluded that the best optimisation setting is to use a tolerance of 10^{-5} with a step size of 10^{-3}, as this is the one which provided with the lowest objective function evaluation which complied with the imposed altitude constraint.

5.3 Benchmark Case Study

Following the parametric study conducted in the previous section, a benchmark case study was conducted in order to evaluate the optimisation capabilities of the framework were 8 geometric parameters were compared with the REXUS 2 sounding rocket along with their respective relative deviations in order to evaluate any major discrepancies, as portrayed in Table 5.5. Furthermore, the key flight events and the thrust profiles were also analysed.

Table 5.5: Comparison between the REXUS 2 and the optimised rocket configuration [13, 153].

Parameter	Unit	REXUS 2	Optimised Rocket	Deviation
Length	**[m]**	5.620	5.822	+ 3.4%
Diameter	**[m]**	0.3560	0.364	+ 2.2%
Total Mass	**[kg]**	514.000	501.768	- 2.4%
Propellant Mass	**[kg]**	290.000	282.610	- 2.5%
Structural Mass	**[kg]**	126.000	121.158	- 3.8%
SRM Length	**[m]**	2.800	2.895	+ 3.4%
Fin Root Chord	**[m]**	0.590	0.582	- 1.4%
Fin Tip Chord	**[m]**	0.400	0.408	+ 2.0%

As it can be found in Table 5.5, all compared parameters align well with the REXUS 2, with the biggest relative deviation observed being a 3.8% reduction in the structural mass.

In terms of the key events analysis, Table 5.6 portrays a comparison between the key flight events of both rockets. It can be observed that there is a major discrepancy between both rockets SRM burn-out times, which can be justified by observing the difference between the thrust profiles of both rockets, portrayed in Fig. 5.1. The REXUS 2 has a dual-thrust profile, with a boost phase of 4 seconds at 84.5 kN and a sustain phase of roughly 21 seconds at 13.3 kN [153], whereas, the optimised model has a regressive thrust profile starting at 36.2 kN gradually decreasing to a final 15.5 kN, and thus, this difference might have been due to the much higher burning rates in the boost phase of the REXUS 2.

Table 5.6: Key flight events [13, 153].

Number	Time [s]		Altitude [km]		Event
	REXUS 2	Optimised Rocket	REXUS 2	Optimised Rocket	
1	T+ 0.0	T+ 0.0	0.00	0.00	Lift-Off
2	T+ 26.0	T+ 31.09	22.72	20.11	SRM Burn-Out
3	T+ 153.0	T+ 163.8	100.24	100.08	Apogee
4	T+ 300.0	T+ 302.06	3.30	3.30	Recovery Sequence Activation

As for the flight profile analysis, it was found that there is a general agreement between both REXUS 2 and the optimised rocket, as seen in Figure 5.2. The differences observed were due to the fact that the REXUS 2 flight profile was only a prediction in preparation for the actual mission, so atmospheric, aerodynamic and other factors may not have been taken into account. The evidence for this assumption lays

with the fact that the REXUS 2 flight path is almost a perfect parabola, which is not possible under real atmospheric conditions. The presence of aerodynamic air resistance combined with the changes with altitude of the atmospheric parameters, namely, atmospheric density and pressure, would cause a more irregular profile shape, slowing substantially the rocket during the propelled ascent and atmospheric re-entrance phases.

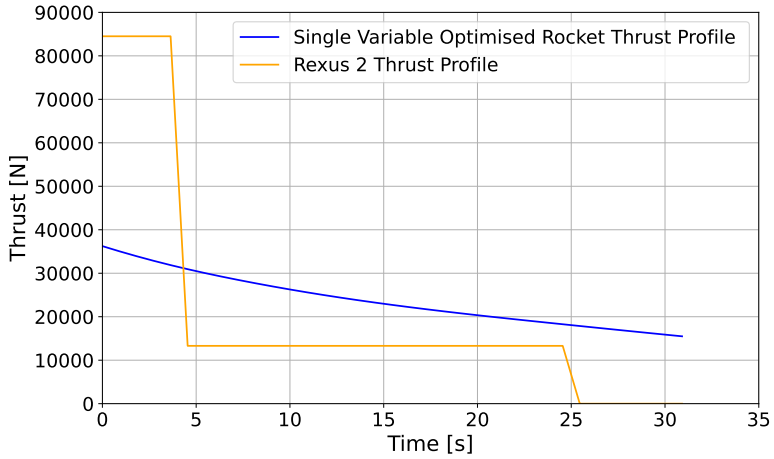

Figure 5.1: Thrust profile comparison of the Rexus 2 and the optimised rocket.

Additionally, it was observed that after the recovery sequence activation, i.e., after the parachute deployment, the predicted flight profile of the REXUS 2 follows an excessively steep descent, which further supports this assumption. In order to completely clarify this issue, a comparison between both REXUS 2 flight profile with the optimised rocket flight profiles with and without parachute deployment was conducted, which can also be seen in Figure 5.2. Interestingly enough, this comparison allowed to appreciate the impact of the recovery system in the final stages of the flight profile. A controlled slow descent is expected in order to safely land a rocket with terminal velocities up to 8 m/s [85, 86], which is not possible in such a small amount of time as the REXUS 2 flight profile suggests.

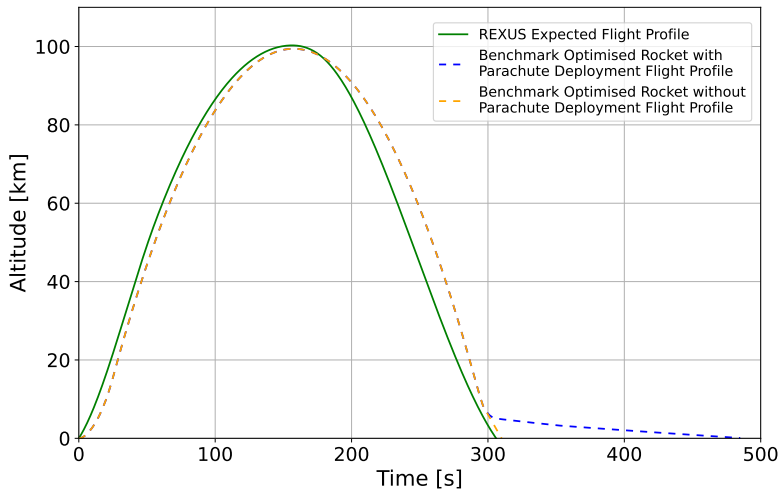

Figure 5.2: Comparison between the Rexus 2 expected flight profile, retrieved from [13], with the optimised rocket flight profile paths with and without parachute deployment.

Finally, a visual comparison of both rockets is illustrated in Fig. 5.3, with a side-by-side 2D schematic view of both configurations highlighting some main dimensions.

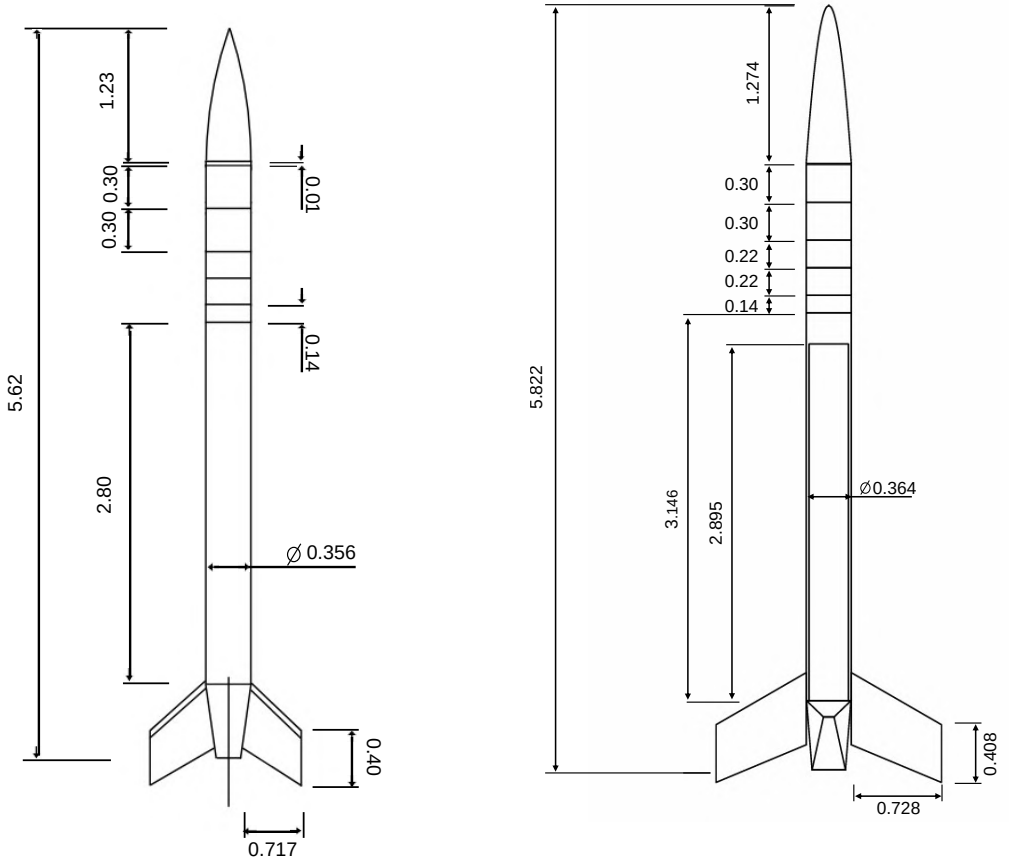

(a) REXUS configuration.

(b) Optimised rocket configuration.

Figure 5.3: 2D schematic comparison between the REXUS and the optimised rocket configuration.

5.4 Multivariable Case Study

In the previous section, a benchmark case study was conducted for an optimisation procedure with only one design variable. To further test the capabilities of the framework, a multivariable follow-up test was prepared using 10 geometric design variables. Table 5.7 portrays the selected design variables, their initial values, lower and upper bounds and the final optimised value.

After analysing the previous table, it is interesting to note that several variables which have reduced impact in the objective function, the lift-off rocket mass, were only slightly changed, while other variables with much more impact were drawn to their lower or upper bounds in order to minimise the objective function. This behaviour is relevant because it might indicate that there might be a malfunction within the system. Although it is true that, in order to minimise the objective function, the optimiser will rightfully try to reduce the thicknesses of the components as much as possible, the imposed structural constraint should restrain the optimiser from searching for new values beyond the feasible region of the design space, even if their bounds allow it. Table 5.8 presents a comparison between the characteristics of the REXUS 2 and the optimised rocket.

Table 5.7: Design Variable initial value, lower and upper bounds and optimised value.

Design Variable	Unit	Initial Value	Lower Bound	Upper Bound	Optimised Value
Rocket Diameter	**[m]**	0.356	0.3500	0.3650	0.3500
Body Tube Thickness	**[m]**	0.003	0.0028	0.0032	0.0028
SRM Grain Thickness	**[m]**	0.067	0.062	0.070	0.062
SRM Casing Thickness	**[m]**	0.0025	0.002	0.003	0.002
Nozzle Throat Area	**[m^2]**	0.005	0.003	0.008	0.00350
Nozzle Angle	**[rad]**	0.2618	0.2618	0.5236	0.2618
Rocket Length to Diameter Ratio	**-**	16.0000	16.0000	17.5000	16.0000
Nose Cone Length to Diameter Ratio	**[m]**	4.0000	3.8000	4.2000	4.1990
Expansion Ratio	**-**	10.0000	9.0000	10.0000	9.9999
Nozzle Convergent Section Angle	**[rad]**	0.4500	0.4500	0.5500	0.5236

Table 5.8: Comparison between the REXUS 2 and the multivariable optimised rocket configuration [13, 153].

Parameter	Unit	REXUS 2	Optimised Rocket	Deviation
Length	**[m]**	5.620	5.600	-0.4%
Diameter	**[m]**	0.356	0.350	-1.7%
Total Mass	**[kg]**	514.000	439.530	-14.5%
Propellant Mass	**[kg]**	290.000	247.842	-14.5%
Structural Mass	**[kg]**	126.000	105.545	-16.2%
SRM Length	**[m]**	2.800	2.560	-8.6%
Fin Root Chord	**[m]**	0.59	0.56	-5.1%
Fin Tip Chord	**[m]**	0.400	0.392	-2 %

From this table, it is possible to observe that a reduction of 14.5 % in rocket total mass and propellant mass was achieved, along with a 16.2% reduction in the structural mass, which is a significant improvement from the benchmark case study. This was an expected result as the optimiser manages ten design variables against only one in the former case study. Also, these results align well with the observed behaviour of the optimiser regarding the thickness reduction of the components.

As for the flight profile analysis, it was observed that the optimised rocket in the current case study followed a similar profile to the other two, yet the burnout time significantly lowered, as a consequence of the total mass reduction, which demanded much less propellant to be burned, as Fig. 5.4 portrays.

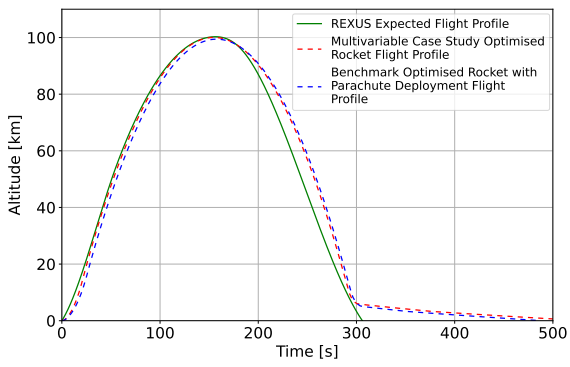

(a) Flight profile comparison between the Rexus 2 and the single and multivariable optimised rockets.

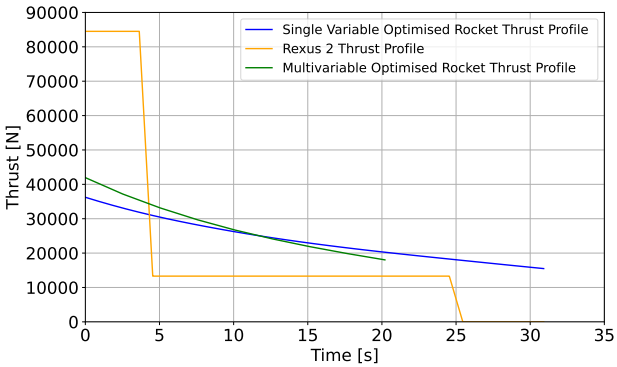

(b) Thrust profile comparison between the Rexus 2 and the single and multivariable optimised rockets.

Figure 5.4: Comparison between the optimised rocket configuration and REXUS.

This leads to the conclusion that, from this optimisation process, a new configuration was found which is capable of meeting the intended mission requirements (to reach a minimum peak altitude of 100 km) with 14.5% less propellant.

Finally, a visual comparison of both rockets is illustrated in Fig. 5.5, with a side-by-side 2D schematic view of both configurations highlighting some main dimensions.

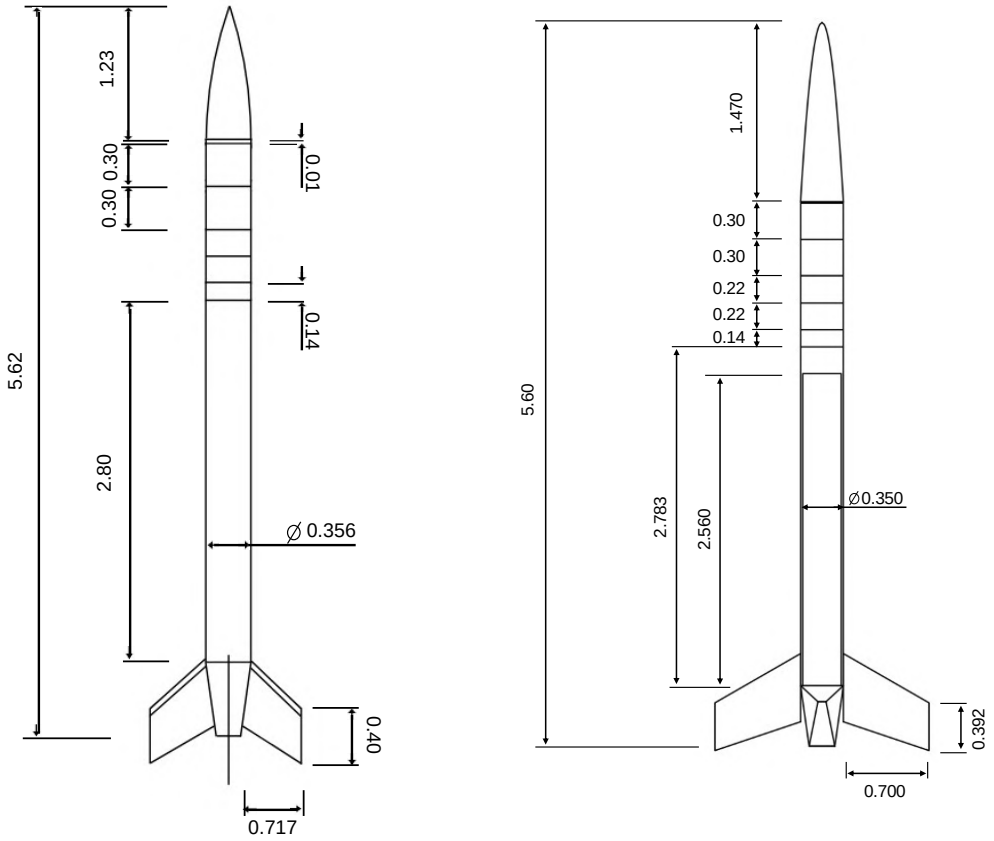

(a) REXUS configuration.

(b) Optimised rocket configuration.

Figure 5.5: 2D schematic comparison between the REXUS and the multivariable case study optimised rocket configuration.

5.5 Payload and Minimum Altitude Sensitivity Analysis

In previous case studies, the optimisation capabilities of the developed framework were put to test, first for a single design variable optimisation problem and, afterwards, for a more demanding multivariable optimisation problem with ten geometric design variables. After this initial testing, a sensitivity analysis of two significant optimisation parameters was conducted: minimum altitude and the payload.

5.5.1 Payload Sensitivity Analysis

In order to assess the payload sensitivity, the payload was set to 112.3 kg, matching with the REXUS 10 [153] and the same optimisation setup was used with adjusted variable upper bounds in order to give the optimiser enough design space to find a feasible solution. Table 5.9 presents a comparison between the optimised rocket configuration with the REXUS 2.

From this comparison, it was possible to observe the impact of the payload in the rocket designed configuration. The new rocket reached an altitude of 100.15 km with a total lift-off mass of 484.6 kg, which represents a 5.7% decrease when compared to the REXUS 2 rocket and a 10.2% increase when compared to the previous multivariable optimised rocket. Moreover, it was possible to observe a general increase in the other compared parameters which aligns well with the expected behaviour of the framework given that more payload was carried.

Table 5.9: Comparison between the REXUS 2 and the payload sensitivity analysis new optimised rocket configuration [13, 153].

Parameter	Unit	REXUS 2	Optimised Rocket	Deviation
Length	**[m]**	5.620	5.792	+3.1%
Diameter	**[m]**	0.356	0.362	+1.7%
Total Mass	**[kg]**	514.000	484.551	-5.7%
Propellant Mass	**[kg]**	290.000	265.176	-8.6%
Structural Mass	**[kg]**	126.000	111.786	-11.3%
SRM Length	**[m]**	2.800	2.628	-6.1%
Fin Root Chord	**[m]**	0.59	0.58	-1.8%
Fin Tip Chord	**[m]**	0.400	0.405	+1.4 %

5.5.2 Minimum Altitude Sensitivity Analysis

Continuing this sensitivity analysis, the impact of the minimum altitude was also tested by changing the original altitude constraint from 100 km to 82.45 km, the altitude reached by REXUS 10 [153], while maintaining the original payload of 98 kg. The same optimisation setup was used, with adjusted variable lower bounds in order to give the optimiser enough design space to find a feasible solution, obtaining the results presented in Table 5.10.

Table 5.10: Comparison between the REXUS 2 and the altitude sensitivity analysis new optimised rocket configuration [13, 153].

Parameter	Unit	REXUS 2	Optimised Rocket	Deviation
Length	**[m]**	5.620	5.568	-0.9%
Diameter	**[m]**	0.356	0.348	-2.2%
Total Mass	**[kg]**	514.000	426.550	-17.0%
Propellant Mass	**[kg]**	290.000	237.286	-18.2%
Structural Mass	**[kg]**	126.000	102.842	-18.38%
SRM Length	**[m]**	2.800	2.469	-11.8%
Fin Root Chord	**[m]**	0.59	0.56	-6.0%
Fin Tip Chord	**[m]**	0.400	0.390	-2.6 %

These results clearly showed the impact of the minimum altitude in this new optimised rocket. Reaching a peak altitude of 82.89 km with a total lift-off mass of 426.6 kg, which represents a 17.0% decrease when compared to the REXUS 2 rocket and a - 2.95% when compared with the multivariable optimised rocket, with a completely different mission profile as Fig 5.6 portrays. In contrast to the payload sensitivity

analysis results, it was possible to observe a general decrease in the compared geometric parameters which aligns well with the expected behaviour of the framework given that a lower altitude constraint was imposed.

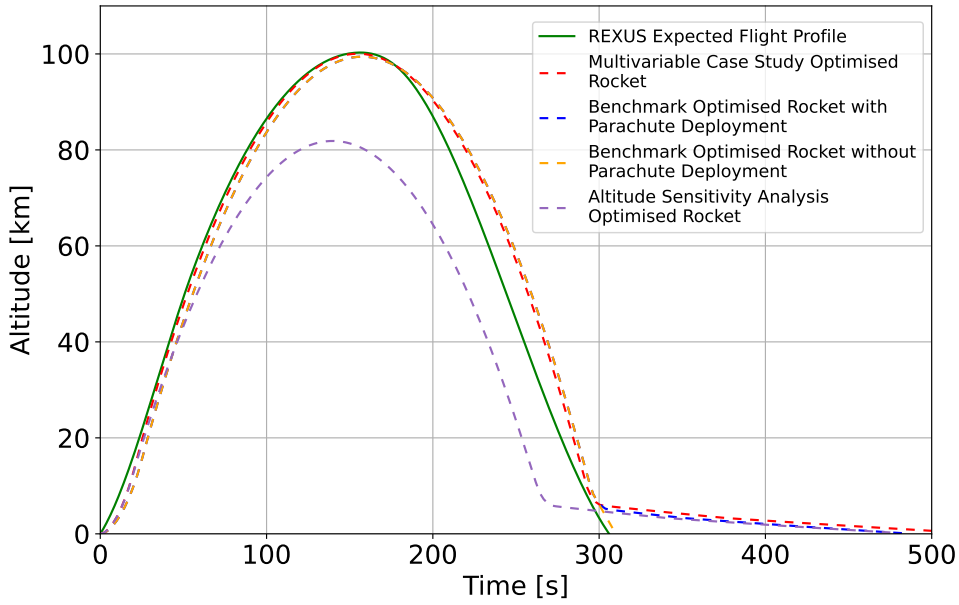

Figure 5.6: Comparison between the Rexus 2 expected flight profile, retrieved from [13], with the optimised rocket flight profile paths of the benchmark with and without parachute deployment, multivariable case study with parachute deployment and altitude sensitivity analysis.

5.5.3 Rexus 10 Case Study: Payload and Minimum Altitude Sensitivity Analysis

As a final test, the impact of the coupled effect of the payload and minimum altitude in the optimisation results was tested using the REXUS 10 flight mission data for comparison. The payload was set to 112.3 kg and the altitude constraint to 82.45 km. Table 5.11 presents the obtained results in comparison to the REXUS 10.

Table 5.11: Comparison between the REXUS 10 and the optimised rocket configuration [153].

Parameter	Unit	REXUS 10	Optimised Rocket	Deviation
Length	**[m]**	5.620	5.568	-0.9%
Diameter	**[m]**	0.356	0.348	-2.2%
Total Mass	**[kg]**	528.300	449.718	-14.9%
Propellant Mass	**[kg]**	290.000	238.653	-17.7%
Structural Mass	**[kg]**	126.000	102.850	-18.4%
SRM Length	**[m]**	2.800	2.483	-11.4%
Fin Root Chord	**[m]**	0.590	0.557	-5.6%
Fin Tip Chord	**[m]**	0.400	0.390	-2.56 %

From these results, it can be observed that the optimised rocket had a total lift-off mass of 449.7 kg for a peak altitude of which is an intermediary value between the two previous sensitivity analysis obtained values. This can be explained by the combined effect of the payload and minimum altitude acting simultaneously. As it was confirmed earlier in this Chapter, an increase in the carried payload

results in heavier designs, whereas, an altitude constraint reduction leads to lighter designs. Thus, the expected value for the objective function, the total mass lift-off mass of the rocket, was a number which balanced these two contrasting effects.

Table 5.12: Design Variable initial value, lower and upper bounds and optimised value.

Design Variable	Unit	Initial Value	Lower Bound	Upper Bound	Optimised Value
Rocket Diameter	**[m]**	0.35	0.3480	0.3650	0.348
Body Tube Thickness	**[m]**	0.003	0.0028	0.0032	0.0028
SRM Grain Thickness	**[m]**	0.068	0.062	0.07	0.062
SRM Casing Thickness	**[m]**	0.002	0.002	0.003	0.002
Nozzle Throat Area	**[m^2]**	0.005	0.003	0.008	0.003202
Nozzle Angle	**[rad]**	0.3	0.2618	0.5236	0.2618
Rocket Length to Diameter Ratio	**-**	16.5	16	18	16.0
Nose Cone Length to Diameter Ratio	**[m]**	4	3.8	4.4	4.399
Expansion Ratio	**-**	10	9	10	10
Nozzle Convergent Section Angle	**[rad]**	0.45	0.45	0.55	0.5236

In terms of optimisation, results were compared with the REXUS 10. It was observed a rocket lift-off total mass optimisation of 14.9%, 17.7% in propellant mass and 18.4% in structural mass. In addition, other evaluated parameters were observed to be in accordance with the REXUS 10. Although these results are positive, they need to be considered with great caution because it was observed that the optimiser dragged every thickness to its lower bound in order to minimise the objective functions portrayed in Table 5.12, which further strengthens earlier signs that the structural model might not be properly evaluating the compressive stresses at the body tube.

In terms of the key flight events, these are presented in Table 5.13.

Table 5.13: Key flight events [153].

Number	Time [s]		Altitude [km]		Event
	REXUS 10	Optimised Rocket	REXUS 10	Optimised Rocket	
1	T+ 0.0	T+ 0.0	0.00	0.00	Lift-Off
2	T+ 26.0	T+ 19.39	20.38	12.3246	SRM Burn-Out
3	T+ 140.00	T+ 126	82.45	82.60	Apogee
4	T+ 380.0	T+ 341.82	3.30	3.30	Recovery Sequence Activation

It is possible to note some discrepancies which need to be addressed: first, the SRM burn-out time happens earlier in the flight due to the fact that the optimised rocket carried 17.7% less propellant mass; second, the optimised rocket reached the apogee 14 seconds earlier in the flight, in comparison to the REXUS 10, which might be related either to a generally higher total velocity profile or to an underestimation of the drag profile. This argument also serves to justify the discrepancy in the recovery sequence activation times of both rockets.

To further understand this mismatch in the key flight events, a few available parameters from the flight data of the REXUS 10 mission [153] and the framework were compared, as presented in Fig. 5.7.

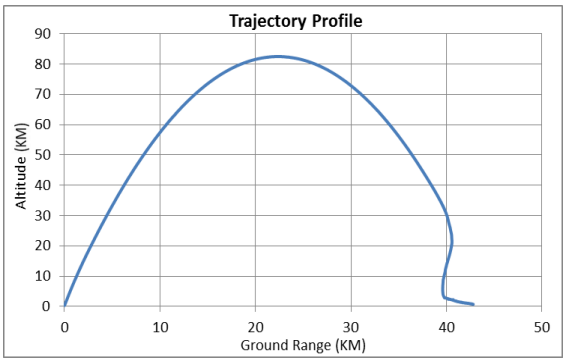

(a) REXUS 10 flight profile [153].

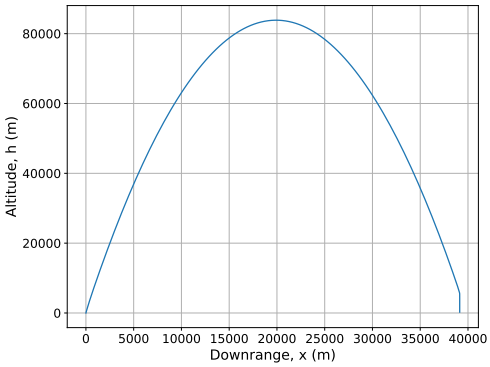

(b) Optimised rocket flight profile.

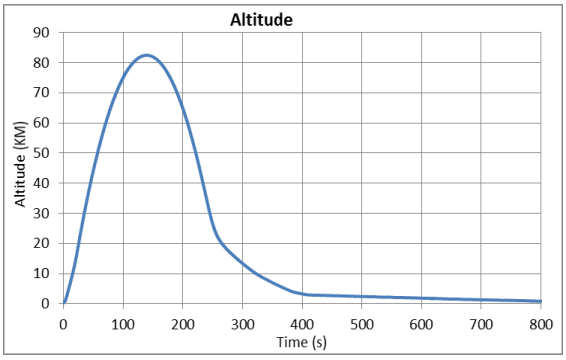

(c) REXUS 10 altitude profile [153].

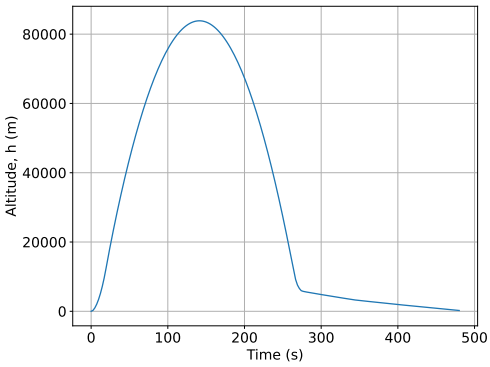

(d) Optimised rocket altitude profile.

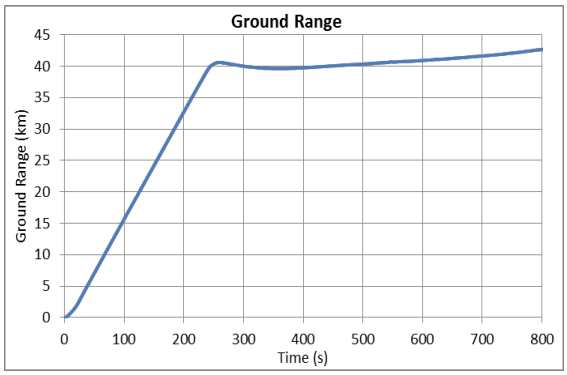

(e) REXUS 10 ground range profile [153].

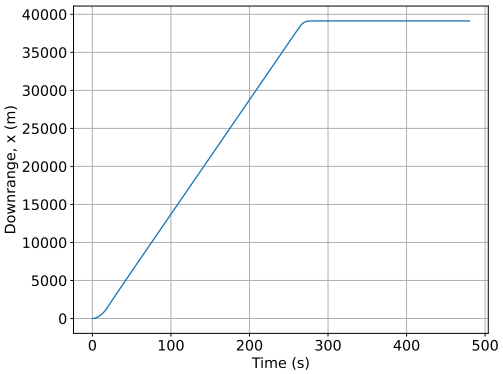

(f) Optimised rocket downrange profile.

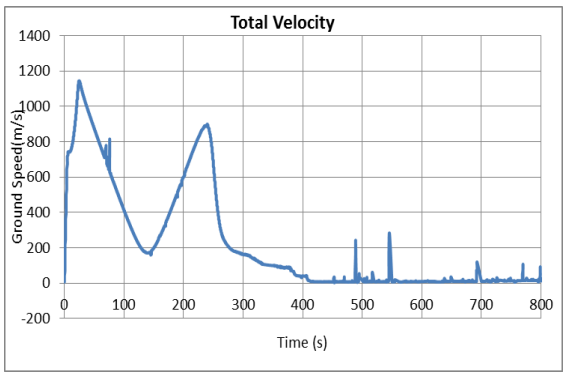

(g) REXUS 10 total velocity profile [153].

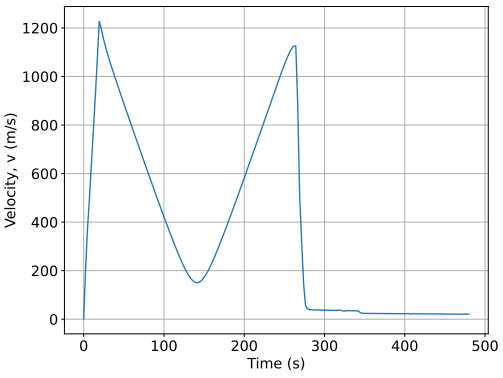

(h) Optimised rocket total velocity profile.

Figure 5.7: Comparison of several flight parameters of the REXUS 10 mission and the optimised rocket.

After comparing both flight data, the following conclusions were reached:

- As portrayed in Figures 5.7a and 5.7b, the trajectory profile of the optimised rocket was too parabolic when compared to the real flight data of the REXUS 10 mission, which suggests that there might be possible issues in the behaviour of the aerodynamics model;
- The hypothesis that higher speeds could be causing a discrepancy in the key flight events was confirmed, as it can be seen in figures 5.7g and 5.7h.
- Compared to the optimised rocket, the REXUS 10 took an additional 300 seconds to reach the ground which suggests that the terminal velocity after parachute deployment was higher than expected. After review, it was found that the reached terminal velocity was 20.74 m/s, which is excessive and confirms the earlier assumptions.

Finally, a visual comparison of both rockets is illustrated in Fig. 5.8, with a side-by-side 2D schematic view of both configurations highlighting some main dimensions.

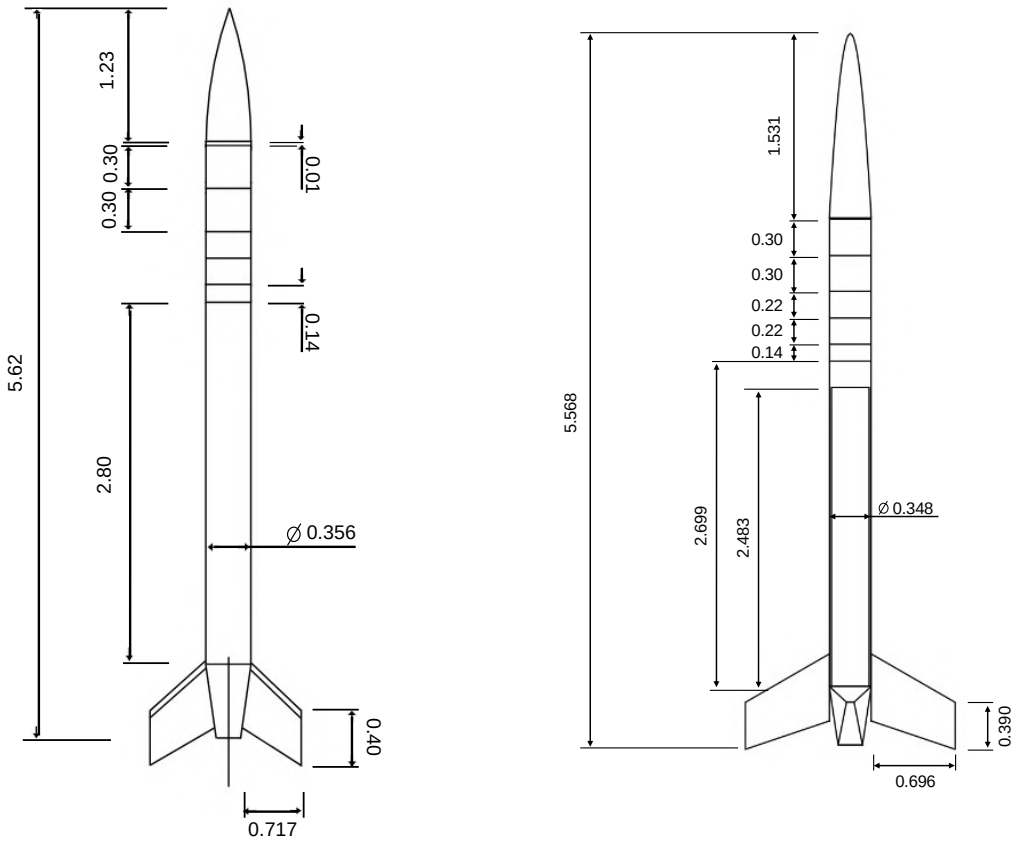

(a) REXUS configuration.

(b) Optimised rocket configuration.

Figure 5.8: 2D schematic comparison between the REXUS and the REXUS 10 case study optimised rocket configuration.

Chapter 6

MDO with High Fidelity Structural Analysis

In Section 5.3, an optimised rocket was compared with the REXUS 2 sounding rocket and a 3.8% structural mass reduction was achieved. In order to truly appreciate how further this mass can be reduced, a completely new optimisation process was created where the developed MDO framework was integrated with a high fidelity structural analysis model, developed by Fernandes [70].

6.1 Optimisation Process Description

The optimisation process was composed of the following steps:

- As the objective was to evaluate to what extent the structural mass of the optimised rocket of the benchmark case study could be minimised, its diameter was fixed in order to start the process;
- This diameter was used as a design variable in the MDO framework to create an initial rocket configuration, so that an initial trajectory simulation could be conducted to determine a first estimate of the suborbital flight Δ_v.
- This initial value of the Δ_v was sent to the mass and sizing model so that a new rocket configuration could be modelled. At the mass and sizing model, the convergence between the structural factor σ and the structural mass m_s was guaranteed through an internal iterative process involving four equations and four variables, namely: the propellant mass, m_p, the structural mass, m_s, Δ_v and σ;
- After convergence was achieved, a candidate rocket configuration was sent to the MDO framework, a new trajectory simulation was conducted and a new Δ_v was obtained, adjusted to the new configuration;
- This adjustment in the Δ_v, posed a problem because it did not match the previous Δ_v which originated the current candidate configuration. For this reason, a new convergence had to occur, this time in order to converge the Δ_v with the candidate rocket configuration.

- Next, a series of simulations, including both flow and Finite Element Method (FEM) were run in *SOLIDWORKS* so that real stresses imposed on each component could be calculated;
- Finally, the difference between the allowed maximum stresses and the real stresses was calculated for each component. If this difference was positive, it meant that the component could withstand more demanding loading conditions and, thus, the thickness would be reduced. If a negative difference was observed, the opposite happened;
- This process only ended when, between two consecutive iterations, significant thickness changes were not observed in any component;

Figure A.1 portrays a detailed flowchart of the optimisation process, in which, it is possible to see the existing dataflows between the MDO framework and the high fidelity structural system, as well as the internal convergence cycles.

6.2 Results

In this section, the obtained results from an optimisation process conducted using the previous procedure are presented. The results will be presented sequentially, following the interior convergence cycles within the global iterative loop.

Starting with the Δ_v and σ convergence, Table 6.1 portrays the evolution of the rocket initial mass m_0, final mass m_f, structural mass m_s, and initial propellant mass m_{p0}. For each parameter, the initial and final masses along with their relative deviations are presented.

Table 6.1: Initial and final values of m_0, m_f, m_s, and m_{p0} for the σ, and m_s convergence process over four iterations.

Iteration	m_0			m_f			m_s			m_{p0}		
	Initial	Final	Dev. %	Initial	Final	Dev. %	Initial	Final	Dev. %	Initial	Final	Dev. %
1	352.08	346.65	1.56	161.69	156.25	3.48	112.69	107.25	5.07	190.4	190.4	0.0
2	346.65	339.66	2.06	156.25	153.48	1.81	107.25	104.48	2.65	190.4	186.18	2.2661
3	340.7725	333.39	2.21	154.60	147.98	4.47	105.59	98.98	6.68	186.18	185.41	0.4153
4	339.66	322.53	5.31	153.48	142.80	7.48	104.48	93.80	11.3859	186.18	179.73	3.9357

It can be seen that a general trend of mass reduction was achieved which is consistent with the thickness reduction observed at each component presented further in the present section.

Regarding the Δ_v, it was observed an unexpected upward trend during the iterative process, which might be associated with the fact that the kick angle was not optimised during the procedure and, as a consequence of the successive weight adjustments made, the trajectories started to place the rocket at the apogee with slightly higher horizontal speeds than expected, which might be the reason for this unexpected behaviour.

Figure 6.1 graphically portrays the Δ_v evolution throughout the iterative process.

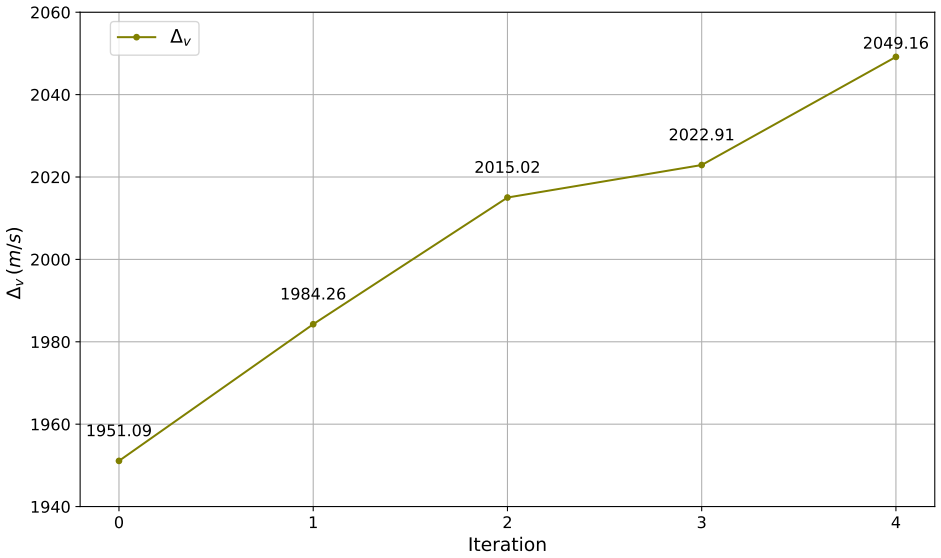

Figure 6.1: Δ_v evolution along the iterative process.

In terms of the thickness evolution, Figure 6.2 illustrates the evolution of the thicknesses of several main components throughout the optimisation process.

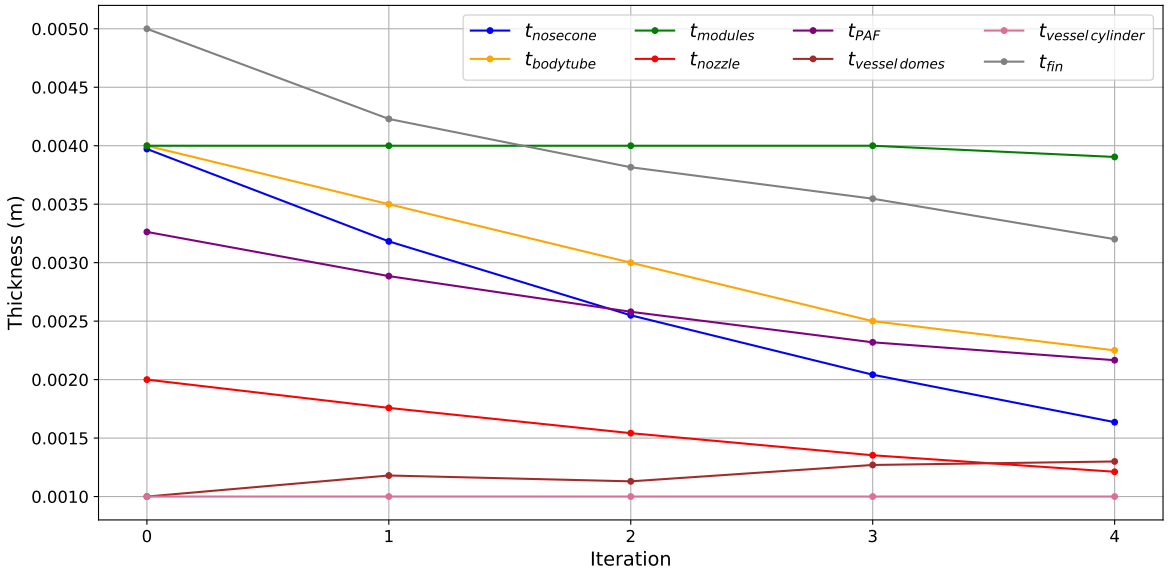

Figure 6.2: Thickness evolution along the iterative process.

From this figure, it can be seen that the thickness of the majority of the components decreased along the iterative process, as expected, with two exceptions: the thickness of the vessel domes, which are the top and bottom extremities of the rocket SRM casing, slightly increased; and the thickness of the vessel cylinder, which is the thickness of the SRM casing.

Regarding these results, the observed decrease in the thicknesses of the majority of the components can be justified by the fact that the guessed initial values were too conservative, so, as the initial stresses at each component were too far from their specific allowed maximum stresses, it was expected a general trend of thickness reduction along the iterative process.

Addressing now the two exceptions observed, their initial values were the lowest of the set, and so it is possible that they were implausible initial guesses, which further strengthens the confidence in the obtained results, as the structural analysis was capable of analysing these components and determine that in order to comply with their maximum stress allowed, it was not possible to further decrease their thickness, which, on the contrary, had to be maintained or increased, even though, the optimisation objective favoured against it.

Additionally, it was observed that the rocket total mass diminished 29.56 kg, which represents a 8.4% reduction. As for the propellant mass, it diminished 10.67 kg representing a 5.6% downsizing. Furthermore, the structural mass was reduced in 18.89 kg, which represents a reduction of 16.8%.

Figure 6.3 graphically showcases the evolution of these masses along the iterative process: rocket structural mass, $m_{structural}$, propellant initial mass, $m_{initial\,propellant}$, rocket initial mass, m_0, and rocket final mass, m_f.

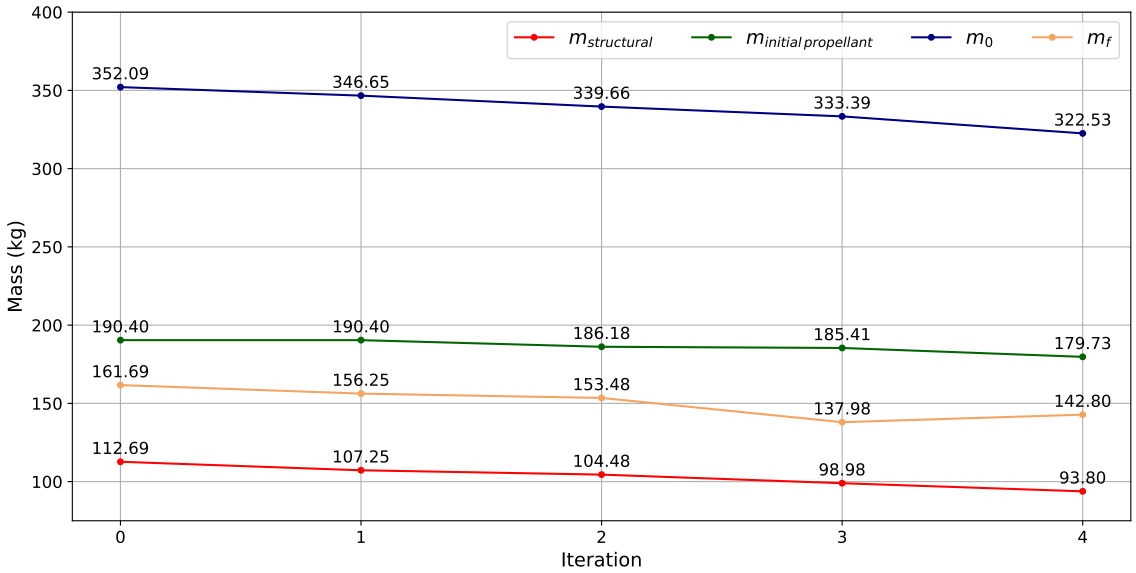

Figure 6.3: Mass evolution along the iterative process.

Chapter 7

Conclusions

7.1 Concluding Remarks

The main goal of this dissertation was to develop and validate an MDO framework coupled with trajectory optimisation capable of optimising the preliminary design of a sounding rocket with a minimum payload capacity of 44 kg and 100 km reachable peak altitude.

Six models were then developed: mass and sizing, flight dynamics, atmospheric, propulsion, aerodynamics, and structural.

A mass and sizing model containing seven components (nose cone, modules, fins, nozzle, body tube, SRM, and a component for the estimation of general parameters) was developed, followed by an aerodynamics model capable of estimating the C_d profile of the rocket based on three sources: nose cone, base and fins, with a compressible flow correction for better accuracy under compressible flow regimes and a recovery system contribution to simulate the behaviour of the deployment of a parachute during the descent phase of the flight profile.

Afterwards, a propulsion model was developed, divided in two components: the grain burnback and the internal ballistics, each intended to simulate the grain regression and the internal ballistic behaviour of the SRM using one-dimensional isentropic flow equations, respectively.

Next, a structural model was developed in order to perform a simplified buckling analysis of the body tube cylindrical shell, and also, a fin flutter analysis to ensure the integrity of the fins throughout the rocket trajectory.

An atmospheric model following both the 1962 and the 1976 U.S Standard Atmosphere Conventions for the prediction of the atmospheric properties for a given altitude was adapted from the *OpenAeroStruct Python* library and integrated in the framework.

Then, a 2 DoF flight dynamics model was developed in order to calculate four state variables for the trajectory model: the rate of change of the velocity, $\dot{v}$, pitch angle, $\dot{\gamma}$, altitude $\dot{h}$ and downrange $\dot{x}$.

After their individual development, the couplings among variables were identified and a trajectory model was assembled using five of these modules: flight dynamics, atmospheric, propulsion, aerodynamic and structural.

After extensive research, it was then decided to develop a framework following a MDF architecture, using a SLSQP as the global optimiser and a pseudospectral method for the direct collocation of the integration process of the trajectory.

It then followed the selection of an available open-source software capable of conducting multidisciplinary optimisation coupled with trajectory optimisation upon which was decided to implement this framework using the *OpenMDAO* and *Dymos Python* libraries.

Having the framework fully implemented, a series of parametric studies were conducted focused on two main optimisation parameters: the tolerance level of the SLSQP method and the step size of the finite difference method for three different initial points of the design space. This studies indicated that the framework is capable of conducting optimisation processes consistently under 10 minutes, subject to tolerance levels as low as 10^{-5} with a step size of 10^{-2} and 10^{-3}. After analysis, the best optimisation setup was achieved using a tolerance level of 10^{-5} for the SLSQP optimiser and a finite difference method step size of 10^{-3}.

A benchmark case study was conducted in order to assess the framework behaviour under a real optimisation environment. Using a single design variable, the rocket diameter D_{rocket}, a good agreement between the optimised and the benchmark rocket, the REXUS 2 was observed with an absolute average relative deviation of 2.64% and a 2.4% rocket total mass reduction. As for the trajectory analysis, an overall agreement was observed with some discrepancies found in the burn-out time due to the difference in the thrust profile of both rockets.

A multivariable case study then followed, with a significant improvement in the optimisation behaviour of the framework. The rocket total lift-off and the propellant masses were reduced 14.5%, as well as the structural mass, which was reduced 16.2%.

A sensitivity analysis was conducted for two main parameters: payload and altitude. It was confirmed that a positive change in the carried payload significantly increases the masses of the rocket, with a 10.2% increase in the rocket lift-off total mass. As for the altitude sensitivity analysis, it was observed that reducing the altitude constraint from 100 km to 82.45 km, in order to match the REXUS 10 mission, resulted in a 3% total mass reduction, which was the expected behaviour.

A final case study was then conducted in order to evaluate the coupled effect of both parameters by increasing the payload value from 90 kg to 112.3 kg and lowering the altitude constraint from 100 km to 82.45 km, matching the REXUS 10 mission requirements. The optimised results were then compared with the REXUS 10 rocket and a general mass reduction was observed: 14.9% in the rocket lift-off total mass, 17.7% in the propellant mass and 18.4% in the structural mass. Additionally, the flight data of both the REXUS 10 mission and the optimisation trajectory simulation were compared, it was concluded that higher speeds were achieved in the simulated trajectory and that the followed flight path was too parabolic which suggests that the aerodynamics model might require further improvements.

Finally, in order to find the optimal structural mass of the optimised rocket, the MDO framework was integrated with a High Fidelty Structural Model in a new optimisation process. Using an iterative procedure, it was possible to couple the trajectory simulation with flow and FEM structural analysis run in SOLIDWORKS in order to minimise the structural mass of the rocket, given a fixed diameter of the body

tube. From the obtained results, it was possible to observe a thickness reduction trend in the majority of the analysed components with a reduction of 16.8% in structural mass, as expected. Nonetheless, these results need to be taken with caution given the fact that only four iterations were conducted due to computational time limitations, which was not enough to reach a final convergence.

Overall, the developed framework shows good signs of being capable of performing the design optimisation of a single-stage sounding rocket at a preliminary level. Yet, further testing is needed to truly appreciate its capabilities.

7.2 Future Work

Although the developed framework shows encouraging signs, there is room for further improvements across several areas.

At the model level, the flight dynamics model could be improved from the current 2 DoF to a much more interesting 6 DoF system dynamics; also, the aerodynamics could be further improved if other sources of drag were to be included in the model, thus giving a more robust drag evaluation. The structural model could also be improved if a more precise structural analysis was to be conducted and not limited to buckling and fin flutter.

Additionally, a cost model could be implemented in order to bring a more realistic approach to the preliminary design process.

Bibliography

[1] G. Genta. Private space exploration: A new way for starting a spacefaring society? *Acta Astronautica*, 104(2):480–486, nov 2014. ISSN 0094-5765. DOI:10.1016/j.actaastro.2014.04.008.

[2] S. Laundy and H. Dooley. How space exploration is fueling the Fourth Industrial Revolution, 2023. URL https://www.brookings.edu/articles/how-space-exploration-is-fueling-the-fourth-industrial-revolution/. Accessed on December 1st, 2023.

[3] U. S. S. Foundation. *The Space Report: The Authoritative Guide to Global Space Activity*. Space Foundation, 2013.

[4] S. F. E. Team. Space Foundation Releases the space report 2023 Q2, showing annual growth of global space economy to $546B, 2023. URL https://www.spacefoundation.org/2023/07/25/the-space-report-2023-q2/. Accessed on December 1st, 2023.

[5] R. Brukardt. How will the space economy change the world?, 2022. URL https://www.mckinsey.com/industries/aerospace-and-defense/our-insights/how-will-the-space-economy-change-the-world. Accessed on December 1st, 2023.

[6] NASA. As Artemis Moves Forward, NASA Picks SpaceX to Land Next Americans on Moon - NASA. https://www.nasa.gov/news-release/as-artemis-moves-forward-nasa-picks-spacex-to-land-next-americans-on-moon/, 2021. [Accessed 07-01-2024].

[7] K. Chang. SpaceX Wins NASA $2.9 Billion Contract to Build Moon Lander. https://www.nytimes.com/2021/04/16/science/spacex-moon-nasa.html, 2021. [Accessed 07-01-2024].

[8] G. Gurney. *Space Technology Spinoffs*. An Impact book. Watts, 1979. ISBN 9780531022900.

[9] I. A. Crawford. The long-term scientific benefits of a space economy. *Space Policy*, 37:58–61, Aug. 2016. ISSN 0265-9646. DOI:10.1016/j.spacepol.2016.07.003.

[10] I. S. E. C. Group. *Benefits Stemming from Space Exploration*. DIANE Publishing Company, 2013. ISBN 9781457849091.

[11] N. Administration. *Earth Benefits from NASA Research and Technology. Life Sciences Applications*. CreateSpace Independent Publishing Platform, 1991. ISBN 9781722187354.

[12] A. Papageorgiou and J. Olvander. The role of multidisciplinary design optimisation (MDO) in the development process of complex engineering products. In *Proceedings of the 21st International Conference on Engineering Design (ICED17)*, volume 4, 2017.

[13] M. Persson, O. & Hörschgen. REXUS 2 - the first EuroLaunch project. In *17th ESA Symposium on European Rocket and Balloon Programmes and Related Research*, pages 389 – 393, Sandefjord, Norway, 30 May - 2 June 2005. Swedish Space Corporation (SSC) & Deutsches Zentrum für Luft- und Raumfahrt (DLR), ESA Publications Division. ISBN 92-9092-901-4.

[14] T. S. Taylor. *Introduction to Rocket Science and Engineering, Second Edition*. CRC Press, apr 2017.

[15] W. Humphries. *Information Flow in the Launch Vehicle Design/Analysis Process*. 1999. Available:https://ntrs.nasa.gov/api/citations/20000012425/downloads/20000012425.pdf.

[16] N. Duranté, A. Dufour, V. Pain, G. Baudrillard, and M. Schoenauer. Multidisciplinary Analysis and Optimisation Approach for the Design of Expendable Launchers. 08 2004. ISBN 978-1-62410-019-2. doi: 10.2514/6.2004-4441. DOI:10.2514/6.2004-4441.

[17] R. S. Ryan and J. S. Townsend. Fundamentals and Issues in Launch Vehicle Design. *Journal of Spacecraft and Rockets*, 34(2):192–198, 1997. DOI:10.2514/2.3209.

[18] L. Brevault, M. Balesdent, and S. Defoort. Preliminary study on launch vehicle design: Applications of multidisciplinary design optimisation methodologies. *Concurrent Engineering*, 26(1): 93–103, Nov. 2017. ISSN 1531-2003. DOI:10.1177/1063293x17737131.

[19] N. F. Brown and J. R. Olds. Evaluation of Multidisciplinary optimisation Techniques Applied to a Reusable Launch Vehicle. *Journal of Spacecraft and Rockets*, 43(6):1289–1300, Nov. 2006. ISSN 1533-6794. doi: 10.2514/1.16577. DOI:10.2514/1.16577.

[20] L. Brevault, M. Balesdent, N. Bérend, and R. Le Riche. Decoupled Multidisciplinary Design optimisation Formulation for Interdisciplinary Coupling Satisfaction Under Uncertainty. *AIAA Journal*, 54(1):186–205, Jan. 2016. ISSN 1533-385X. doi: 10.2514/1.j054121. DOI:10.2514/1.j054121.

[21] J. R. R. A. Martins and A. Ning. *Engineering Design optimisation*. Cambridge University Press, Nov. 2021. ISBN 9781108833417. DOI:10.1017/9781108980647.

[22] T. E. Konstantin. Exploration of Space by means of Reactive Aparatus. 5, 1903.

[23] Robert H. Goddard, World Rocket Pioneer. 1960.

[24] H. Oberth. *The Rocket into Planetary Space*. DE GRUYTER, Dec. 2014. ISBN 9783486754636. doi: 10.1515/9783110367560.

[25] R. Goddard. *A Method of Reaching Extreme Altitude*. Smithsonian Institution, 1919.

[26] A. Chodos. This Month in Physics History: March 16, 1926: Launch of the First Liquid Fuel Rocket. https://www.aps.org/publications/apsnews/200103/history.cfm, mar 2021. [Accessed 09-01-2024].

[27] NASA. Dr. Robert H. Goddard, American Rocketry Pioneer. https://www.nasa.gov/dr-robert-h-goddard-american-rocketry-pioneer/#:~:text=In%201914%2C%20Goddard%20received%20two,by%20various%20types%20of%20gunpowder. [Accessed 15-01-2024].

[28] V. Glushko. *Development of Rocketry and Space Technology in the USSR.* Novosti Press Publishing House, 1973.

[29] F. Ordway and R. Wakeford. *International Missile and Spacecraft Guide*. International Missile and Spacecraft Guide. McGraw-Hill, 1960.

[30] G. A. Robertson and D. W. Webb. The Death of Rocket Science in the 21st Century. *Physics Procedia*, 20:319–330, 2011. ISSN 1875-3892. DOI:10.1016/j.phpro.2011.08.029.

[31] H. S. SEIFERT. Twenty-Five Years of Rocket Development. *Journal of Jet Propulsion*, 25(11): 594–603, Nov. 1955. ISSN 1936-9980. DOI:10.2514/8.6832.

[32] W. R. Dornberger. The German V-2. *Technology and Culture*, 4(4):393, 1963. ISSN 0040-165X. doi: 10.2307/3101376. DOI:10.2307/3101376.

[33] J. R. Verbeek. *"V2 - Vengeance" from The Hague and Surroundings. The Deployment of the V2-Missiles and the Terrors for the City and its Inhabitants*. 2003.

[34] W. C. B. Hunt. Lost in Space: The Defeat of the V-2 and Post-War British Exploitation of German Long-Range Rocket Technology. *Air and Space Power Review*, 22(2), 2019. ISSN 1463-6298. URL https://www.raf.mod.uk/what-we-do/centre-for-air-and-space-power-studies/aspr/aspr-vol22-iss2-8-pdf/. Available:https://www.raf.mod.uk/what-we-do/centre-for-air-and-space-power-studies/aspr/aspr-vol22-iss2-8-pdf/.

[35] M. J. Neufeld. The guided missile and the third reich: Peenemünde and the forging of a technological revolution. *Science, Technology and National Socialism*, 1994.

[36] D. Hölsken. *V-Missiles of the Third Reich, the V-1 and V-2*. Monogram Aviation Pub., 1994. ISBN 9780914144427.

[37] W. Corliss. *NASA Sounding Rockets, 1958-1968: A Historical Summary*. NASA SP. Scientific and Technical Information Office, National Aeronautics and Space Administration, 1971.

[38] R. Ceresuela. Aerodynamic problems of sounding-rocket vehicles. *Journal of Spacecraft and Rockets*, 5(1):96–100, Jan. 1968. ISSN 1533-6794. DOI:10.2514/3.29191.

[39] D. W. JOHNSON. Development of recovery systems for high- altitude sounding rockets. *Journal of Spacecraft and Rockets*, 6(4):489–491, Apr. 1969. ISSN 1533-6794. DOI:10.2514/3.29688.

[40] D. W. Johnson. Sounding Rocket Payload Recovery Systems. *Journal of Spacecraft and Rockets*, 11(6):424–425, June 1974. ISSN 1533-6794. DOI:10.2514/3.62091.

[41] D. D. Dunfee and G. K. OSS. A frangible sounding rocket vehicle design. *Journal of Spacecraft and Rockets*, 4(6):823–826, June 1967. ISSN 1533-6794. DOI:10.2514/3.28970.

[42] R. J. Muraca. External and internal air loads on sounding rockets. *Journal of Spacecraft and Rockets*, 4(9):1207–1210, Sept. 1967. ISSN 1533-6794. doi: 10.2514/3.29053. DOI:10.2514/3.29053.

[43] L. D. Wing. Practical Methods for Predicting Aerodynamic Heating Effects on Sounding Rockets. *Journal of Spacecraft and Rockets*, 8(11):1114–1119, Nov. 1971. ISSN 1533-6794. DOI:10.2514/3.59777.

[44] R. D. SHAVER. The two-stage sounding rocket problem. *Journal of Spacecraft and Rockets*, 4(10):1310–1315, Oct. 1967. ISSN 1533-6794. DOI:10.2514/3.29077.

[45] V. P. Marchese, E. L. Rakowsky, and L. J. BEMENT. A Fluidic Sounding Rocket Motor Ignition System. *Journal of Spacecraft and Rockets*, 10(11):731–734, Nov. 1973. ISSN 1533-6794. DOI:10.2514/3.61955.

[46] H. S. TSIEN and R. C. EVANS. Optimum Thrust Programming for a Sounding Rocket. *Journal of the American Rocket Society*, 21(5):99–107, Sept. 1951. ISSN 1936-9964. DOI:10.2514/8.4372.

[47] S. MEYERS. Aeroelastic analysis of sounding rocket vehicles. In *3rd Sounding Rocket Technology Conference*. American Institute of Aeronautics and Astronautics, Mar. 1973. DOI:10.2514/6.1973-284.

[48] D. Mori. Application of Fiber Reinforced Plastics to the Sounding Rocket. *Journal of the Society of Mechanical Engineers*, 69(572):1179–1184, 1966. ISSN 2424-2675. DOI:10.1299/jsmemag.69.572_1179.

[49] T. Noga and R. Puri. Microgravity, atmosphere sounding, astronomy, technology validation - an overview of suborbital rockets' missions and payloads. *International Journal of Space Science and Engineering*, 6(2):179, 2020. ISSN 2048-8467. DOI:10.1504/ijspacese.2020.110365.

[50] U. S. F. A. A. O. of Commercial Space Transportation. *Suborbital Reusable Launch Vehicles and Emerging Markets*. Federal Aviation Administration, Office of Commercial Space Transportation, 2005.

[51] G. Sutton and O. Biblarz. *Rocket Propulsion Elements, Ninth Edition*. John Wiley & Sons (US), 2017. ISBN 9781118753651.

[52] D. Edberg, D. Edberg, and G. Costa. *Design of Rockets and Space Launch Vehicles, Second Edition*. AIAA education series. American Institute of Aeronautics and Astronautics, Incorporated, 2022. ISBN 9781624106415. DOI:10.2514/5.9781624106422.0000.0000.

[53] Spieler, Patrick and Lupu, Elena and Hasic, Dalmir and Spieler, Michael and Pellet, Michael and Arif, Hassan Baumann, Cyril and Talon, Quentin Lozano, Emilio and Kirchhoff, Oliver and Jung, Laurent and Teste, Stephane and Cardinaux, Christian and Ivanov, Anton and Floreano, Dario and Mintchev, Stefano. Technology demonstrator of a rocket carrying a deployable fleet of autonomous gliders . In *67th International Astronautical Congress, Adelaide, Australia*, Sept. 2017.

[54] G. Seibert and B. T. Battrick. *The History of Sounding Rockets and Their Contribution to European Space Research*. ESA Publications division Noordwijk, 2006. ISBN 92-9092-550-7. Available:https://www.esa.int/esapub/hsr/HSR_38.pdf.

[55] S. Christe, B. Zeiger, R. Pfaff, and M. Garcia. Introduction to the Special Issue on Sounding Rockets and Instrumentation. *Journal of Astronomical Instrumentation*, 05(01):1602001, 2016. doi: 10.1142/S2251171716020013. DOI:10.1142/s2251171716020013.

[56] M. Lappa. *Fluids, Materials and Microgravity: Numerical Techniques and Insights Into Physics*. Elsevier Science, 2004. ISBN 9780080445083.

[57] D. Bayley and R. Hartfield. Design optimisation of Space Launch Vehicles for Minimum Cost Using a Genetic Algorithm. volume 8, 07 2007. ISBN 978-1-62410-011-6. DOI:10.2514/6.2007-5852.

[58] C. Dupont, A. Tromba, and S. Missonnier. New strategy to preliminary design space launch vehicle based on a dedicated MDO platform. *Acta Astronautica*, 158:103–110, May 2019. ISSN 0094-5765. DOI:10.1016/j.actaastro.2018.04.013.

[59] M. Ebrahimi, M. R. Farmani, and J. Roshanian. Multidisciplinary design of a small satellite launch vehicle using particle swarm optimisation. *Structural and Multidisciplinary optimisation*, 44(6): 773–784, May 2011. ISSN 1615-1488. DOI:10.1007/s00158-011-0662-7.

[60] F. M. Villanueva. Multidisciplinary Design optimisation of a Single Stage Sounding Rocket using Swarm Intelligence. In *2022 IEEE XXIX International Conference on Electronics, Electrical Engineering and Computing (INTERCON)*, pages 1–4, 2022. doi: 10.1109/INTERCON55795.2022.9870092. DOI:10.1109/INTERCON55795.2022.9870092.

[61] M. Kanazaki, A. Ariyairt, K. Chiba, K. Kitagawa, and T. Shimada. Conceptual Design of Single-stage Rocket Using Hybrid Rocket byMeans of Genetic Algorithm. *Procedia Engineering*, 99: 198–207, 2015. ISSN 1877-7058. DOI:10.1016/j.proeng.2014.12.526.

[62] A. Okninski. Multidisciplinary optimisation of single-stage sounding rockets using solid propulsion. *Aerospace Science and Technology*, 71:412–419, 2017. ISSN 1270-9638. doi: 10.1016/j.ast.2017.09.039. DOI:10.1016/j.ast.2017.09.039.

[63] L. Federici, A. Zavoli, G. Colasurdo, L. Mancini, and A. Neri. Integrated optimisation of First-Stage SRM and Ascent Trajectory of Multistage Launch Vehicles. *Journal of Spacecraft and Rockets*, 58 (3):786–797, May 2021. ISSN 1533-6794. DOI:10.2514/1.a34930.

[64] T. Takahama and S. Sakai. Constrained optimisation by the ϵ - constrained differential evolution with an archive and gradient-based mutation. In *IEEE Congress on Evolutionary Computation*. IEEE, July 2010. DOI:10.1109/cec.2010.5586484.

[65] S.-H. Lee. Pseudo-analytic approach to determine optimal conditions for maximizing altitude of sounding rocket. *Aerospace Science and Technology*, 55:64–75, Aug. 2016. ISSN 1270-9638. doi: 10.1016/j.ast.2016.05.013. DOI:10.1016/j.phpro.2011.08.029.

[66] M. Pallone, M. Pontani, P. Teofilatto, and A. Minotti. Design methodology and performance evaluation of new generation sounding rockets. *International Journal of Aerospace Engineering*, 2018: 1–16, 2018. ISSN 1687-5974. DOI:10.1155/2018/1678709.

[67] A. Mishra, K. Gandhi, K. Sharma, N. Sumanth, and Y. Krishna. Conceptual Design and Analysis of Two Stage Sounding Rocket. *International Journal of Science and Engineering*, 07:53–73, 09 2021. DOI:10.2514/1.a34594.

[68] J. Huh and S. Kwon. A practical design approach for a single-stage sounding rocket to reach a target altitude. *The Aeronautical Journal*, 126(1301):1084–1100, 2022. DOI:10.1017/aer.2022.18.

[69] D. Mishra. *Fundamentals of Rocket Propulsion*. CRC Press, July 2017. ISBN 9781315175997. DOI:10.1201/9781315175997.

[70] H. Fernandes. Design and Analysis of the Structure of a Sounding Rocket. Master's thesis, Instituto Superior Técnico, Oct. 2024. Unpublished.

[71] P. Ekman. Development of composite fin to improved Orion rocket . Bachelor thesis, Mälardalen University, School of Innovation, Design and Engineering., 2012. Available:https://mdh.diva-portal.org/smash/record.jsf?pid=diva2%3A557411&dswid=-5735.

[72] J. J. Bertin and R. M. Cummings. *Aerodynamics for Engineers*. Cambridge University Press, Aug. 2021. ISBN 9781009098625. DOI:10.1017/9781009105842.

[73] P. A. Ritter. optimisation and design for heavy lift launch vehicles. Master's thesis, University of Tennessee, 2012.

[74] Niskanen, Sampo. OpenRocket technical documentation For OpenRocket version 13.05. Technical report, 2013.

[75] J. Anderson. *Aircraft Performance & Design*. McGraw-Hill international editions. McGraw-Hill Education, 1999. ISBN 9780070019713.

[76] S. Vukelich, S. Stoy, K. Burns, J. Castillo, and M. Moore. *Missile Datcom: Final report*. Number v. 1 in AFWAL-TR. Flight Dynamics Laboratory, Air Force Wright Aeronautical Laboratories, Air Force Systems Command, United States Air Force, 1988.

[77] P. M. Sforza. *Manned Spacecraft Design Principles*. Elsevier Inc., 2016. ISBN 9780128044254.

[78] B. Finio. Model Rocket Aerodynamics: Stability. https://www.sciencebuddies.org/science-fair-projects/project-ideas/Aero_p002/aerodynamics-hydrodynamics/model-rocket-stability?, september 2023. Accessed 31-03-2024.

[79] W. Larson, J. Wertz, and B. D'Souza. *SMAD III: Space Mission Analysis and Design, 3rd Edition : Workbook*. Space technology library. Microcosm Press, 2005. ISBN 9780792359012.

[80] J. Bunkley, L. J. M. Caballes, M. Ajuwon, and G. Chen. Design Analysis of Rocket Tail Fins Aimed at Higher Apogee by Computer Simulation. *American Society for Engineering Education*, 2022.

[81] A. Pektas, U. Haciabdullahoglu, N. Ejder, Z. Demircan, and C. Tola. Effects of Different Fin Shapes on Apogee and Stability of Model Rockets. In *2019 9th International Conference on Recent Advances in Space Technologies (RAST)*, pages 193–199, 2019. DOI:10.1109/rast.2019.8767439.

[82] M. Shahir and A. Sapit. A Study On Aerodynamic Shape of Fin of Model Rocket Using Computational Fluid Dynamics (CFD). *Faculty of Mechanical and Manufacturing Engineering, Universiti Tun Hussein Onn Malaysia*, 2021.

[83] H. Bart. Why should airfoil your fins? Peak of Flight Newsletter, 3355 Fillmore Ridge Heights, Colorado Springs, Colorado 80907-9024 USA, January 2012.

[84] B. Marciniak and J. Kindracki. Development of a Parachute Recevorey System for Sounding Rockets. In *Proceedings of the 6th European Conference for Aeronautics and Space Sciences*, 2015. Available:https://www.eucass.eu/component/docindexer/?task=download&id=3524.

[85] L. Pepermans, E. Menting, M. Rozemeijer, B. Koops, N. S. Dahl, N. Suard, S. khurana, F. V. Marion, F. Kuhnert, and M. Serman. Comparison of Various Parachute Deployment Systems for Full Rocket Recovery of Sounding Rockets. In *Proceedings of the 8th European Conference for Aeronautics and Space Sciences. Madrid, Spain, 1-4 july 2019*, 2019. DOI:10.13009/EUCASS2019-411.

[86] D. Pytlak, J. Kowalczyk, A. Kipiela, P. Rodo, J. Kappes, J. Kierski, and M. Sochacki. Design and validation of the recovery systems of students' sounding rockets. In *2023 IEEE Aerospace Conference*, pages 1–18, 2023. DOI:10.1109/AERO55745.2023.10115749.

[87] J. S. Barrowman and J. A. The Theoretical Prediction of the Center of Pressure. *National Association of Rocketry*, 1966. Available: https://www.apogeerockets.com/downloads/barrowman_report.pdf.

[88] J. S. Barrowman. Calculating the center of pressure of a model rocket. High Power Rocketry TIR-33, 1998.

[89] J. S. Barrowman. The Practical Calculation of the Aerodynamic Characteristics of Slender Finned Vehicles. Master's thesis, Faculty of the Schol of Engineering and Architecture of The Catholic University of America, Washington, D. C, March 1967. Available:https://ntrs.nasa.gov/api/citations/20010047838/downloads/20010047838.pdf.

[90] G. K. Mandell, G. J. Caporasao, and W. Bengen. *Topics in Advanced Model Rocketry*. MIT Press Classics, 1973. ISBN 9780262020961.

[91] S. Box, C. M. Bishop, and H. Hugh. Estimating the dynamic and aerodynamic parameters of passively controlled high power rockets for flight simulation. *Cambridge Rocketry*, 2009. Available: https://cambridgerocket.sourceforge.net/AerodynamicCoefficients.pdf.

[92] A. Robert. Drag Coefficient Prediction Model. 1996.

[93] N. Kubota. Principles of Solid Rocket Motor Design. *Journal of Pyrotechnics*, Issue 20, 2004. Available:https://www.jpyro.co.uk/wp-content/uploads/j20_27_hsl5-2.pdf.

[94] B. Dequick, M. Lefebvre, and P. Hendrick. Sensitivity Analysis of a Two-Phase CFD Simulation of a 1 kN Paraffin-Fueled Hybrid Rocket Motor. *Energies*, 14(20), oct 2021. ISSN 1996-1073. doi: 10.3390/en14206794. DOI:10.3390/en14206794.

[95] D. R. Greatrix. *Hybrid Rocket Engines*, page 417–434. Springer London, 2012. ISBN 9781447124856. DOI:10.1007/978-1-4471-2485-6_12.

[96] A. Bussmann. Parametric study on hybrid rocket propulsion system performance measured by the system specific impulse. Master's thesis, Luleå University of Technology, 2022. Available:https://www.diva-portal.org/smash/get/diva2:1671476/FULLTEXT01.pdf.

[97] K. Kuo and M. Summerfield. *Fundamentals of Solid-propellant Combustion*. Progress in astronautics and aeronautics. American Institute of Aeronautics and Astronautics, 1984. ISBN 9780915928842.

[98] J. M. Tizó. Burnback Analysis of Solid Propellant Rocket Motors. *arXiv preprint*, 2023. DOI:10.48550/ARXIV.2301.04559.

[99] R. Hartfield, R. Jenkins, J. Burkhalter, and W. Foster. A Review of Analytical Methods for Solid Rocket Motor Grain Analysis. In *39th AIAA/ASME/SAE/ASEE Joint Propulsion Conference and Exhibit*. American Institute of Aeronautics and Astronautics, June 2003. doi: 10.2514/6.2003-4506. DOI:10.2514/6.2003-4506.

[100] W. Miller. *Solid Rocket Motor Performance Analysis and Prediction*. NASA SP 8039. National Aeronautics and Space Administration, May 1971.

[101] U. S. N. Aeronautics, S. Administration, and W. Brooks. *Solid Propellant Grain Design and Internal Ballistics*. NASA SP 8076. National Aeronautics and Space Administration, March 1972.

[102] G. Henry, R. Humble, W. Larson, U. S. D. of Defense, U. S. N. Aeronautics, and S. Administration. *Space Propulsion Analysis and Design*. College custom series. McGraw-Hill, 1995. ISBN 9780070313293.

[103] A. Nosseir. Rocket Design and Structural Modeling & Analysis of Micro-Satellite Launch Vehicle. Master of science in aerospace engineering, Università Di Pisa, january 2020.

[104] G. F. Bernstein. *Structural Design Requirements and Factors of Safety for Spaceflight Hardware*. NASA Standard, Lyndon B. Johnson Space Center, Houston, Texas, jsc 65828, B edition, March 2014.

[105] J. R. Simmons. Aeroelastic Optimization of Sounding Rocket Fins. Master's thesis, U.S. Air Force Institute of Technology, June 2009.

[106] I. E. Theodorsen, T. & Garrick. Mechanism of Flutter: A Theoretical and Experimental Investigation of the Flutter Problem. Report No. 685, NACA, Langley Aeronautical Laboratory Langley Field, Va, 1940.

[107] D. J. Martin. Summary Of Flutter Experiences As A Guide To The Preliminary Design of Lifting Surfaces On Missiles. Report No. 685, NACA, Langley Aeronautical Laboratory Langley Field, Va, 1940.

[108] A. Tewari. *Atmospheric and Space Flight Dynamics: Modeling and Simulation with MATLAB® and Simulink® (Modeling and Simulation in Science, Engineering and Technology)*. Modeling and Simulation in Science, Engineering and Technology. Birkhäuser Boston, 1 edition, 2006. ISBN 9780817644376; 0817644377.

[109] U. S. N. Oceanic, A. Administration, and U. S. C. on Extension to the Standard Atmosphere. *U.S. Standard Atmosphere, 1976*. NOAA - SIT 76-1562. National Oceanic and Amospheric [sic] Administration, 1976.

[110] U. S. C. on Extension to the Standard Atmosphere, U. S. N. Aeronautics, and S. Administration. *U.S. Standard Atmosphere, 1962: ICAO Standard Atmosphere to 20 Kilometers; Proposed ICAO Extension to 32 Kilometers; Tables and Data to 700 Kilometers*. U.S. Government Printing Office, 1962.

[111] J. P. Jasa, J. T. Hwang, and J. R. R. A. Martins. Open-source coupled aerostructural optimisation using *python*. *Structural and Multidisciplinary optimisation*, 57(4):1815–1827, April 2018. DOI:10.1007/s00158-018-1912-8.

[112] H. Akima. A New Method of Interpolation and Smooth Curve Fitting Based on Local Procedures. *Journal of the ACM*, 17(4):589–602, Oct. 1970. ISSN 1557-735X. DOI:10.1145/321607.321609.

[113] Akima1DInterpolator — SciPy v1.14.1 Manual. `https://docs.scipy.org/doc/scipy/reference/generated/scipy.interpolate.Akima1DInterpolator.html`. [Accessed 05-10-2024].

[114] P. Sforza. *Theory of Aerospace Propulsion*. Aerospace Engineering. Elsevier Science, 2016. ISBN 9780128096017. DOI:10.1016/c2009-0-61051-5.

[115] L. Sopegno, P. Livreri, M. Stefanovic, and K. P. Valavanis. Thrust Vector Controller Comparison for a Finless Rocket. *Machines*, 11(3):394, Mar. 2023. ISSN 2075-1702. DOI:10.3390/machines 11030394.

[116] I. Gerth and E. Mooij. Guidance for Autonomous Precision Landing on Atmosphereless Bodies. In *AIAA Guidance, navigation, and control conference*, page 0088. American Institute of Aeronautics and Astronautics, Jan. 2014. DOI:10.2514/6.2014-0088.

[117] SpaceForest. Perun. Commercial suborbital rocket flights! `https://spaceforest.pl/perun/`, 2024. [Accessed 09-10-2024].

[118] J. R. R. A. Martins and A. B. Lambe. Multidisciplinary Design optimisation: A Survey of Architectures. *AIAA Journal*, 51(9):2049–2075, Sept. 2013. ISSN 1533-385X. DOI:10.2514/1.j05189 5.

[119] M. Balesdent. *Multidisciplinary Design optimisation of Launch Vehicles*. PhD thesis, Ecole Centrale de Nantes (ECN), 11 2011. English.

[120] N. Alexandrov and R. Lewis. Algorithmic perspectives on problem formulations in MDO. In *8th Symposium on Multidisciplinary Analysis and optimisation*. American Institute of Aeronautics and Astronautics, Sept. 2000. DOI:10.2514/6.2000-4719.

[121] R. Balling and J. Sobieszczanski-Sobieski. optimisation of coupled systems - A critical overview of approaches. In *5th Symposium on Multidisciplinary Analysis and optimisation*. American Institute of Aeronautics and Astronautics, Aug. 1994. doi: 10.2514/6.1994-4330. DOI:10.2514/6.1994-43 30.

[122] J. Sobieszczanski-Sobieski and R. T. Haftka. Multidisciplinary aerospace design optimisation: survey of recent developments. *Structural optimisation*, 14(1):1–23, Aug. 1997. ISSN 1615-1488. DOI:10.1007/bf01197554.

[123] J. Agte, O. de Weck, J. Sobieszczanski-Sobieski, P. Arendsen, A. Morris, and M. Spieck. MDO: assessment and direction for advancement—an opinion of one international group. *Structural and Multidisciplinary optimisation*, 40(1–6):17–33, Apr. 2009. ISSN 1615-1488. DOI:10.1007/s00158-009-0381-5.

[124] N. Tedford and J. R. R. A. Martins. On the Common Structure of MDO Problems: A Comparison of Architectures. In *11th AIAA/ISSMO Multidisciplinary Analysis and optimisation Conference*. American Institute of Aeronautics and Astronautics, June 2006. DOI:10.2514/6.2006-7080.

[125] M. Sferza, J. Ninić, D. Chronopoulos, F. Glock, and F. Daoud. Multidisciplinary Optimisation of Aircraft Structures with Critical Non-Regular Areas: Current Practice and Challenges. *Aerospace*, 8(8):223, Aug. 2021. ISSN 2226-4310. DOI:10.3390/aerospace8080223.

[126] P. Dépincé, B. Guédas, and J. Picard. Multidisciplinary and multiobjective optimisation: Comparison of several methodss. In *7th World Congress on Structural and Multidisciplinary optimisation)*, 2007.

[127] E. J. Cramer, J. E. Dennis, Jr., P. D. Frank, R. M. Lewis, and G. R. Shubin. Problem Formulation for Multidisciplinary optimisation. *SIAM Journal on optimisation*, 4(4):754–776, Nov. 1994. DOI:10.1137/0804044.

[128] J. Nocedal and S. Wright. *Numerical optimisation*. Springer Series in Operations Research and Financial Engineering. Springer New York, 2006. ISBN 9780387400655.

[129] M. Janga Reddy and D. Nagesh Kumar. Evolutionary algorithms, swarm intelligence methods, and their applications in water resources engineering: a state-of-the-art review. *H2Open Journal*, 3(1):135–188, Jan. 2020. ISSN 2616-6518. DOI:10.2166/h2oj.2020.128.

[130] B. G. Dantzig. Origins of the simplex method. Technical Report SOL 87-5 AD-A182 708, Systems optimisation Laboratory, May 1987.

[131] J. A. Nelder and R. Mead. A Simplex Method for Function minimisation. *The Computer Journal*, 7 (4):308–313, Jan. 1965. ISSN 1460-2067. DOI:10.1093/comjnl/7.4.308.

[132] N. Karmarkar. A new polynomial-time algorithm for linear programming. *Combinatorica*, 4(4): 373–395, Dec. 1984. ISSN 1439-6912. DOI:10.1007/bf02579150.

[133] S. Obayashi. Multidisciplinary design optimisation of aircraft wing planform based on evolutionary algorithms. In *SMC'98 Conference Proceedings. 1998 IEEE International Conference on Systems, Man, and Cybernetics (Cat. No.98CH36218)*, volume 4, pages 3148–3153 vol.4. IEEE, 1998. DOI:10.1109/icsmc.1998.726486.

[134] F. Castellini, M. Lavagna, A. Riccardi, and C. Bueskens. Multidisciplinary Design optimisation Models and Algorithms for Space Launch Vehicles. In *13th AIAA/ISSMO Multidisciplinary Analysis optimisation Conference*. American Institute of Aeronautics and Astronautics, June 2010. DOI:10.2514/6.2010-9086.

[135] D. Kraft. *A Software Package for Sequential Quadratic Programming*. Deutsche Forschungs- und Versuchsanstalt für Luft- und Raumfahrt Köln: Forschungsbericht. Wiss. Berichtswesen d. DFVLR, 1988.

[136] M. P. Kelly. Transcription Methods for Trajectory optimisation: a beginners tutorial, 2017. DOI:https://doi.org/10.48550/arxiv.1707.00284.

[137] D. Guého, G. He, P. Singla, and R. G. Melton. Optimal spacecraft docking maneuver using direct and indirect collocation method and particle swarm optimisation. In *AIAA/AAS Astrodynamics Specialist Conference*, page 848, 2019.

[138] D. A. Benson, G. T. Huntington, T. P. Thorvaldsen, and A. V. Rao. Direct Trajectory optimisation and Costate Estimation via an Orthogonal Collocation Method. *Journal of Guidance, Control, and Dynamics*, 29(6):1435–1440, Nov. 2006. ISSN 1533-3884. DOI:10.2514/1.20478.

[139] P. J. Enright and B. A. Conway. Discrete approximations to optimal trajectories using direct transcription and nonlinear programming. *Journal of Guidance, Control, and Dynamics*, 15(4): 994–1002, July 1992. ISSN 1533-3884. DOI:10.2514/3.20934.

[140] O. von Stryk and R. Bulirsch. Direct and indirect methods for trajectory optimisation. *Annals of Operations Research*, 37(1):357–373, Dec. 1992. ISSN 1572-9338. DOI:10.1007/bf02071065.

[141] A. Rao, D. Benson, G. Huntington, B. Origin, L. Seattle, C. Wa, C. Francolin, M. Darby, and M. Patterson. User's Manual for GPOPS Version 2.1: A MATLAB R Package for Dynamic optimisation Using the Gauss Pseudospectral Method. *Gainesville, FL, USA*, 2009. Available: `https://gpops2.com/resources/gpops2UsersGuide.pdf`.

[142] F. Topputo and C. Zhang. Survey of Direct Transcription for Low-Thrust Space Trajectory optimisation with Applications. *Abstract and Applied Analysis*, 2014:1–15, 2014. ISSN 1687-0409. DOI:10.1155/2014/851720.

[143] I. M. Ross and F. Fahroo. Pseudospectral Knotting Methods for Solving Nonsmooth Optimal Control Problems. *Journal of Guidance, Control, and Dynamics*, 27(3):397–405, May 2004. ISSN 1533-3884. DOI:10.2514/1.3426.

[144] J. S. Gray, J. T. Hwang, J. R. R. A. Martins, K. T. Moore, and B. A. Naylor. OpenMDAO: an open-source framework for multidisciplinary design, analysis, and optimisation. *Structural and Multidisciplinary optimisation*, 59(4):1075–1104, Mar. 2019. ISSN 1615-1488. DOI:10.1007/s00158-019-02211-z.

[145] R. Falck, J. Gray, K. Ponnapalli, and T. Wright. Dymos: A *Python* package for optimal control of multidisciplinary systems. *Journal of Open Source Software*, 6(59):2809, Mar. 2021. ISSN 2475-9066. DOI:10.21105/joss.02809.

[146] H. Chung, J. T. Hwang, J. S. Gray, and H. A. Kim. Topology optimisation in OpenMDAO. *Structural and Multidisciplinary optimisation*, 59(4):1385–1400, Feb. 2019. ISSN 1615-1488. doi: 10.1007/s00158-019-02209-7. DOI:10.1007/s00158-019-02209-7.

[147] L. Dalcín, R. Paz, and M. Storti. MPI for *Python*. *Journal of Parallel and Distributed Computing*, 65(9):1108–1115, Sept. 2005. ISSN 0743-7315. DOI:10.1016/j.jpdc.2005.03.010.

[148] S. Balay, W. D. Gropp, L. C. McInnes, and B. F. Smith. *Efficient Management of Parallelism in Object-Oriented Numerical Software Libraries*, page 163–202. Birkhäuser Boston, 1997. ISBN 9781461219866. DOI:10.1007/978-1-4612-1986-6_8.

[149] C. Heath and J. Gray. OpenMDAO: Framework for Flexible Multidisciplinary Design, Analysis and optimisation Methods. In *53rd AIAA/ASME/ASCE/AHS/ASC Structures, Structural Dynamics and Materials Conference 2012*, 04 2012. ISBN 978-1-60086-937-2. DOI:10.2514/6.2012-1673.

[150] J. T. Hwang, D. Y. Lee, J. W. Cutler, and J. R. R. A. Martins. Large-Scale Multidisciplinary optimisation of a Small Satellite's Design and Operation. *Journal of Spacecraft and Rockets*, 51(5): 1648–1663, Sept. 2014. ISSN 1533-6794. DOI:10.2514/1.a32751.

[151] J. P. Jasa, J. T. Hwang, and J. R. R. A. Martins. Open-source coupled aerostructural optimisation using *Python*. *Structural and Multidisciplinary optimisation*, 57(4):1815–1827, Feb. 2018. ISSN 1615-1488. DOI:10.1007/s00158-018-1912-8.

[152] H. Chung, J. T. Hwang, J. S. Gray, and H. A. Kim. Implementation of topology optimisation using openMDAO. In *2018 AIAA/ASCE/AHS/ASC Structures, Structural Dynamics, and Materials Conference*. American Institute of Aeronautics and Astronautics, Jan. 2018. DOI:10.2514/6.2018-0653.

[153] M. S. *Rexus User Manual: Rocket Experiments for University Students*. Number 7.11. EuroLaunch, JAN 2014. Available: `https://www.zarm.uni-bremen.de/fileadmin/user_upload/teaching/study_programs/rexus_bexus/RX_UserManual_v7-11_08Jan14.pdf`.

[154] NASA. Rocket Thrust Equations. `https://www.grc.nasa.gov/www/k-12/airplane/rktthsum.html`, 2021. [Accessed 04-09-2024].

[155] B. Dahlquist. Wind Caused Instability. *High Power Rocketry*, 1998.

[156] R. Galejs. Wind Instability, What Barrowman Left Out. 1999.

Appendix A

Flowcharts and Diagrams

A.1 MDO Diagram

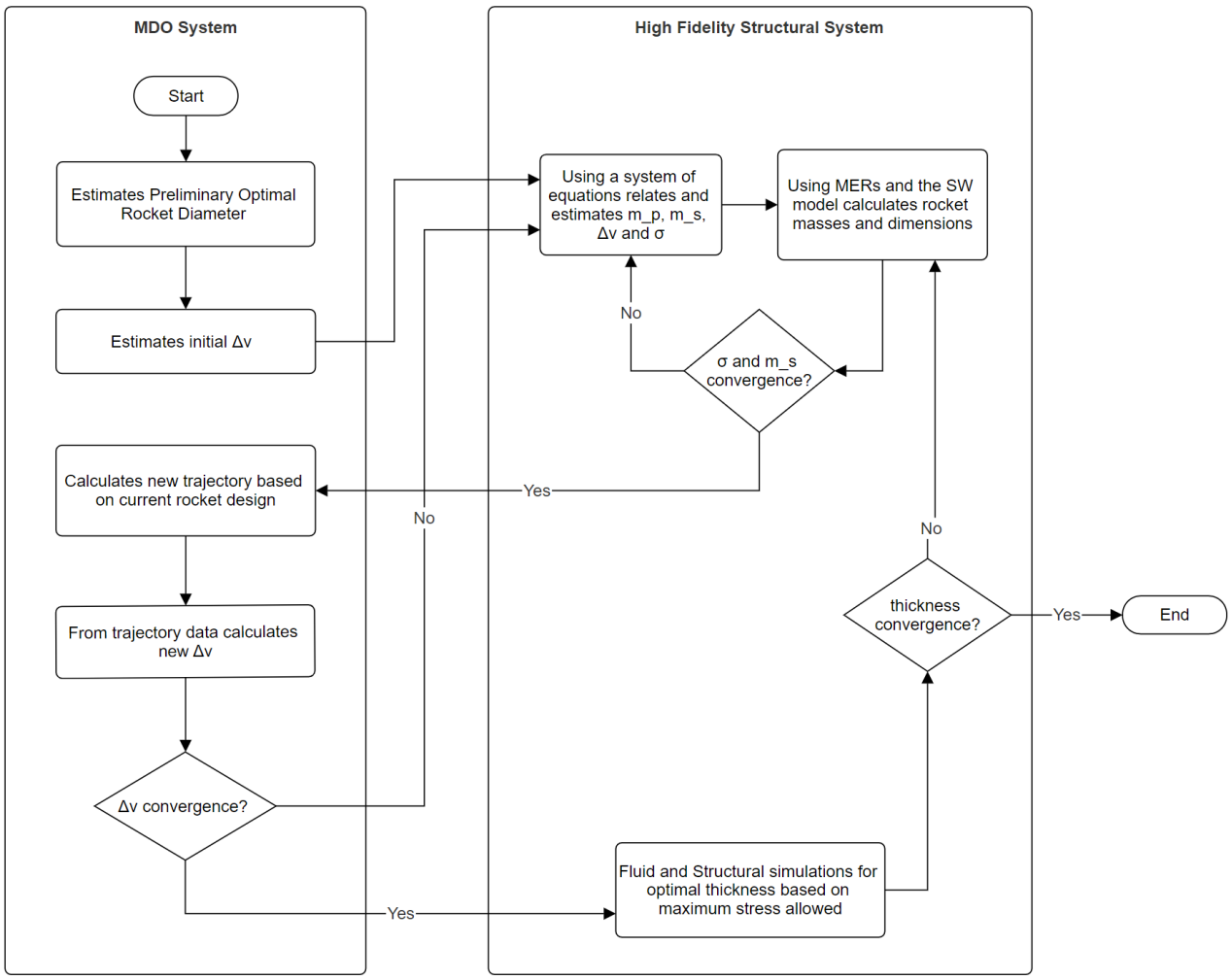

Figure A.1: Flowchart of the MDO framework integrated with a High Fidelity Structural Analysis model.

A.2 2D Rocket Schematics

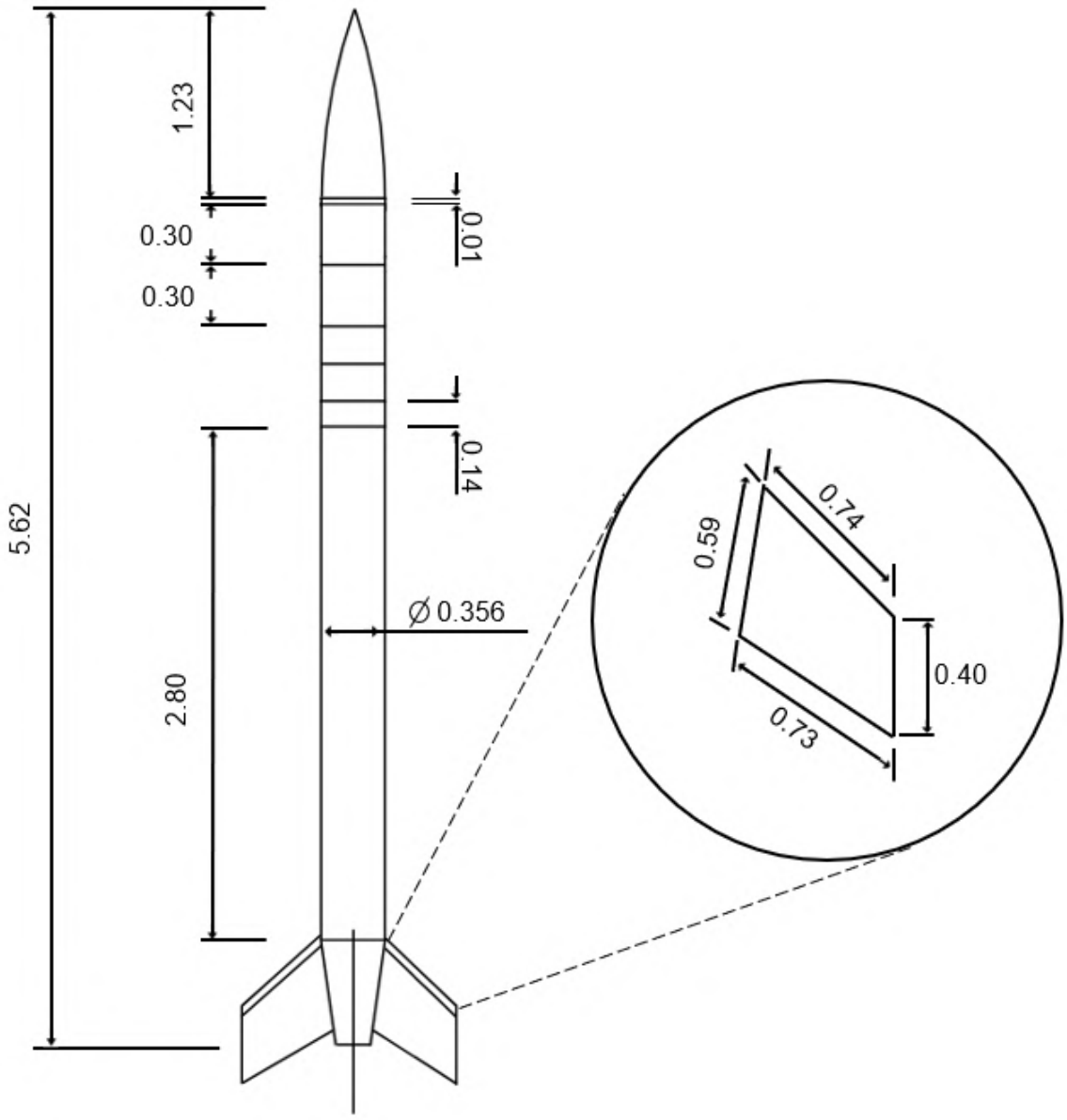

Figure A.2: 2D Schematic view of the REXUS 2. Adapted from [13].

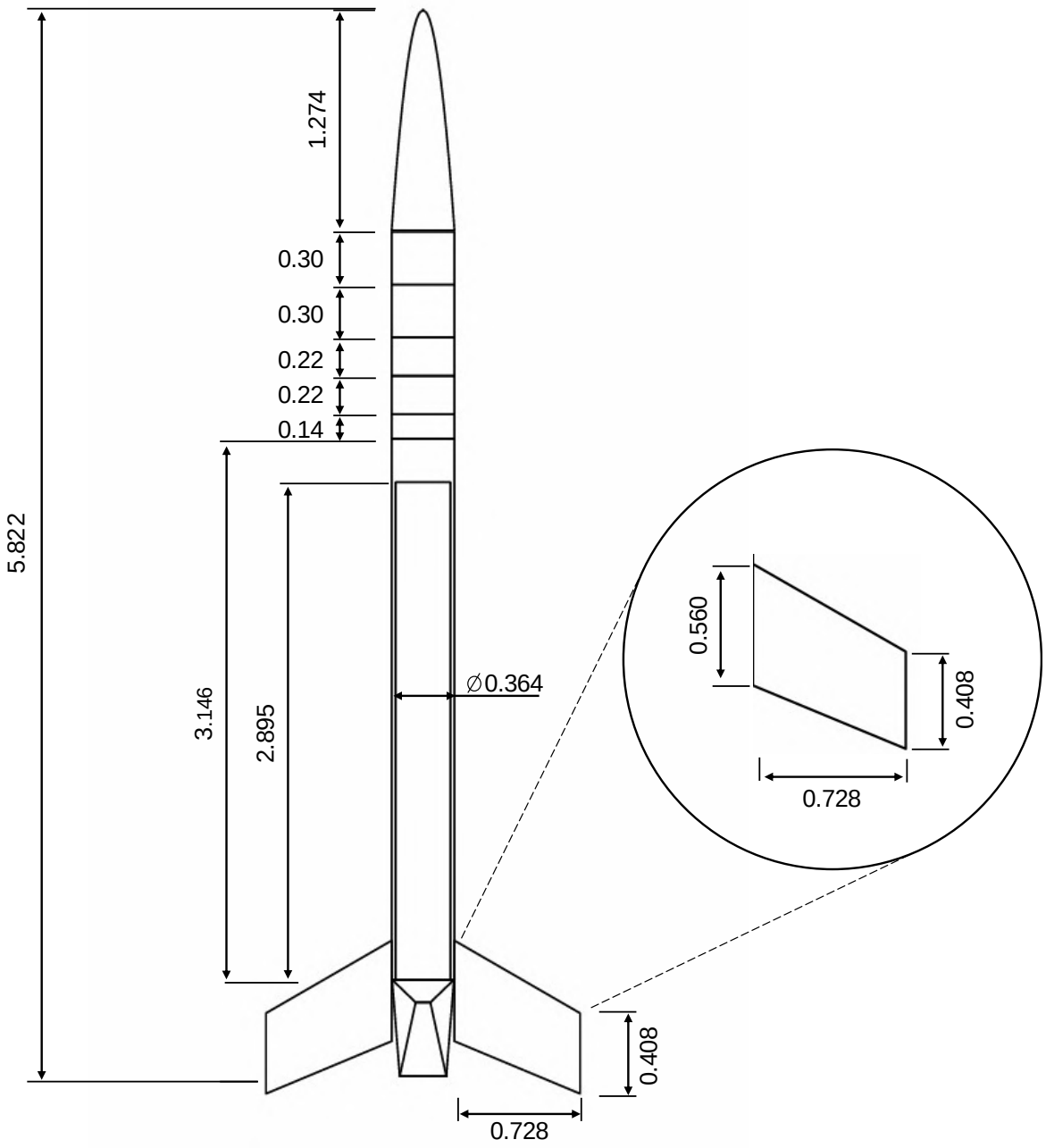

Figure A.3: 2D Schematic view of the benchmark case study optimised rocket.

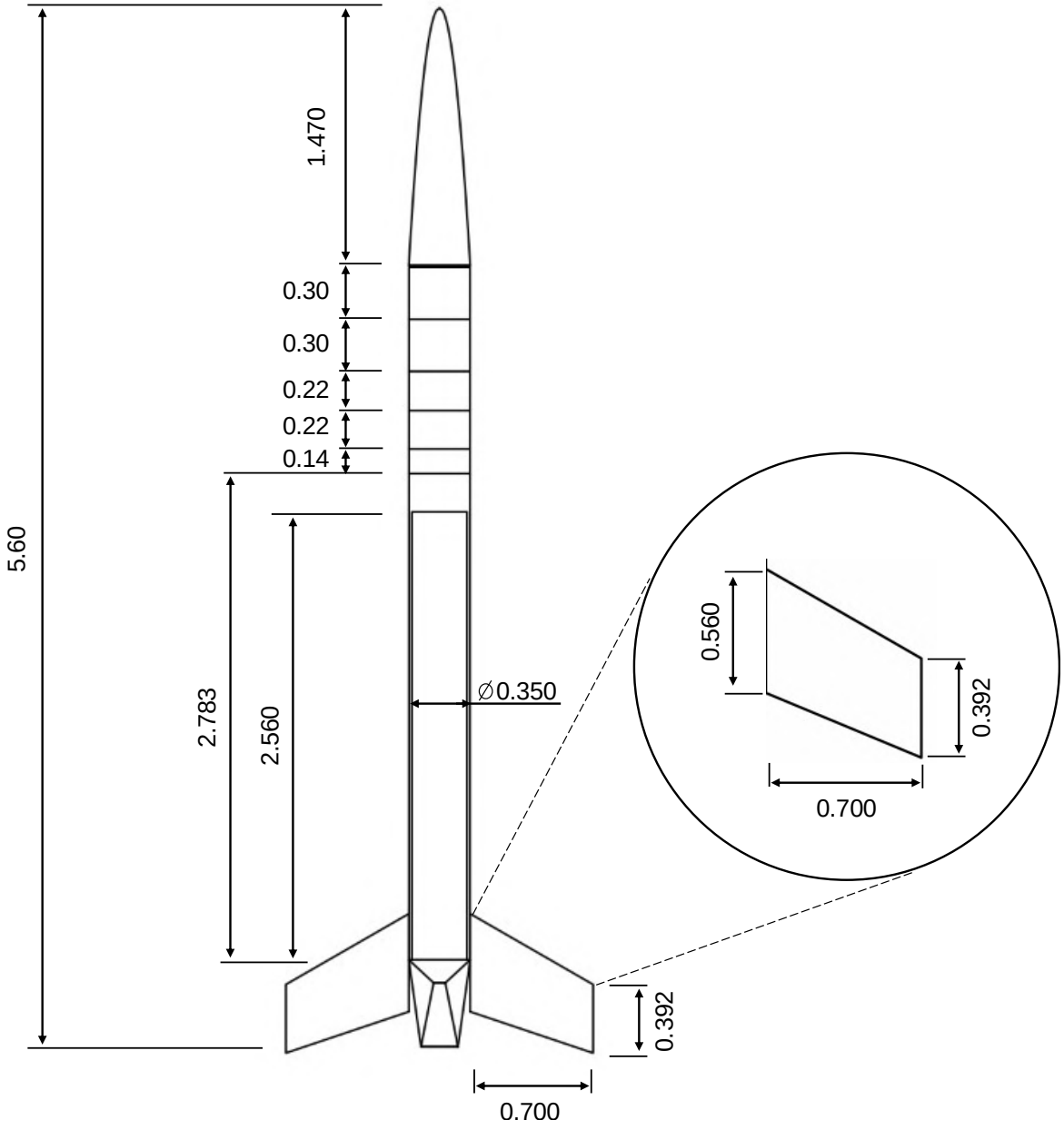

Figure A.4: 2D Schematic view of the multivariable case study optimised rocket.

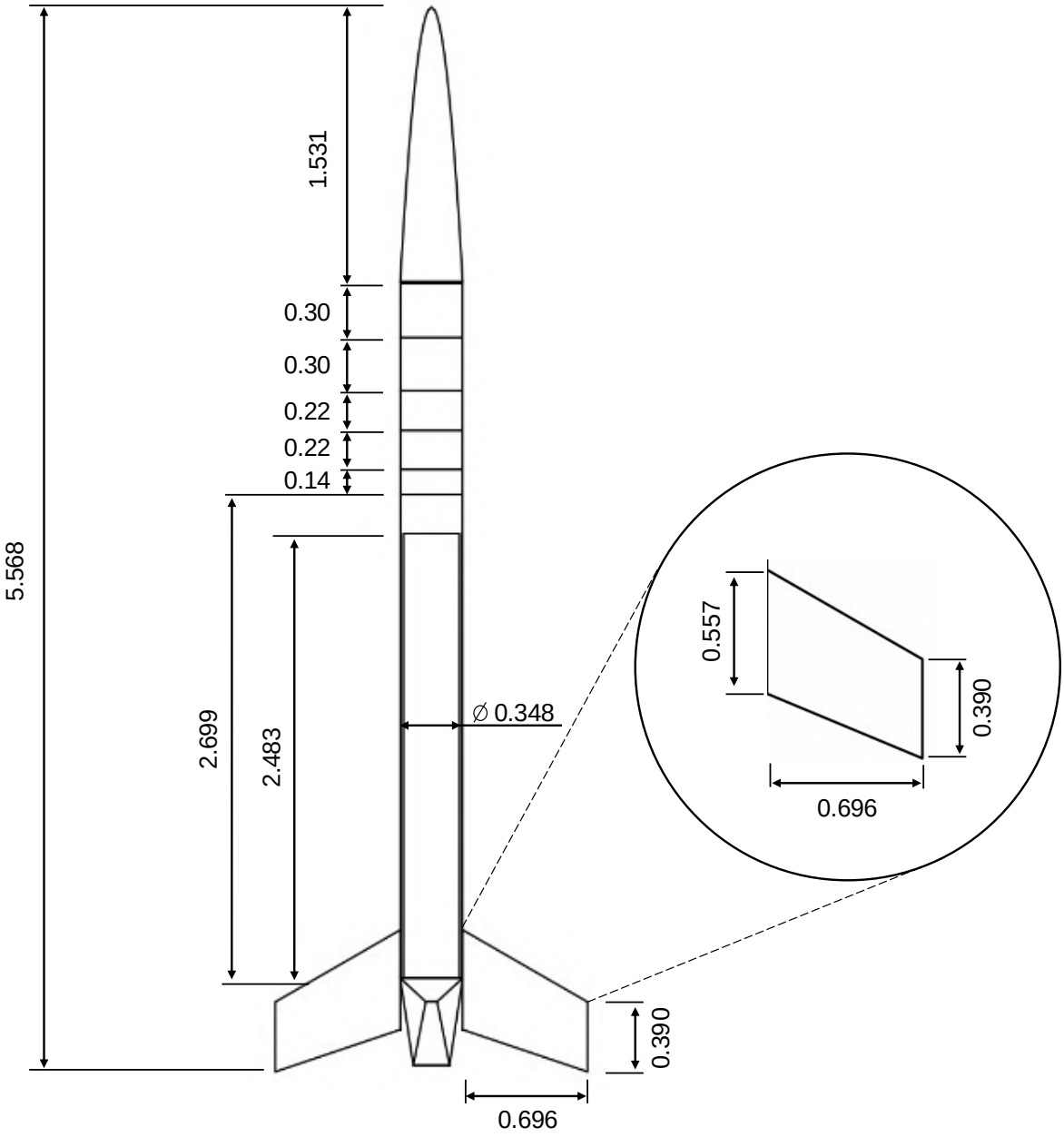

Figure A.5: 2D Schematic view of the Rexus 10 case study optimised rocket.

Appendix B

Equations

B.1 Propulsion Model Equations

Table B.1: Burnback Analysis Equations.

Parameter	Symbol	Equation		Reference
Initial Propellant Mass	m_{p0}			
Instantaneous Propellant Mass	m_{pi}	$m_{pi} = m_{p0} - (m_0 - m_i)$	(B.1)	[52]
Propellant Mass Density	ρ_p			
Initial Rocket Mass	m_0			
Instantaneous Rocket Mass	m_i	$R_p = \sqrt{\frac{-m_{pi}}{\rho_p \pi L_{grain} + R_i^2}}$	(B.2)	[52]
Port Radius	R_p			
Propellant Burning Area	A_b			
Grain Length	L_{grain}	$A_b = 2\pi R_p L_{grain}$	(B.3)	[52]
Grain Inner Radius	R_i			

Table B.2: Internal Ballistic Equations.

Parameter	Symbol	Equation		Reference
Internal Chamber Pressure	P_c			
Burn Rate Coefficient	a	$T_e = T_c \left[1 + \frac{\gamma - 1}{2} M_e^2\right]^{-1}$	(B.4)	[97]
Propellant mass density	ρ_p			
Propellant Burning Area	A_b			
Nozzle Discharge Coefficient	C_D	$P_c = \left[\frac{a \rho_p A_b}{C_D A_t}\right]^{\frac{1}{1-n}}$	(B.5)	[97, 154]
Nozzle Throat Area	A_t			
Propellant Ballistic Exponent	n			
Nozzle Exit Pressure	P_e			
Nozzle Exit Velocity	V_e	$P_e = P_c \left[1 + \frac{\gamma - 1}{2} M_e^2\right]^{\frac{-\gamma}{\gamma - 1}}$	(B.6)	[97, 154]
Gas Universal Constant	R			
Nozzle Gases Exit Temperature	T_e			
Internal Chamber Temperature	T_c	$V_e = M_e \sqrt{\gamma R T_e}$	(B.7)	[97, 154]
Gas Specific Heat Ratio	γ			
Nozzle Exit Mach Number	M_e			
Thrust	T	$\dot{m} = -C_D A_t P_t$	(B.8)	[97]
Thrust Coefficient	C_F			
Mass Rate Change	$\dot{m}$			
Gravitational Acceleration	g	$Thrust = \dot{m} V_e + (P_e - P) A_e$	(B.9)	[97]
Specific Impulse	Isp			

B.2 Mass and Sizing Model Equations

Table B.3: Nose Cone Component Equations.

Parameter	Symbol	Equation		Reference
Rocket Radius	R_{rocket}			
Rocket Length	L_{rocket}	$R_{rocket} = \frac{D_{rocket}}{2}$	(B.10)	[52]
Rocket Length to Diameter Ratio	L/D_{rocket}			
Nose Cone Length to Diameter Ratio	$L/D_{nose\,cone}$	$L_{rocket} = L/D_{rocket} D_{rocket}$	(B.11)	[52]
Rocket Reference Area	S_r			
Nose Cone Diameter	D_{nc}	$S_r = \pi R_{rocket}^2$	(B.12)	[52]
Nose Cone Length	L_{nc}			
Nose Cone Surface Area	S_{nc}	$D_{nc} = D_{rocket}$	(B.13)	[52]
Nose Cone Tip Mass	m_{nc}			
Nose Cone Mass	m_{nc}	$L_{nc} = D_{nc} L/D_{nose\,cone}$	(B.14)	[52]
Nose Cone Mass Density	ρ_{nc}			
Nose Cone Tip Mass Density	ρ_{tip}	$m_{tip} = \rho_{tip} V_{tip}$	(B.15)	[52]
Nose Cone Tip Mass	m_{tip}			
Nose Cone Tip Volume	V_{tip}	$m_{nc} = \rho_{nc} t_{nc} S_{nc}$	(B.16)	[52]
Nose Cone Thickness	t_{nc}			

Table B.4: Modules Component Equations.

Parameter	Symbol	Equation		Reference
Module Thickness	t_m			
Rocket Radius	R_{rocket}	$V_{mPL} = \pi(R_{PL}^2 - (R_{rocket}^2 - t_m)^2)(L_{PL} - (2t_m)) + 2\pi t_m R_{rocket}^2$	(B.17)	-
Module Mass Density	ρ_m			
Payload Module Mass	m_{mPL}	$m_{mPL} = \rho_m V_{mPL}$	(B.18)	-
Module Length	L_m			
Module Volume	V_m	$V_m = \pi(R_{rocket}^2 - (R_{rocket} - t_m)^2) L_m + 2\pi t_m R_{rocket}^2$	(B.19)	-
Experiment Mass	m_E			
Recovery System Mass	m_R	$m_m = V_m \rho_m$	(B.20)	-
Module Volume	V_m			
Payload Module Volume	V_{mPL}	$m_{Et} = m_m + m_E$	(B.21)	-
Payload Length	L_{PL}			
Payload Radius	R_{PL}	$m_{St} = m_m + m_S$	(B.22)	-
Experiment Module Total Mass	m_{Et}			
Service Module Total Mass	m_{St}	$m_{Rt} = m_m + m_R$	(B.23)	-
Recovery Module Total Mass	m_{Rt}			
Payload Module Total Mass	m_{mPL}	$m_{PLt} = m_{mPL} + m_{PL}$	(B.24)	-
Payload Module Total Mass	m_{PLt}			

Table B.5: Fins Component Equations.

Parameter	Symbol	Equation		Reference
Fin Root Chord	c_r			
Fin Root Chord Constant	K_{cr}	$c_r = K_{cr} D_{rocket}$	(B.25)	-
Rocket Diameter	D_{rocket}			
Fin Tip Chord	c_{tip}	$c_{tip} = K_{c\,tip} D_{rocket}$	(B.26)	-
Fin Tip Chord Constant	$K_{c\,tip}$			
Fin Semi Span	F_{ss}	$F_{ss} = K_{Fss} D_{rocket}$	(B.27)	-
Fin Semi Span Constant	K_{Fss}			
Fin Surface Area	A_{fins}	$A_{fins} = \frac{c_r c_{tip}}{2F_{ss}}$	(B.28)	-
Fins Mass	m_{fins}			
Fin Mean Thickness	t_{fins}			
Fin Mass Density	ρ_{fins}	$m_{fins} = n_{fins}(A_{fins} t_{fins}) \rho_{fins}$	(B.29)	-
Number of fins	n_{fins}			

Table B.6: Nozzle Component Equations.

Parameter	Symbol	Equation		Reference
Nozzle Throat Area	A_t	$A_t = \frac{c_{del} T_{vac}}{P_c g_0 I_{sp_{Vac}}}$	(B.30)	[52]
Nozzle Exhaust Velocity	c_{del}			
Average Thrust in Vacuum	T_{vac}	$A_e = \varepsilon A_t$	(B.31)	[52]
Average Internal Casing Pressure	P_c			
Gravitational Acceleration at Sea Level	g_0	$R_t = \sqrt{\frac{A_t}{\pi}}$	(B.32)	[52]
Specific Impulse in Vacuum	I_{sp_Vac}			
Nozzle Expansion Ratio	ε			
Nozzle Exit Area	A_e	$R_e = \sqrt{\frac{A_e}{\pi}}$	(B.33)	[52]
Nozzle Throat Radius	R_t			
Nozzle Exit Radius	R_e	$D_n = 2R_e$	(B.34)	[52]
Nozzle Convergent Section Angle	$\alpha_{convergent}$			
Nozzle Diameter	D_n	$L_n = 0.8\left(\frac{2R_e - 2R_t}{2\tan(\alpha)}\right)$	(B.35)	[52]
Nozzle Angle	α			
Nozzle Length	L_n			
Nozzle Adapter Length	L_{na}	$L_{na} = \frac{(D_{Rocket} - 2t_{bt}) - 2R_t}{2\tan(\alpha_{convergent})}$	(B.36)	[52]
Nozzle Adapter Mass Density	ρ_{na}			
Nozzle Mass Density	ρ_n			
Nozzle Adapter Volume	V_{na}	$m_{na} = \rho_{na} V_{na}$	(B.37)	[52]
Nozzle Volume	V_n			
Nozzle Adapter Mass	m_{na}	$m_n = \rho_n m_n$	(B.38)	[52]
Nozzle Mass	m_n			

Table B.7: Body Tube Component Equations.

Parameter	Symbol	Equation		Reference
Body Tube Length	L_{bt}			
Rocket Length	L_{rocket}	$L_{bt} = L_{rocket} - L_{nc} - 3L_m - L_n - L_{na}$	(B.39)	
Nose Cone Length	L_{nc}			
Module Length	L_m			
Nozzle Adapter Length	L_{na}	$V_{bt} = \pi(R_{rocket}^2 - (R_{rocket} - t_{bt})^2)L_{bt}$	(B.40)	[52]
Nozzle Length	L_n			
Body Tube Thickness	t_{bt}			
Body Tube Volume	V_{bt}	$m_{bt} = \rho_{bt} V_{bt}$	(B.41)	
Body Tube Mass	m_{bt}			

Table B.8: SRM Component Equations.

Parameter	Symbol	Equation		Reference
SRM Casing Length	L_c			
Rocket Radius	R_{rocket}	$L_c = L_{bt}$	(B.42)	-
Body Tube Length	L_{bt}			
SRM Casing Radius	R_c	$R_c = R_{rocket} - t_{bt}$	(B.43)	-
Body Tube Thickness	t_{bt}			
Casing Thickness	t_c	$m_c = \left(\pi(R_c^2 - (R_c - t_c)^2)(L_c - 2t_c) + 2\pi t_c R_c^2\right)\rho_c$	(B.44)	-
Casing Mass Density	ρ_c			
Casing Mass	m_c	$R_{go} = R_{rocket} - t_c$	(B.45)	-
Nozzle Length	L_n			
Body Tube Thickness	t_{bt}	$R_{gi} = R_{go} - t_g$	(B.46)	-
Body Tube Volume	V_{bt}			
Body Tube Mass	m_{bt}	$L_g = L_c$	(B.47)	-
Grain Outer Radius	R_{go}			
Grain Inner Radius	R_{gi}	$m_p = \pi L_g(R_{go}^2 - R_{gi}^2)\rho_p$	(B.48)	-
Grain Length	L_g			
Grain Web Thickness	t_g	$m_{ins} = \left(0.02(\pi L_c(R_c^2 - (R_c - t_c)^2)\right)\rho_{ins}$	(B.49)	[52]
Propellant Mass Density	ρ_p			
Propellant Mass	m_p	$m_{SRM} = m_c + m_{ins} + m_p$	(B.50)	[52]
Insulation Density	m_{ins}			

Table B.9: Rocket Component Equations.

Parameter	Symbol	Equation		Reference
Rocket Initial Mass	m_0			
SRM Casing Length	L_c			
Rocket Length	L_{rocket}			
Nose Cone Mass	m_{nc}	$m_0 = m_{nc} + m_{tip} + m_{PLt} + m_{Et} + m_{St} + m_{Rt}$		[51]
Nose Cone Tip Mass	m_{tip}	$+ m_{fins} + m_{bt} + m_n + m_{na} + m_w + m_p$	(B.51)	
Experiment Module Total Mass	m_{Et}	$+ m_c$		
Service Module Total Mass	m_{St}			
Recovery Module Total Mass	m_{Rt}			
Payload Module Total Mass	m_{PLt}	$m_s = m_{tip} + m_{nc} + m_{mPL} + m_{mE} + m_w$		
Fins Mass	m_{fins}	$+ m_{St} + m_{Rt} + m_{bt} + m_c + m_{fins}$	(B.52)	[51]
Body Tube Mass	m_{bt}	$+ m_n + m_{na}$		
Nozzle Mass	m_n			
Nozzle Adapter Mass	m_{na}			
Wiring Mass	m_w			
Propellant Mass	m_p			
SRM casing	m_c	$\sigma = \frac{m_s}{m_s + m_p}$	(B.53)	[51]
Propellant Mass Density	ρ_p			
Propellant Mass	m_p			
Structural Mass	m_s	$m_f = m_0 - m_p$	(B.54)	[51]
Structural Factor	σ			
Rocket Final Mass	m_f			

B.3 Aerodynamics Model Equations

Table B.10: Aerodynamics Equations.

Parameter	Symbol	Equation		Reference
Zero lift Drag Coefficient	Cd_0	$Cd_0 = Cd_{nc} + Cd_b + Cd_f$	(B.55)	[90]
Nose Cone Drag	Cd_b			
Fin Drag Coefficient	Cd_f			
Drag Coefficient Correction	C'_d			
Free Stream Mach Number	M_a	$C'_d = \begin{cases} \frac{C_{d0}}{\sqrt{1-M_a^2}}, & M_a < 0.8 \\ \frac{C_{d0}}{\sqrt{1-0.8^2}}, & 0.8 < M_a < 1.1 \\ \frac{C_{d0}}{\sqrt{M_a^2-1}}, & M_a > 1.1 \end{cases}$	(B.56)	[91]
Free Stream Density	ρ			
Free Stream Velocity	v			
Rocket Reference Area	S_{rocket}			
Rocket Drag	D_{rocket}	$D_{rocket} = \frac{1}{2}\rho v^2 C'_d S_{rocket} v^2$	(B.57)	[51]
Drogue Induced Drag Coefficient	$C_{Ddrogue}$			
Drogue Parachute Cross-Section Area	S_{drogue}			
Main Parachute Induced Drag Coefficient	$C_{Dmain\ parachute}$	$D_{drogue} = \frac{1}{2}\rho v^2 C_{Ddrogue} S_{drogue}$	(B.58)	[85]
Drogue Parachute Drag	D_{drogue}			
Main Parachute Cross-Section Area	$S_{main\ parachute}$			
Main Parachute Drag	$D_{main\ parachute}$	$D_{main\ parachute} = \frac{1}{2}\rho v^2 C_{main\ parachute} S_{main\ parachute}$	(B.59)	[85]

B.4 Structural Model Equations

Table B.11: Buckling Equations.

Parameter	Symbol	Equation		Reference
Buckling Critical Stress	σ_{crit}	$\sigma_{crit} = \frac{\gamma E}{\sqrt{3(1-v^2)}}\left(\frac{th}{R}\right)$	(B.60)	[103]
Multiplication Factor	γ			
Cylindrical Shell Young Modulus	E			
Poisson Ratio	v	$\gamma = 1 - 0.901\left(1 - e^{-\phi}\right)$	(B.61)	[103]
Body Tube Thickness	th			
Body Tube Radius	R			
Exponent Factor	ϕ	$L_{crit} = \sigma_{crit}\pi(R^2 - (R-th)^2)$	(B.62)	[103]
Buckling Critical Load	L_{crit}			

Table B.12: Fin Flutter Equations.

Parameter	Symbol	Equation		Reference
Fin Flutter Velocity	V_f	$V_f = a\sqrt{\frac{G_E}{\frac{YAR^3}{(t/c_r)^3(AR+2)}\left(\frac{\lambda+1}{2}\right)\left(\frac{P}{P_0}\right)}}$	(B.63)	[107]
Speed of Sound	a			
Effective Shear Modulus of the Fins	G_E			
Fins Aspect Ratio	AR			
Fins Thickness	t			
Fins Root Cord	c_r			
Fins Tapper Ratio	λ			
Atmospheric Air Pressure	P			
Atmospheric Air Pressure at Sea Level	P_0	$Y = \frac{24\epsilon\gamma P_0}{\pi}$	(B.64)	[107]
Flutter Constant	Y			
Fin 1/4 Cord to CM Distance	ϵ			
Atmospheric Air Specific Heat Ratio	γ			

B.5 Flight Dynamics Model Equations

Table B.13: Flight Dynamics Equations.

Parameter	Symbol	Equation		Reference
Velocity	v	$\dot{v} = \frac{Thrust}{m}\cos\alpha - \frac{D}{m} - g\sin\gamma$	(B.65)	[108]
Rocket Thrust	$Thrust$			
Rocket Mass	m			
Angle of Attack	α	$\dot{\gamma} = -\left(\frac{g}{v} - \frac{v}{R_e+h}\right)\cos\gamma + \frac{Thrust}{m}\sin\alpha$	(B.66)	[108]
Rocket Drag	D			
Gravitational Acceleration	g			
Pitch Angle	γ	$\dot{x} = v\cos\gamma$	(B.67)	[108]
Pitch Angle Rate	$\dot{\gamma}$			
Earth Radius	R_e			
Rocket Altitude	h	$\dot{h} = v\sin\gamma$	(B.68)	[108]
Downrange rate	$\dot{x}$			

B.6 Barrowman and Mandel Aerodynamic Coefficient Derivation

First, it is important to acknowledge that there are two main conventions available in the literature to define what are essentially the two orthogonal components of the same force, the aerodynamic force.

On the one hand, the convention used by Barrowman [87, 88], according to which the aerodynamic force components are defined relative to the rocket's roll axis, which will be used here to calculate the normal force coefficient, C_N, and, on the other hand, the convention used by Mandell et. al [90], which defines the aerodynamic force components in relation to the rocket's apparent velocity vector, V, which will be used here to calculate the drag force coefficient, C_D.

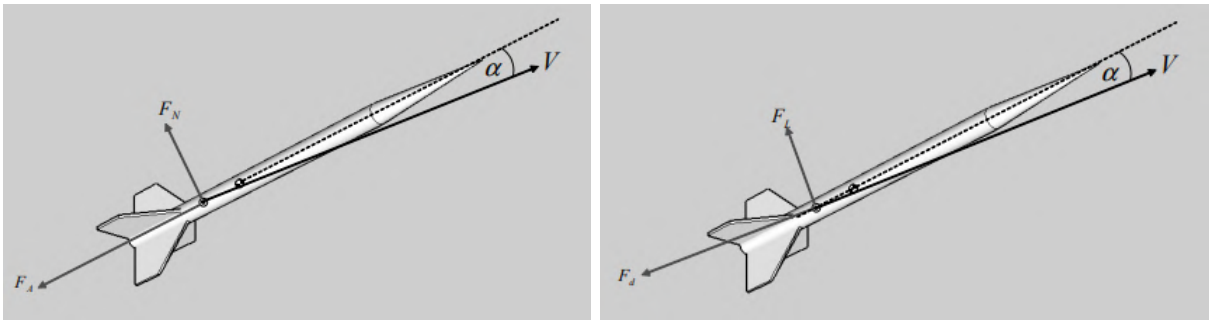

Figure B.1: Aerodynamic force conventions: used by Barrowman, on the right, and by Mandell, on the left [91].

Normal Force and Centre of Pressure

A brief set of equations for estimating the aerodynamic normal force and the centre pressure location will now be presented following the full derivation of Barrowman's method [88].

Initially, Barrowman lists a strict set of assumptions:

- Angle of attack of the rocket lower than 10 ° ($\alpha < 10°$);
- Compressibility effects can be negleted (for velocities under 0.4 Ma);
- Lift forces on the rocket body tube can be neglected;
- The air flow is smooth and does not change abruptly;
- The rocket body is slender;
- The nose cone of the rocket progresses smoothly from its base to a point edge;
- The rocket is an axisymmetric rigid body and the fins are approximated to thin flat plates;

Similarly to the given definition for the drag force, in equation 2.41, Barrowman defines the normal force on the rocket as:

$$F_N = \frac{1}{2}\rho V^2 A_r C_N \tag{B.69}$$

where A_r is the cross sectional area of the base of the rocket's nose cone.

Because it is assumed there only to be incompressible flow and that viscous forces are neglected, C_N is a function of only α. Additionally, only small angles of α are assumed, and so, C_N can be expressed as a linear function of α:

$$C_N = C_{N\alpha}\alpha \tag{B.70}$$

where $C_N\alpha$ is the total stability derivative of the normal force coefficient.

$C_N\alpha$ is calculated as the sum of each individual rocket's component stability derivative:

$$C_{N\alpha(R)} = \sum_{P \in R} C_{N\alpha(P)} \tag{B.71}$$

where P refers to a specific rocket component and R refers to the rocket itself.

Regarding the location of the centre of pressure, it is assumed that it lies on the rocket's roll axis with a position defined according to its distance from the nose cone tip, X_{cp}. It is calculated as follows:

$$X_{cp(R)} = \frac{\sum_{P \in R} C_{N\alpha(P)} X_{cp(P)}}{C_{N\alpha(R)}} \tag{B.72}$$

where $X_{cp(P)}$ is the centre of pressure distance of component P to the tip of the nose cone of the rocket.

Barrowman's assumption that the lift forces on the rocket body are negligible has been questioned by experiments conducted in particularly long slender bodies by Dahlquist [155]. A possible solution to this problem suggested by Box et. al [91] is to extend Barrowman's equations, adding terms that take into account the normal force due to body lift, as proposed by Galejs [156].

The normal force coefficient due to body lift is, then, defined as follows [156]:

$$C_{N(L)} = K\frac{A_p}{A_r}\alpha^2 \tag{B.73}$$

where K is a constant with values ranging from 1.0 to 1.5, A_p is the planform area of the rocket (excluding the fins) and A_r is the reference area for the rocket which is the cross-sectional area at the base of the nose cone. Consequently, $C_{N(L)}$ is not a linear function of α.

Galejs also defines,

$$C_{N\alpha^2} = \frac{C_{N(L)}}{\alpha} = K\frac{A_p}{A_r}\alpha \tag{B.74}$$

which can be added to equation B.71.

The centre of pressure due to the body lift force, $X_{cp(L)}$ can be determined by calculating the centre of the planform area.

To determine the new centre of pressure of the rocket, $X_{cp(R)}$, the terms $C_{N\alpha^2}$ and $X_{cp(L)}$ should be added to equation B.72.

Drag Force

After having defined the set of equations to determine the rocket's normal force and the centre of

pressure, a new set of equations will be presented for estimating the coefficient of drag force of the rocket as proposed by Mandel et. all [90] following Box's method [91].

Initially, the drag force coefficient will be divided into its main components which will be calculated for a zero angle of attack:

- **Body Drag** - the component fundamentally related to the rocket forebody [90]:

$$C_{D(fb)} = \left[1 + \frac{60}{(\frac{l_{(TR)}}{d_b})^3} + 0.0025\frac{l_b}{d_b}\right]\left[2.7\frac{l_n}{d_b} + 4\frac{l_b}{d_b} + 2\left(1 - \frac{d_d}{d_b}\right)\frac{l_c}{d_b}\right]C_{f(fb)} \tag{B.75}$$

  where l_{TR} is the total length of the rocket body, l_c is the length of the boat tail, d_b is the maximum rocket body diameter, $C_{f(fb)}$ is the rocket forebody's coefficient of viscous friction (here definided by equation XX) [91];

- **Base Drag** - the component related to a low pressure region at the base of the rocket due to the boundary layer separation [90]:

$$C_{D(b)} = 0.029\frac{\left(\frac{d_d}{d_b}\right)^3}{\sqrt{C_{D(fb)}}} \tag{B.76}$$

- **Fin Drag** - the component related to the presence of a finset attached to the rocket body [90]:

$$C_{D(f)} = 2C_{f(f)}\left(1 + 2\frac{T_f}{l_m}\right)\frac{4nA_{fp}}{\pi d_f^2} \tag{B.77}$$

  where $C_{f(f)}$ is the fins' coefficient of viscous friction (here defined by equation XX), T_f is the fin thickness, n is the number of fins and d_f is the diameter of the body tube at the fin root, A_fp is the fin planform area (for a trapezoidal fin the exposed part is given by $A_{fe} = \frac{1}{2}(l_r + l_t)\, l_s$ and the full planform area is assumed to extend to the centre line of the rocket body $A_{fp} = A_{fe} + \frac{1}{2}d_f l_r$) [91];

- **Interference Drag** - the component which translates the interference effects between the fins and the rocket body [90]:

$$C_{D(i)} = 2C_{f(f)}\left(1 + 2\frac{T_f}{l_m}\right)\frac{4n(A_{fp} - A_{fe})}{\pi d_f^2} \tag{B.78}$$

- **Viscous Friction Drag** - the component which relates to the skin friction between the rocket body and the air flow due to the latter's viscosity properties, the reason why it is highly dependent on the Reynolds number, Re [90]:

$$C_f = \begin{cases} \frac{1.328}{\sqrt{R_e}} & when \quad Re \leq Re_c \\ \frac{0.074}{Re^{\frac{1}{5}}} - \frac{B}{Re} & when \quad Re \geq Re_c \end{cases} \tag{B.79}$$

  where B is a parameter defined as:

$$B = Re_c\left(\frac{0.074}{Re^{\frac{1}{5}}} - \frac{1.328}{\sqrt{Re}}\right) \tag{B.80}$$

The total drag coefficient for a zero angle of attack, $C_{D(0)}$, can be easily calculated by summing up its individual drag coefficients, as follows [90]:

$$C_{D(0)} = C_{D(fb)} + C_{D(b)} + C_{D(f)} + C_{D(i)} \tag{B.81}$$

For small angles of attack, Mandell et. al. [90] suggests that two more components, derived from wind tunnel experiments, should be added to the zero angle of attack drag coefficient, previously defined in equation B.81.

- **Coefficient of alpha drag on the rocket body** - component related to the additional drag enforced on the rocket body under small angles of attack [90]:

$$C_{Db(\alpha)} = 2\delta\alpha^2 + \frac{3.6\eta(1.36l_{TR} - 0.55l_n)}{\pi d_b}\alpha^3 \tag{B.82}$$

  where α is the angle of attack and both δ and η are experimental coefficients derived from wind tunnel testing.

- **Coefficient of alpha drag on the rocket's fins** - component associated with the additional drag enforced on the rocket fin's under small angles of attack [90]:

$$C_{Df(\alpha)} = \alpha^2 \left[1.2\frac{A_{fp}4}{\pi d_f^2} + 3.12(k_{fb} + k_{bf} - 1)\left(\frac{A_{fe}4}{\pi d_f^2}\right)\right] \tag{B.83}$$

  where k_{fb} and k_bf are the fin-body interference coefficient and body-fin interference coefficient, respectively.

$$k_{fb} = 0.8065R_s^2 + 1.1553R_s \tag{B.84}$$

$$k_{bf} = 0.1935R_s^2 + 0.8174R_s + 1 \tag{B.85}$$

  where R_s is the fin section ratio which is the ratio between the total fin's span, l_TS, and the diameter of the body tube at the point of the fins, d_f.

The total coefficient of drag of the rocket can now be calculated by summing up these coefficients:

$$C_D = C_{D(0)} + C_{Db\alpha} + C_{Df\alpha} \tag{B.86}$$

Finally, the axial force coefficient can be estimated:

$$C_A = \frac{C_D cos\alpha - \frac{1}{2}C_N sin(2\alpha)}{1 - sin^2\alpha} \tag{B.87}$$